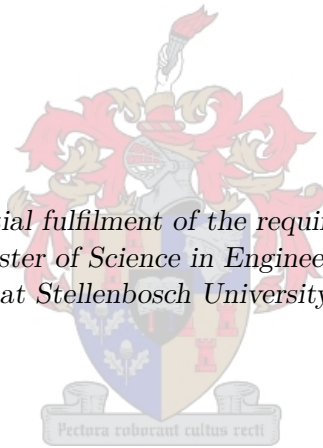


An Analysis and Comparison of Two Methods for UAV
Actuator Fault Detection and Isolation

by

Hendrik Mostert Odendaal

*Thesis presented in partial fulfilment of the requirements for the degree of
Master of Science in Engineering
at Stellenbosch University*



Supervisor:

Prof T. Jones
Department Electrical and Electronic Engineering

October 2012

Declaration

By submitting this thesis electronically, I declare that the entirety of the work contained therein is my own, original work, that I am the sole author thereof (save to the extent explicitly otherwise stated), that reproduction and publication thereof by Stellenbosch University will not infringe any third party rights and that I have not previously in its entirety or in part submitted it for obtaining any qualification.

October 2012

Abstract

Fault detection and isolation (FDI) is an important aspect of effective fault tolerant control architectures. The Electronic System Laboratory at Stellenbosch University identified the need to study viable methods of FDI. In this research two FDI methods for actuator failures on the Meraka Modular UAV are investigated.

The Meraka Modular UAV is an unmanned aircraft that was developed by the CSIR. A simple six degree of freedom non-linear mathematical model is developed that presents a platform on which the two FDI methods are formulated. The theoretical model is used in a simulation environment to extensively test and compare the performance of the proposed FDI methods in different types of flight conditions.

The first method investigated is a multiple model adaptive estimator (MMAE), which incorporates a bank of Kalman filters. Each Kalman filter in the MMAE is conditioned for each expected actuator fault scenario. The limitations of using linear Kalman filters are explained and they are replaced by extended Kalman filters, whose associated advantages and disadvantages are discussed. Each filter in the bank of Kalman filters produces a residual vector and residual covariance matrix. This information is subjected to a Bayes classifier to determine the fault scenario which will have the highest likelihood of being active.

The second method that is studied incorporates the parity space approach for FDI. The parity space consists of the parity relations that quantify all the analytical redundancies available between the sensors' outputs and actuator inputs of a system. A transformation matrix is then optimised to transform these parity relations into residuals that are specially sensitive to specific actuator faults. Actuator faults cause the parity space residuals' variance to increase. A cumulative summation procedure is used to determine when the residuals' variance has changed sufficiently to indicate an actuator fault. A pseudoinverse actuator estimation scheme is used to extract the actuator deflections from the parity relations.

The FDI performance is tested by deliberately failing specific actuators of the Meraka Modular UAV in-flight. The flight test data is then used to analyse and compare the performance of the two FDI methods investigated in the research. It is found that, for the specific Meraka Modular UAV, the FDI performs as expected with disturbance effects and actuator excitation influencing the FDI effectiveness. The research shows that the bank of Kalman filters creates less false alarms whereas the parity space FDI is more sensitive to faults. It is illustrated that FDI can be improved with active actuator excitation and process noise estimation techniques, delivering promising results.

Uittreksel

Fout-deteksie en -isolasië (FDI) is belangrik vir 'n stelsel se beheerder om foute te kan hanteer. Die Elektroniese Stelsellaboratorium (ESL) by die Universiteit van Stellenbosch het die behoefte geïdentifiseer om te gaan kyk na moontlike FDI-stelsels wat gebruik kan word op hul onbemande vliegtuie (OV). In hierdie navorsing is daar na twee FDI-metodes gekyk wat op die Meraka Modulêre OV toegepas kan word.

Die Meraka Modulêre OV is 'n vliegtuig wat deur die WNNR ontwikkel is. 'n Eenvoudige ses-grade-van-vryheid, nie-liniêre wiskundige model van die Meraka Modulêre OV is ontwikkel, en die FDI-metodes is rondom hierdie model geformuleer. Die teoretiese model is gebruik in 'n simulasië-omgewing en die werkverrigting van die twee FDI-metodes is in verskillende vlug-omstandighede getoets en vergelyk.

Die eerste metode waarna gekyk is, was 'n multi-model aanpasbare afskatter (MMAA), wat 'n bank van Kalman-filters gebruik. Elke Kalman-filter in die MMAA is gekondisioneer vir elke denkbare aktueerder-fout. Die beperkinge rondom liniêre Kalman-filters is uitgelig en vergelyk met uitgebreide Kalman-filters, waarvan die voor- en nadele bespreek is. Elke filter in die MMAA produseer 'n residu-vektor en residu-kovariansiematriks. Hierdie informasie is na 'n Bayes-klassifiseerder gestuur om te bepaal watter fout-senario die grootste waarskynlikheid het om aktief te wees.

Die tweede metode waarna gekyk is, het die pariteitsruimte vir FDI gebruik. Die pariteitsruimte is uit al die pariteitsverwantskappe opgebou wat die verhoudings tussen al die insette en uitsette van 'n sisteem kwantifiseer. 'n Transformasie-matriks is geoptimaliseer om hierdie pariteitsverwantskappe te transformeer na residue wat elkeen sensitief is tot 'n spesifieke aktueerderfout. 'n Spesifieke aktueerderfout veroorsaak dat 'n spesifieke residu se variansie verhoog. 'n Kummatiewe sommeringsproses is dan gebruik om te bepaal of die variansie genoegsaam toegeneem het. Sodoende kon daar bepaal word of 'n fout ontstaan het. 'n Pseudo-inversaktueerder-afskattingsmetode is gebruik om die afgeskatte aktueerderdefleksie uit die pariteitsverwantskappe te onttrek.

Die FDI-werkverrigtinge van die twee metodes is getoets deur sekere aktueerders met opset te laat faal gedurende vlugtoetse. Die vlugtoetsdata is gebruik om die werkverrigting van die FDI-metodes te analiseer en met mekaar te vergelyk. Met die spesifieke Meraka Modulêre OV is, soos te wagte, bevind dat verstuurings en aktueerderopwekking 'n groot invloed op die FDI's se werkverrigtinge toon.

Die bevindinge het getoon dat die MMAA-metode minder vals alarms veroorsaak, terwyl die pariteitsruimte meer sensitief vir foute is. Die navorsing toon ook dat die werkverrigting van beide FDI-metodes verbeter kan word met behulp van bykomende aktueerderopwekking en prosesdruisafskattingsmetodes, wat goeie resultate lewer.

Contents

Abstract	iii
Uittreksel	iv
List of Figures	xi
List of Tables	xiii
Nomenclature	xiv
Acknowledgements	xxi
1 Introduction	1
1.1 Background	1
1.2 Preliminary Literature Study	3
1.2.1 Definitions of Fault Tolerant Control and Fault Detection and Isolation	3
1.2.2 Different Theories, Models and Hypotheses	6
1.2.3 Existing Data and Empirical Findings	8
1.2.4 Measuring Techniques and Instruments for Hypotheses Testing	8
1.3 Research Problem and Objectives	9
1.4 Thesis Outline	10
2 Aircraft Model	12
2.1 Reference Frames Definitions	12
2.1.1 Inertial Reference Frame	12
2.1.2 Body Reference Frame	13
2.1.3 Wind Reference Frame	14
2.2 Notation	14
2.3 Frame Transformations	16
2.3.1 Euler Angles	16
2.3.2 Rotation Matrices	17
2.3.3 Position and Attitude Dynamics	17
2.3.4 Velocity Transformations	18
2.3.5 Quaternions	18
2.4 Assumptions	18

2.5	Equations of Rigid-Body Motion	19
2.5.1	Equations of Forces	19
2.5.2	Equations of Moments	20
2.5.3	General Equations	21
2.6	Aerodynamic Forces and Moments	21
2.7	Gravitational Forces and Moments	23
2.8	Engine Forces and Moments	23
2.9	Change in Aircraft Coefficients	23
2.10	Final Set of Non-Linear Differential Equations	27
2.11	Linearising the Mathematical Model	28
2.12	Discretising the State Space Representation	31
3	First Fault Detection and Isolation Method: A Bank of Kalman Filters	32
3.1	The Fault Detection and Isolation Architecture	32
3.2	Designing the Kalman Filters	33
3.2.1	The Kalman Filter Equations	34
3.2.2	The Kalman Filter for the No-Fault Scenario	35
3.2.3	The Kalman Filters for the Fault Scenarios	36
3.2.4	Replacing the Linear Kalman Filters with Extended Kalman Filters	37
3.3	Decision Process	38
3.3.1	Gaussian Bayes Classifier	38
3.3.2	State Estimate	41
3.3.3	Final Decision Process	42
3.4	Simulations for the Bank of Kalman Filters FDI Method	42
3.4.1	Simulation Results for a Straight and Level Flight with Minimal Process Noise	45
3.4.2	Simulation Results for a Straight and Level Flight with Substantial Process Noise	46
3.4.3	Simulation Results for a Circular Flight Path that Closely Resembles the Flight Test Trajectory	47
3.4.4	Simulation Results for a Randomly Generated Flight Mission that Induces Actuator Excitation	48
3.4.5	Simulation Results for a Straight and Level Flight with Minimal Process Noise, but the Actuators Fail with a Non-Zero Locked-in-Place Fault	49
3.5	Fault Detection and Isolation Performance	51
3.5.1	The Effect of Parameter Changes on FDI Performance	52
3.5.2	The Effect of Process Noise on FDI Performance	53
3.5.3	The Effect of Actuator Excitation on FDI Performance	54
4	Second Fault Detection and Isolation Method: The Parity Space Approach	56
4.1	Parity Relations (Analytical Redundancy)	56
4.2	The Generalised Parity Space	57

4.3	Optimising the Residuals for Fault Detection and Isolation	61
4.3.1	The Order of the Parity Space	62
4.3.2	The Process Noise Input Matrix	62
4.3.3	The Measurement Noise Input Matrix	63
4.3.4	The Faults Input Matrix	63
4.3.5	Multi-Objective Optimisation	63
4.3.6	Optimisation Technique	65
4.3.7	Optimisation Results	65
4.4	Decision Process	67
4.4.1	The Cumulative Sum Procedure	68
4.4.2	Final Decision Process	69
4.5	Actuator Deflection Estimation	73
4.6	Simulations for the Parity Space FDI Method	74
4.6.1	Simulation Results for a Straight and Level Flight with Minimal Process Noise	76
4.6.2	Simulation Results for a Straight and Level Flight with Substantial Process Noise.	77
4.6.3	Simulation Results for a Circular Flight Path that Closely Resembles the Flight Test Trajectory.	78
4.6.4	Simulation Results for a Random Generated Flight Mission.	79
4.6.5	Simulation Results for a Randomly Generated Flight Mission, but the Actuators Fail with a Locked-in-Place Fault of 2.5°	80
4.7	Fault Detection and Isolation Performance	82
4.7.1	The Effect of Parameter Changes on FDI Performance	82
4.7.2	The Effect of Process Noise on FDI Performance	82
4.7.3	The Effect of Actuator Excitation on FDI Performance	84
5	Flight Tests	86
5.1	Physical Aircraft	86
5.2	Details of the Flight Tests	88
5.2.1	Wind Conditions	88
5.2.2	Flight Trajectory	89
5.3	Results for the First Flight Test	90
5.3.1	FDI Results Using the Bank of Kalman Filters	90
5.3.2	FDI Results Using Parity Space	93
5.4	Results for the Second Flight Test	95
5.4.1	FDI Results Using the Bank of Kalman Filters	95
5.4.2	FDI Results Using Parity Space	98
6	Comparison of the Two Fault Detection and Isolation Methods	100
6.1	Simulation Results	100
6.1.1	FDI Performance Comparison in Terms of Parameter Change	100
6.1.2	FDI Performance Comparison in Terms of Process Noise	101
6.1.3	FDI Performance Comparison in Terms of Actuator Excitation	102

<i>CONTENTS</i>	ix
6.2 Flight Tests Results	103
6.3 Comparison to Other Literature	105
6.4 Noteworthy Differences	105
7 Recommendations and Conclusion	107
7.1 Recommendations	107
7.1.1 Different Failure Modes	107
7.1.2 Process Noise Estimation	107
7.1.3 Non-Linear Parity Space FDI	108
7.1.4 Practical implementation of the FDI methods	108
7.2 Active Fault Detection and Isolation	108
7.3 Conclusion	111
A Aircraft Parameters: The Meraka Modular UAV	113
B Linearisation	115
B.1 State Matrices	115
B.2 Partial Derivatives of the Elements in the State Matrices	115
B.3 Linearised State Matrices	123
C Process and Measurement Covariance Matrices	124
C.1 Process Noise	125
C.2 Measurement Noise	127
D Healthy and Faulty Residuals Covariance Matrices	128
D.1 Healthy Residuals Covariance Matrices	128
D.2 Faulty Residuals Covariance Matrices Without the Effect of Disturbances	128
D.3 Final Faulty Residuals Covariance Matrices	130
E Flight Test Plan	132
E.1 Introduction	133
E.1.1 Background	133
E.1.2 Test Objectives	133
E.1.3 Description of the Test Item	133
E.1.4 Test Scope	133
E.2 Test Preparation	134
E.2.1 Project Team	134
E.2.2 Logistical Support	134
E.2.3 Briefings and Debriefings	134
E.2.4 Safety	134
E.3 Details of the Test	135
E.3.1 Test Conditions	135
E.3.2 Data Required	135
E.3.3 Data Analysis	135
E.3.4 Acceptance Criteria	135

<i>CONTENTS</i>	x
E.4 Test Schedule	136
E.5 Equipment Checklist	137
Bibliography	138

List of Figures

1.1	Different fault modes.	4
1.2	FTC architecture with a FDI and control re-allocation module.	5
1.3	Thought process for FDI and control allocation.	6
2.1	Inertial reference frame.	13
2.2	Body reference frame with velocity notations.	13
2.3	Wind reference frame.	14
2.4	Body reference frame with force and moment notations.	15
2.5	Euler angle transformation sequence (3,2,1) in 3D [1].	16
2.6	Euler angles and the frame transformation.	17
2.7	The effect of α on the aerodynamic coefficient C_d	24
2.8	The effect of α on the aerodynamic coefficient C_l	25
2.9	The effect of β on the aerodynamic coefficient C_Y	25
2.10	The effect of β on the aerodynamic coefficient C_L	26
2.11	The effect of α on the aerodynamic coefficient C_M	26
2.12	The effect of β on the aerodynamic coefficient C_N	27
3.1	Architecture for the bank of Kalman filters.	33
3.2	Conditional probability density for a one-dimensional feature case with three possible fault scenarios.	41
3.3	The Simulink model used to simulate the performance of a bank of Kalman filters for FDI.	43
3.4	Probabilities for a straight and level flight with minimal process noise.	45
3.5	Probabilities for a straight and level flight with substantial process noise.	46
3.6	Probabilities for a circular flight path that closely resembles the flight test trajectory.	47
3.7	Probabilities for a randomly generated flight mission.	48
3.8	Probabilities for a randomly generated flight mission where the actuators fail with a locked-in-place fault of 2.5°	49
3.9	Estimated actuator deflections for a random generated flight mission where the actuators fail with a non-zero locked-in-place fault.	50
3.10	The effect of parameter changes on the bank of extended Kalman filters FDI performance.	52

3.11	The effect of process noise on the bank of extended Kalman filters' FDI performance.	53
3.12	The effect of actuator excitation on the bank of extended Kalman filters' FDI performance.	54
4.1	Conceptual use of the CUSUM procedures to help with the decision process. . .	73
4.2	The Simulink model used to simulate the performance of a parity space FDI method.	74
4.3	Fault decisions for a straight and level flight with minimal process noise.	76
4.4	Fault decisions for a straight and level flight with substantial process noise. . . .	77
4.5	Fault decisions for a circular flight path that closely resembles the flight test trajectory.	78
4.6	Fault decisions for a randomly generated flight mission.	79
4.7	Fault decisions for a randomly generated flight mission where the actuators fail with a locked-in-place fault of 2.5°	80
4.8	Actuator deflection estimation for a randomly generated flight mission where the actuators fail with a locked-in-place fault of 2.5°	81
4.9	The effect of parameter changes on the parity space FDI performance.	83
4.10	The effect of process noise on the parity space FDI performance.	83
4.11	The effect of actuator excitation on the parity space FDI performance.	84
5.1	The Meraka Modular UAV.	86
5.2	Physical right elevator at -2.5° deflection.	87
5.3	Physical right rudder at $+2.5^\circ$ deflection.	87
5.4	Physical right aileron at $+2.5^\circ$ deflection.	88
5.5	Maximum and minimum wind gusts.	89
5.6	Flight trajectory for both flight tests as seen from above.	90
5.7	Fault decisions using the bank of Kalman filters FDI.	91
5.8	Actuator deflection estimates using the bank of Kalman filters FDI.	92
5.9	Fault decisions using parity space FDI.	93
5.10	Actuator deflection estimates using parity space FDI.	94
5.11	Fault decisions using the bank of Kalman filters FDI.	96
5.12	Actuator deflection estimates using the bank of Kalman filters FDI.	97
5.13	Fault decisions using parity space FDI.	98
5.14	Actuator deflection estimates using parity space FDI.	99
6.1	FDI performance of the two FDI methods in terms of changing parameter values.	100
6.2	FDI performance of the two FDI methods in terms of process noise.	101
6.3	FDI performance of the two FDI methods in terms of actuator excitation.	102
7.1	The bank of Kalman filters FDI decisions where extra actuator excitation was added.	109
7.2	Parity space FDI decisions where extra actuator excitation was added.	110

List of Tables

3.1	Sequence of fault scenarios in the simulation.	44
4.1	Summary of chosen weighting values.	65
5.1	First test flight event summary.	90
5.2	Second test flight event summary.	95
6.1	FDI performance of first flight test.	103
6.2	FDI performance of second flight test.	104
6.3	FDI performance on the simulations in [2].	105
A.1	Meraka Modular UAV physical parameters.	113
A.2	Meraka Modular UAV stability derivatives.	114
A.3	Meraka Modular UAV control derivatives.	114
E.1	Flight test details.	132
E.2	Safety and execution sign-in form.	132
E.3	The test schedule.	136
E.4	Equipment checklist.	137

Nomenclature

Abbreviations and Acronyms

AVL	Athena Vortex Lattice
CUSUM	Cumulative Sum
CSIR	Council for Scientific and Industrial Research
CG	Centre of Gravity
CPU	Central Processing Unit
DOF	Degree Of Freedom
DCM	Direction Cosine Matrix
EKF	Extended Kalman Filter
EMMAE	Extended Multiple Model Adaptive Estimator
ESL	Electronic Systems Laboratory
FDI	Fault Detection and Isolation
FTC	Fault Tolerant Control
GBC	Gaussian Bayes Classifier
GLR	Generalised Likelihood Ratio
GPS	Global Positioning System
KF	Kalman Filter
MIT	Massachusetts Institute of Technology
MMAE	Multiple Model Adaptive Estimator
PDF	Probability Density Function
QFT	Quantitative Feedback Theory
RAM	Random Access Memory
RMS	Root Mean Square

RLS	Recursive Least Squares
UAV	Unmanned Aerial Vehicle
3D	Three-Dimensional

Uppercase Letters

<i>A</i>	Wing aspect ratio
A	Continuous state matrix
B	Continuous input matrix
<i>C</i>	Dimensionless aerodynamic coefficients
<i>C</i>	Expected shift in variance
C	Continuous measurement matrix
<i>D</i>	Aircraft displacements along the z_I -axis (downwards)
<i>E</i>	Aircraft displacements along the y_I -axis (east)
F	Force vector
F	Discretised state matrix
G	Discretised input matrix
H	Momentum vector
H	Discretised measurement matrix
<i>I</i>	Mass moment of inertia
I	Mass moment of inertia tensor
J	Parity space input matrix
<i>K</i>	CUSUM “leak” parameter
K	Kalman gains
<i>L</i>	Aircraft moment along the x_b -axis
<i>L</i>	Dimension of state vector
<i>L</i>	CUSUM detection limit
L	Parity space input matrix for process noise, measurement noise or faults
\mathcal{L}	Likelihood
<i>M</i>	Aircraft moment along the y_b -axis
<i>M</i>	Dimension of input vector

M	Moment vector
N	Aircraft moment along the z_b -axis
N	Dimension of measurement vector
N	Aircraft displacements along the x_I -axis (north)
N	Sequence of last measurement noise or process noise
\mathcal{N}	Normal distribution
O	Observability matrix
P	Aircraft angular rate along the x_b -axis
P	State estimate covariance matrix
P	Sequence of last faults
P	Parity relations vector
Q	Aircraft angular rate along the y_b -axis
Q	Process noise covariance matrix
R	Aircraft angular rate along the z_b -axis
R	Measurement noise covariance matrix
R	Parity space residuals
S	Wing (airfoil) area
S	Residual covariance matrix
S	Parity space input matrices for the process noise, measurement noise or faults
T	Thrust
T	Length of time step
T	Transformation matrix
U	Aircraft velocity along the x_b -axis (forward)
U	Sequence of the last $n + 1$ input vectors
V	Aircraft velocity along the y_b -axis (lateral)
V	Air flow velocity vector of the aircraft
W	Aircraft velocity along the z_b -axis (downward force)
X	Aircraft forces along the x_b -axis (axial force)
Y	Aircraft forces along the y_b -axis (lateral force)

Y	Sequence of last observed sensor values
Z	Aircraft forces along the z_b -axis (normal force)

Lowercase Letters

<i>b</i>	Wing span
<i>c</i>	Chord length
<i>c</i>	Arbitrary lag time
<i>c</i>	Optimisation weightings
\bar{c}	Mean aerodynamic chord
c	Directional column vector
<i>e</i>	Oswald efficiency factor
<i>f</i>	Fault signal
<i>f</i>	Probability density
<i>g</i>	Gravitational constant
<i>h</i>	Altitude above sea
<i>k</i>	Time step
<i>m</i>	Mass
<i>n</i>	Parity space order
<i>p</i>	Perturbation of angular rate along the x_b -axis
<i>p</i>	Probability
p	Momentum vector
<i>q</i>	Perturbation of angular rate along the y_b -axis
\bar{q}	Dynamic pressure
<i>r</i>	Perturbation of angular rate along the z_b -axis
<i>r</i>	Residual
<i>t</i>	Time
<i>u</i>	Perturbation of velocity along the x_b -axis
u	Input vector
<i>v</i>	Perturbation of velocity along the y_b -axis
v	Measurement noise vector

w	Perturbation of velocity along the z_b -axis
\mathbf{w}	Process noise vector
\mathbf{y}	Measurement vector
\mathbf{x}	State vector

Subscripts

A	Aileron deflection
a	Aerodynamic force or moment
b	Body reference axes
d_0	Static drag coefficient
E	Elevator deflection
F	Flap deflection
F	Faulty covariance matrix
f	Faults
g	Gravitational force or moment
H	Healthy covariance matrix
I	Inertial reference axes
k	Time step
L	Rolling moment coefficient
l	Left actuator
l	Lift coefficient
l_0	Static lift coefficient
l_α	Lift due to angle of attack
l_Q	Lift due to pitch rate
l_{δ_i}	Lift due to the i^{th} actuator
L_β	Roll moment produced by side slip coefficient
L_P	Roll moment produced due to roll rate perturbations
L_R	Roll moment produced due to yaw rate perturbations
L_{δ_i}	Roll moment produced due to the i^{th} actuator
M	Pitch moment coefficient

M_0	Static pitching moment coefficient
M_α	Pitch stiffness coefficient
M_Q	Pitch damping coefficient
M_{δ_i}	Pitching moment produced due to the i^{th} actuator
N	Yaw moment coefficient
N_β	Yaw moment produced by side slip coefficient
N_P	Yaw moment produced due to roll rate perturbations
N_R	Yaw moment produced due to yaw rate perturbations
N_{δ_i}	Yaw moment produced due to the i^{th} actuator
R	Rudder deflection
r	Right actuator
T	Trim
t	Thrust force or moment
v	Measurement noise
w	Wind reference axes
w	Process noise
$wind$	Expected wind velocity
wp	Working point
X	Axial force coefficient
Y	Lateral force coefficient
Y_β	Side force due to side slip coefficient
Y_P	Side force produced due to roll rate perturbations
Y_R	Side force produced due to yaw rate perturbations
Y_{δ_i}	Side force due to the i^{th} actuator
Z	Normal force coefficient

Greek Letters

α	Angle of attack
β	Side slip angle
δ	Control surface deflection angle

δ	Control actuator vector
Ω	Angular velocity vector
Ω	Left null space of the observability matrix
μ	Multivariate mean vector
Φ	Roll rotation angle
ϕ	Perturbation around roll angle
Ψ	Yaw rotation angle
ψ	Perturbation around yaw angle
ρ	Air density
σ	Variance
τ	Arbitrary lag time
Θ	Pitch rotation angle
θ	Perturbation around pitch angle
θ	Fault scenario
Σ	Covariance matrix

Syntax and Style

A	The matrix A (usually uppercase)
x	The vector x (usually lowercase)
\hat{x}	Indicates the estimated value of x
$E\{x\}$	Expected value of x

Acknowledgements

This research would not have been possible without the support and understanding of many people in my life. I would however like to offer my greatest thanks to the following people:

First and foremost to my supervisor, professor Thomas Jones, for his experienced guidance and indispensable knowledge. His enthusiastic encouragement has made me able to enjoy completing this research.

I would like to thank Lionel Basson and Anton Runhaar for their valuable assistance in regards to the flight tests and their patience with the Meraka Modular UAV.

Without Ami Philp I would not have had the power and perseverance to complete this research. She supported me in times of doubt and was there in times that I most needed it.

Lastly, I would like to thank my friends at the faculty, especially Dirk, Attie, Wikus and Wiaan, for the late night work sessions, immense amounts of coffee and keeping me sane.

Chapter 1

Introduction

1.1 Background

With increased technological advancement over the past century, our reliance on the systems that govern our daily lives has become greater than ever before. Humanity has reached a state in which it cannot operate without the complex systems that supply our energy, transportation, food security and even entertainment. The complexity of these systems necessitates improved reliability of the control systems that manage most of these systems. It is clear that a structure of fault detection is paramount in the pursuit of safety, reliability and performance. One of the emerging industries today is automated systems that totally or partially rely on themselves to achieve these three objectives. In this thesis actuator fault detection and isolation of an automated unmanned aerial vehicle (UAV) will be the subject of research.

UAVs have increasingly been used since the 1990s for important automated tasks in several different industries. These tasks include [2]:

- Inspections of power lines, bridges and dams
- Forest monitoring, fire detection, fire fighting (operation and management)
- Sea rescue searches
- Border patrols and law enforcement
- Environmental and climate research
- Monitoring traffic and transportation systems
- Charting and mapping
- Prospecting
- Crop yield prediction, drought monitoring and spraying of pesticides
- Observation of oil and gas pipelines in remote areas
- Tactical reconnaissance and operational support

Because of the large economic benefit UAVs have, it becomes apparent that the safety and reliability of these UAVs are vital. Several different schemes are being used to meet these goals. Redundancy and robustness are frequently used but compromises performance. Fault tolerant control (FTC) systems, a fairly new branch of control automation, overcome the need to compromise on performance by adapting the system to the fault that has occurred. These schemes are used not only in the unmanned aerospace industry, but in most modern technological systems that rely on sophisticated control systems. Most of these systems are safety-critical systems such as spacecraft, nuclear power stations, chemical plants, automobiles and manned aircraft. The aim of fault tolerance is to prevent faults from developing into serious failure, hence increasing the availability of the system and reducing the risk of safety hazards. It is necessary to design control systems that are capable of tolerating potential faults in these systems in order to improve the reliability and availability while providing desirable performance.

In a typical aircraft the pilot or control system can manipulate a set of input mechanisms. These mechanisms, such as the thrust generating engines and control surfaces, are controlled to create moments and forces that ultimately change the states of the aircraft in some desired way. The control surfaces are also commonly referred to as actuators.

A traditional airplane has three independent control actuators: the aileron pair, elevator pair and rudder. These actuators must generate desired moments and forces for which a unique solution for control can be found [3]. However, to increase the reliability, manoeuvrability and survivability of modern airplanes, control actuators are no longer limited to just these three. Many more control actuators have been introduced, as well as the decoupling of the actuator pairs, so that the left and right actuator surfaces can deflect independently. With an increase in the number of redundant actuators, the problem of allocating these controls to achieve the desired moments and forces becomes non-unique. Such redundancy has called for effective control allocation or re-allocation (in case of actuator failures) to optimally distribute the required control moment over available actuators.

A control re-allocation system was developed at Stellenbosch University as a master's study [3] and it forms an integral part of the fault tolerant control architecture being developed at their Electronics Systems Laboratory (ESL). Control allocation and re-allocation is an important process in a typical fault tolerant control scheme. A faulty actuator degrades the achievable moments and forces that can be created by the set of actuators. The control allocation system minimises the difference between the desired and achievable aircraft performance parameters by optimising the allocation of control effort commanded by the control system to the physical actuators on the aircraft. For the control allocation scheme to work it must know that a fault has occurred and it must know the type of fault, the size of the fault, and which actuators are defective [3].

For an effective control allocation process a reliable fault detection and isolation (FDI) system must be in place to supply the required information. Aircraft can use several costly sensors directly attached to the control surfaces to conduct the FDI process by means of a voting scheme. In recent years it has become common practice to use analytical redundancy to supplement some of the sensors in achieving FDI and so reduce the required costs for

reliable FDI. The topic of this research therefore focuses on actuator fault detection and isolation through the use of analytical redundancy.

1.2 Preliminary Literature Study

The FDI for UAVs is a rich field of research and a review on the literature will be presented in the following categories:

- Definitions of FTC and FDI
- Different theories, models and hypotheses
- Existing data and empirical findings
- Measurement techniques and instruments for hypotheses testing

1.2.1 Definitions of Fault Tolerant Control and Fault Detection and Isolation

Since the research will form part of a fault tolerant control architecture, the definition of a fault tolerant system and the corresponding terminology must be understood. The distinction between a fault and a failure is discussed in [4], where a “fault is an unpermitted deviation of at least one characteristic property (feature) of the system from the acceptable, usual, standard condition” and a “failure is a permanent interruption of a system’s ability to perform a required function under specified operating conditions”.

In this research only actuator faults are considered but sensor faults can easily be incorporated into the FDI systems. The reason for this decision is to focus attention on the actuator failure information that is required for the control allocation system. An aircraft has several actuators which may fail at any time on board the aircraft. There are an infinite number of ways in which an actuator can fail. Four of the most common types of operating modes are described below, of which three are failure modes.

- (a) No-fault - This mode is the nominal operating mode of an actuator. The actuator follows the desired deflection accurately (figure 1.1a).
- (b) Floating - The control surface can become detached from the control actuator or can become completely ineffective. This creates a surface that floats around the zero-deflection position (figure 1.1b). This can be described as an additive fault.
- (c) Locked-in-place - The control surface can become stuck at an arbitrary deflection position (figure 1.1c). This can be described as an additive fault.
- (d) Effectiveness - The effectiveness of the actuator can become distorted, resulting in a larger or smaller deflection than desired (figure 1.1d). This can be described as a multiplicative fault.

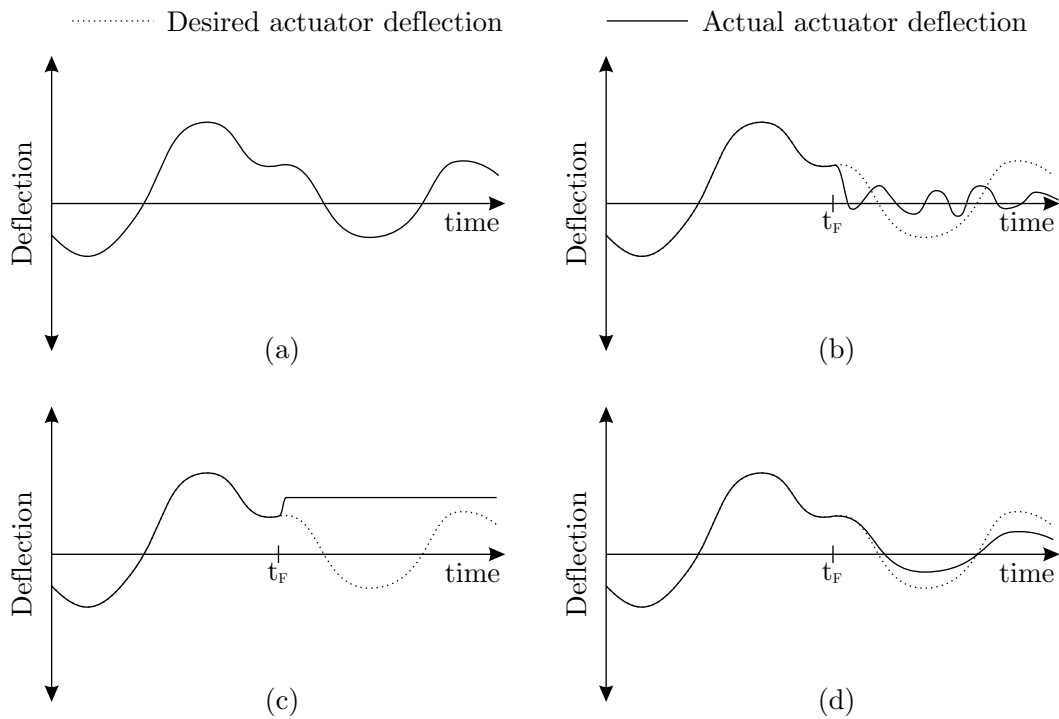


Figure 1.1: Different fault modes: (a) no-fault; (b) floating fault; (c) locked-in-place fault; (d) effectiveness fault. t_F indicates the start of the fault.

Fault tolerant control is a control architecture that is capable of handling a fault or multiple faults while still operating the system at an acceptable performance level. There are several different fault tolerant control schemes that mainly focus on robust control design or adaptive control design. However, for robust control, performance degradation after a fault occurred is a significant issue, whereas for adaptive control, stability assurance is a hurdle [5].

FTC systems usually have several loops in which fault tolerance is applied. In the inner loop an FDI process, which supplies the control allocator with actuator health information, can be used so that the fault affects the performance of the aircraft as little as possible. This is a first defence for faults and will be the method implied in this research. The architecture for this type of first defence FTC is shown in figure 1.2. When performance degradation is such that it becomes unacceptable, other fault tolerant processes such as an adaptive controller can be adapted until performance and stability is restored [6].

A more comprehensive bibliographic review on the topic can be found in [7].

Fault detection and isolation systems (also known as a fault detection and diagnosis systems) are concerned with the following three tasks:

- 1 Fault detection - It is necessary for the system to detect that something has gone wrong, even if it cannot directly determine where the fault is.

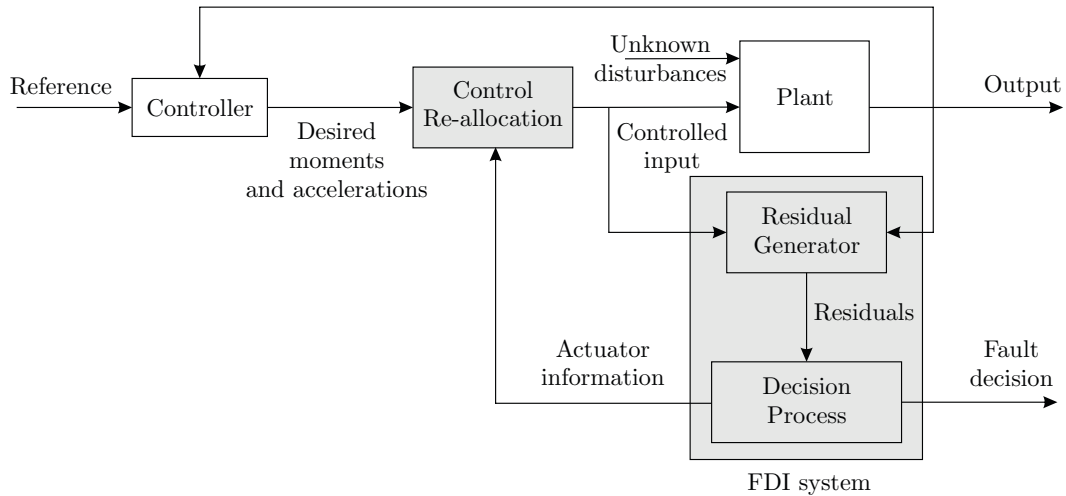


Figure 1.2: FTC architecture with a FDI and control re-allocation module.

- 2 Fault isolation - It is the process by which it is determined what part of the system is operating in a faulty manner, for example, “the left elevator is faulty”.
- 3 Fault identification - The extent of the fault is determined and categorised, for example, “the left flap is stuck at -1.3 degrees” or “the right rudder is floating with an amplitude of two degrees”.

In this research it is of paramount importance to implement all three tasks so that the necessary information can be supplied to the control allocation system. The basic thought process of the desired system after a fault occurs is shown in figure 1.3.

As seen in figure 1.3, the sensor outputs and control inputs are the only available information from which FDI can be done. These outputs and inputs are used by a residual generator to create residuals. Residuals exhibit specific statistical characteristics that are extracted by calculations of decision statistics. The decision statistics are then used to make a decision about detecting the fault, isolating the fault and identifying the fault. The three responsibilities of detection, isolation and identification may be executed in parallel or in series. In some FDI systems, a single detection indicates that a fault is present, as well as its position.

The FDI scheme is usually run on-line, in real time. In most systems, the fault detection algorithm is running continuously, while the isolation task is activated only upon the detection of the fault [8]. There are also two families of FDI systems, namely active and passive FDI systems. Active FDI will constantly monitor the system while artificially exciting the UAV [9; 5; 10; 11; 12] through the aircraft’s actuators. This method decreases the time it takes to detect a fault and can also guarantee fault detection in a set amount of time [13]. The disadvantage of active fault detection is that more energy is used to excite the actuators, the actuators wear out faster due to more use, and some level of performance is lost. The second family is passive FDI systems, which also constantly monitor the health of the actuators, but do not artificially excite the actuators to assist the FDI process [14]. Most FDI techniques can be tuned to be either an active or passive FDI system.

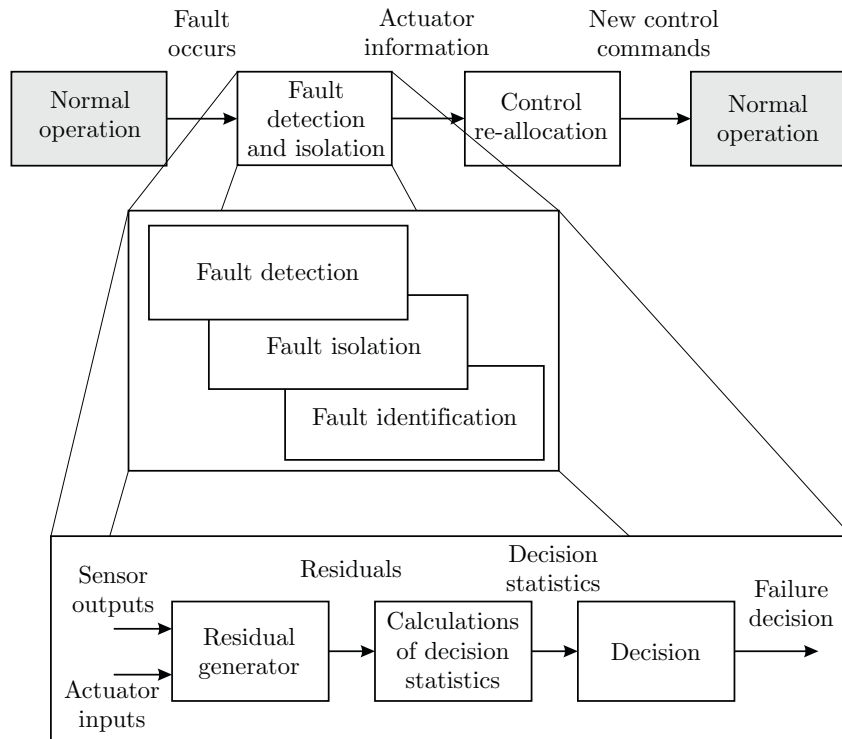


Figure 1.3: Thought process for FDI and control allocation.

Some methods and definitions of control allocation are discussed in [6; 15; 16; 17]. There is also a distinction between passive and active FTCs, and [7] is an excellent starting point for a bibliographic review on the topic. More definitions of FTC, FDI and control allocation can be found in [18].

1.2.2 Different Theories, Models and Hypotheses

Several fault tolerant control methods exist and for the research done for this thesis, control re-allocation with a FDI module is the required FTC architecture. An in-depth analysis of the topic is beyond the scope of this study. For a comprehensive list of different FTC methods available, consult [7].

There are also several FDI methods available. These FDI methods can depend on a model based approach or a data based approach. A mathematical model of the aircraft is available and therefore a model based approach is more appropriate for this research. The model based approaches can further be classified by their outcome as a qualitative or quantitative method. A qualitative method can use fuzzy logic or other decision processes to give a measure of fault quality, for example “the left rudder is stuck at a high angle”. The quantitative methods apply numerical values to their decisions such as “the right aileron is stuck at -3 degrees”. The control re-allocation system requires quantitative information to operate and therefore a quantitative method for FDI is an obvious choice.

Several techniques that address the problem of quantitative, model based FDI include [2]:

- **State estimation techniques:** A fault usually changes the expected state of a system in an additive way. State estimation techniques use the innovations (measurement residual) of the estimators as a means to quantify the discrepancy between the expected behaviour of the system and the observed behaviour. Most faults can be classified as additive and therefore makes this method attractive.
 - **Observer based approach** [19] - The residuals from an observer also qualify for use in an FDI system. There are ways of decoupling disturbances with “unknown input” design methods. The design of the observer can be used to optimise the residuals for FDI as well as to control the observer dynamics.
 - **Kalman filter (KF) based** [20] - A multiple model adaptive estimation (MMAE) technique uses a bank of Kalman filters to estimate the probability of a specific fault scenario. The MMAE method can be applied in practice as long as the expected faults can be hypothesised by a reasonable number of KFs.
- **Parameter estimation techniques** [21]: Parameter estimation is an intuitive approach of determining multiplicative faults. The dynamic parameters of the system are estimated and compared with the nominal values of a fault-free system model. Parameter Estimation is more reliable than analytical redundancy methods, but it requires more computational power and external excitation.
 - **Recursive least squares** [22] - The Recursive least squares (RLS) filter is an algorithm which recursively finds the filter coefficients that minimize a weighted linear least squares cost function relating to the input signals.
 - **Regression analysis** [21] - The method looks at the relationship between different dependent and independent variables to find the best suited set of parameters that describe this relationship. The least square method mentioned above is one of the many regression analysis techniques available for parameter estimation.
- **Parity space techniques** [7]: The parity space relations are the relationships found between the inputs and outputs of a system and are used as residuals for the FDI system. These relations are obtained from the system’s rearranged mathematical model subject to a linear transformation. The design freedom obtained through the transformation can be used to decouple disturbances and improve fault isolation.
 - **Input-Output based** [8] - If the system can be described by a transfer function relating the output to the input, then residuals can be created with this relationship. The limitation of this method is that the number of sensors required must be equal to or more than the number of faults hypothesis to diagnose the faults. This is not the case with redundant actuators on a typical aircraft.
 - **State space based** [23] - The output of a system is a function of the system states, as well as the input to the system. If the null space to the observability matrix can be obtained, then a relationship between the outputs and inputs of the system can be found that is decoupled from the system states. The advantage

of this approach over the basic input-output based approach is that more faults can be diagnosed than the number of sensors on board the aircraft.

1.2.3 Existing Data and Empirical Findings

It is important to test theoretical principles on real-life situations to further our understanding of the topic and offer practical solutions to everyday problems. It is also important to compare the work done here with that done internationally so that the significance of this research may be quantified.

The simulation results from most of the techniques discussed above were analysed. For the RLS technique [22] a six-degree-of-freedom, F-16/MATV simulation was run. It shows that the recursive least squares algorithm yields poor results when there is a poorly conditioned observation matrix. It also shows that modifying the RLS to a modified sequential least squares method, improves detection performance considerably.

In [20] it shows that the performance of a bank of Kalman filters (used in a multiple model adaptive estimation scheme) is unacceptable if it is not tuned to some degree. Some of the tuning methods that were proposed are: direct pseudo noise on the process noise covariance matrix's diagonal elements; direct pseudo noise on the measurement covariance matrix; and tuning for actuator uncertainty. These methods increase the reliability of the detection at the cost of required computing power. Another proposed method is given in [2] where a bank of extended Kalman filters (EKF) is used instead of a bank of linear Kalman filters. The algorithm, combined with an active supervision module, is shown to offer fast and accurate FDI at the expense of additional processing power.

In all of the literature, extensive simulations were performed and in several instances test were done on actual flights. Most methods discussed here used some sort of tuning method or robust technique to enhance the reliability of the specific FDI method. There are also several hybrid systems where more than one technique is incorporated that improves the fault detection abilities. The results of this research are compared with literature in chapter 6.

1.2.4 Measuring Techniques and Instruments for Hypotheses Testing

Accurate simulations can be used as a preliminary measuring tool. In [5] a FTC system is tested on a model that represents the lateral-directional dynamics of a McDonnell F-4C Phantom flying at Mach 0.6 at an altitude of 35 000 ft. Other methods for testing specific signals include the evaluation of the residual vectors in [9] by using a cumulative sum (CUSUM) or a Generalized Likelihood Ratio (GLR) test. MATLAB[®] is also an excellent simulation tool. The three simulation cases in [24] were performed in MATLAB[®] 6.1 running on a 800 MHz Pentium III computer.

At the ESL MATLAB[®] R2008b is available on an Intel[®] Core[™] i5 CPU @ 2.8 GHz with 4.0 GB RAM. This program will be used extensively to simulate the dynamics of the aircraft and the performance of the FDI methods.

For the practical flight tests in this research a Meraka Modular UAV, that was developed at the Council for Scientific and Industrial Research (CSIR), will be used. The aircraft is equipped with several sensors in its avionics that are used for state estimation purposes. Several of the sensors' data will be used as an input to the FDI process. The sensors incorporated by the avionics on board the Meraka Modular UAV are:

- Accelerometers & rate gyros - A High Precision tri-axis Inertial Sensor from Analog Devices will be used (model number ADIS16350).
- GPS - A Novatel differential GPS system will be used.
- Angle-of-attack & side-slip angle sensor - The 100400 Mini Air data boom from Space Age Control will be used to measure both the angle of attack and sideslip angles.
- Static-pitot tube - The 100400 Mini Air data boom also houses a pitot tube used to determine the static pressure and the airspeed of the UAV.

The mathematical model and other details of the aircraft will be discussed in chapter 2.

1.3 Research Problem and Objectives

There is a need at the ESL for FDI systems for their unmanned automated technology such as the Meraka Modular UAV. The Meraka Modular UAV can be used as a test-bed for the development of a suitable FDI. It should then be possible to use the FDI on other unmanned vehicles by changing a minimum number of parameters. The other vehicles at the ESL will then be able to benefit from the FDI system developed in this research with minimal extra effort.

By creating more than one FDI system the advantages and disadvantages of the systems can be compared, combined and a great deal of understanding can sprout from the evaluation. In section 1.2.2 it was noted that there are three main methodologies for designing an FDI in a model based, quantitative manner. However the faults that will be focused on are categorised as additive faults (see section 1.2.2) and consequently a parameter estimation methodology cannot be used and leaves only the state estimator and parity space method. One FDI method in each of these two categories will be used to develop independent FDI systems.

The Kalman filter based method is an attractive technique as the estimators aim to produce optimal estimates. Some statistical information regarding the sensors and processes of the aircraft are known and can be used by the Kalman filters. Extended Kalman filters are also used in the state estimation processes incorporated by the ESL on their vehicles. The literature is rich in articles and dissertations covering linear and extended Kalman filter based FDI systems and makes for excellent material for comparison [25].

Both the input-output and state space methods, which fall under the parity space based approach, are covered in [8]. The input-output based method is an excellent FDI development method, but problems arise when more faults can occur than the number of useful detection

sensors. If this is the case the state space based method can be used and allows for more design freedom with the use of optimisation techniques.

The research problem can therefore be stated as the problem of delivering reliable information regarding the current state of the aircraft actuators. This information can then be used to determine the optimal control allocation for the UAV. The objectives of this research will be categorised as follows:

- Creating two fault detection and isolation systems using two of the techniques mentioned in the literature review.
- Making both systems usable in the FTC architecture developed in the ESL for the Meraka Modular UAV at Stellenbosch University.
- Testing the system in both a simulation environment and actual test flight environment.
- Analysing and comparing the two FDI methods.

1.4 Thesis Outline

Chapter one gave an introduction to where fault detection and isolation finds itself in the general architecture of a fault tolerant control scheme. A brief literature review covered the basic concepts and philosophies regarding fault tolerant control and fault detection and isolation. The chapter was concluded with the research problem and the objectives of the research.

Chapter two is concerned with deriving the necessary mathematics that will be used in the research. This involves setting up all the required conventions and investigating the dynamics of the Meraka Modular UAV.

Chapter three introduces the development of the first FDI process that incorporates the use of a bank of Kalman filters. The linear Kalman filters will also be replaced by extended Kalman filters, thereby improving the FDI system. The chapter will conclude with simulation results that show the expected performance of the bank of Kalman filters FDI method.

Chapter four describes the development of the second FDI process that uses a parity space approach to create the residuals that will be used for FDI. The method will be optimised for fault detection and isolation whereafter a CUSUM procedure will be introduced, which assists the decision making process. Finally performance simulations and conclusions regarding this method are presented.

Chapter five is concerned with the test flight conducted at the Helderberg Radio Flyers Club, which tested the performance of both the FDI methods. The physical aircraft actuators and their effects on the expected performance of the FDI are also discussed in this chapter.

Chapter six compares the two FDI methods and draws conclusions from the simulated results and flight tests that were conducted. Lastly, the FDI performance is compared to other literature simulations.

Chapter seven provides valuable recommendations regarding practical considerations and proposed future research and applications. The research conclusions completes the end of the thesis.

Chapter 2

Aircraft Model

For a quantitative model based FDI approach, a transfer function or state space representation of the aircraft is required. In order to obtain this, it is first necessary to obtain the equations of motion for the aircraft. To derive the non-linear aircraft model, specific assumptions must be made and several reference frames defined. In this chapter the inertial, body and wind frames, as well as the gravitational, aerodynamic and thrust model used to describe the non-linear aircraft dynamics for the Meraka Modular UAV, will be defined.

2.1 Reference Frames Definitions

There are three reference frames that must be defined in order to develop a simple six degree of freedom, non-linear model for the aircraft dynamics [26]. The first is the inertial reference frame in which the laws of Newton are applicable. The second is the body reference frame that coincides with the aircraft frame, and lastly the wind frame that describes the direction of airflow over the body of the aircraft.

2.1.1 Inertial Reference Frame

In this research, the earth will be regarded as flat and non-rotating and can therefore be regarded as an inertial reference frame. This is an acceptable approximation as the motion of the Modular UAV will be localised and be relatively slow (22 m/s). This simplifies the dynamic model for the aircraft quite substantially without significant loss of accuracy [3] for the purpose of FDI. The frame is defined as fixed to the earth at some convenient location such as the starting centre of gravity (CG) point of the aircraft before take-off. The x-axis is pointed north, whereas the y-axis points east and the z-axis points downwards to complete the right-hand convention. This definition is depicted in figure 2.1. The subscript used for the inertial reference frame will be I .

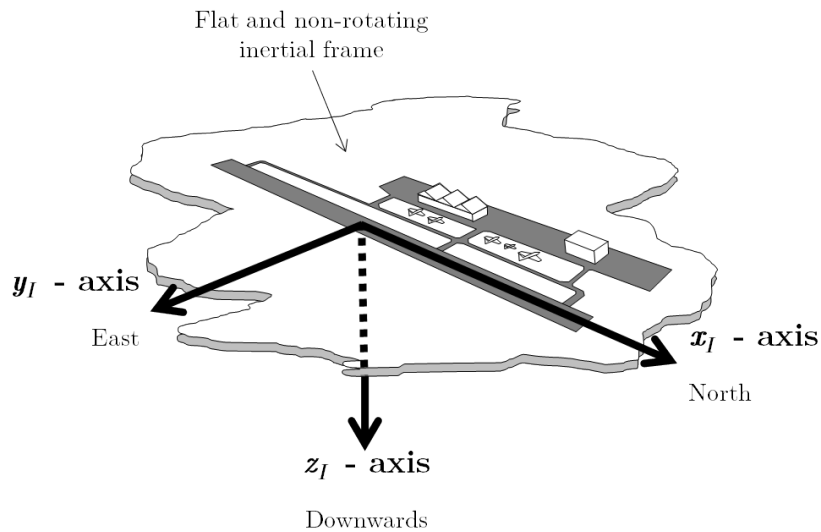


Figure 2.1: Inertial reference frame.

2.1.2 Body Reference Frame

The body reference frame is required so that the forces and moments can be mapped in a logical manner to the resulting motions of the aircraft. The centre point of the frame coincides with the CG of the aircraft. This is not always the case, but it is generally placed at the CG and will be done this way in this research.

The x-axis points forward and comes out the nose of the aircraft, while the y-axis points out along the right wing as seen in figure 2.2. It must be noted that the x-axis does not coincide with one of the principal axes of the aircraft. Instead it coincides with the originally aligned equilibrium direction of the velocity vector of the aircraft [27]. The z-axis completes the right-hand convention by pointing downwards so that the x_b - z_b -plane is the aircraft's plane of symmetry. The convention is also shown in figure 2.2. The subscript used for the body reference frame will be b .

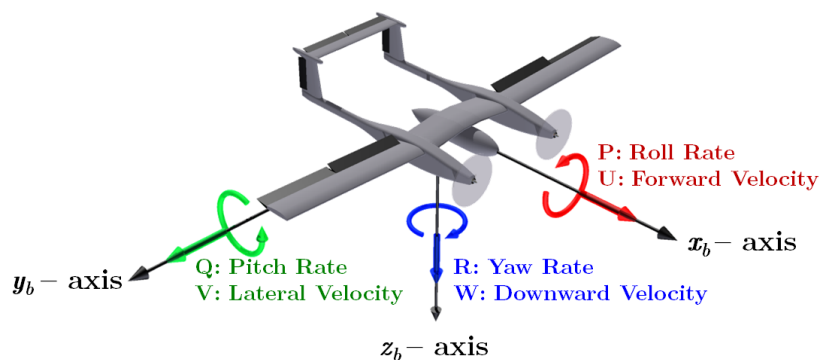


Figure 2.2: Body reference frame with velocity notations.

2.1.3 Wind Reference Frame

The wind frame is sometimes also referred to as the stability frame or the aerodynamic frame [28]. The aerodynamic forces that act on the body of the aircraft are produced by the air flowing over the airframe. The air flow velocity is described by \mathbf{V} and the direction of \mathbf{V} can be described by two angles relative to the body frame of the aircraft. The two angles are the angle of attack, α , and side slip angle, β . These angles parameterises the change in the air flow pattern over the airframe that consequently produces different aerodynamic forces and moments.

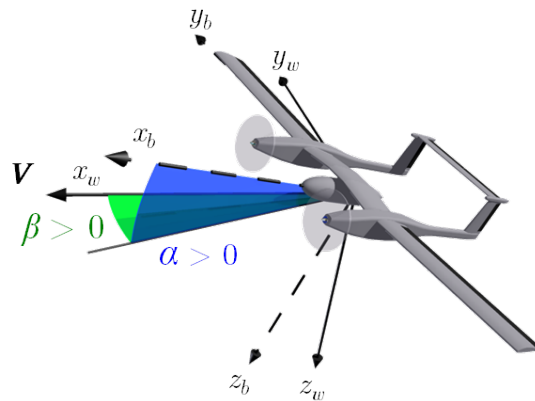


Figure 2.3: Wind reference frame, angle of attack and side slip angle, $\alpha > 0$ and $\beta > 0$.

The wind reference frame can be defined by lining up the x_w -axis with the velocity vector, \mathbf{V} . As shown in figure 2.3 the angle of attack (α) is the angle between the projection of \mathbf{V} onto the x_b-z_b -plane and the x_b -axis. The side slip angle (β) is the angle between the projection of the airspeed vector \mathbf{V} onto the x_b-z_b -plane and the airspeed vector itself [2]. The y-axis and z-axis of the wind reference frame are directed according to these angles as illustrated in figure 2.3. The subscript used for the wind reference frame will be w .

2.2 Notation

The components of the total instantaneous values of the linear velocities resolved into the body reference frame are

- U - Forward velocity
- V - Lateral velocity
- W - Downward velocity

and the angular rates are

- P - Angular rate around the x_b -axis
- Q - Angular rate around the y_b -axis
- R - Angular rate around the z_b -axis

These vectors are shown in figure 2.2.

The notation that will be used for the forces and moments acting on the body of the aircraft is provided in figure 2.4. The forces are

- X - Axial force
- Y - Lateral force
- Z - Normal force

and the moments are

- L - Rolling moment
- M - Pitching moment
- N - Yawing moment

There are eight control surfaces consisting of two ailerons, two flaps, two rudders and two elevators. The control surface deflection angles are $\delta_A, \delta_E, \delta_F, \delta_R$ respectively. A distinction will be made between the left and right actuator by adding an l or r suffix to the subscript according to whether it is left or right (such as δ_{Ar} is the right aileron) as seen from behind the aircraft. Figure 2.4 shows the control surfaces and their deflections, where a negative deflection causes a positive moment around the body reference frame.

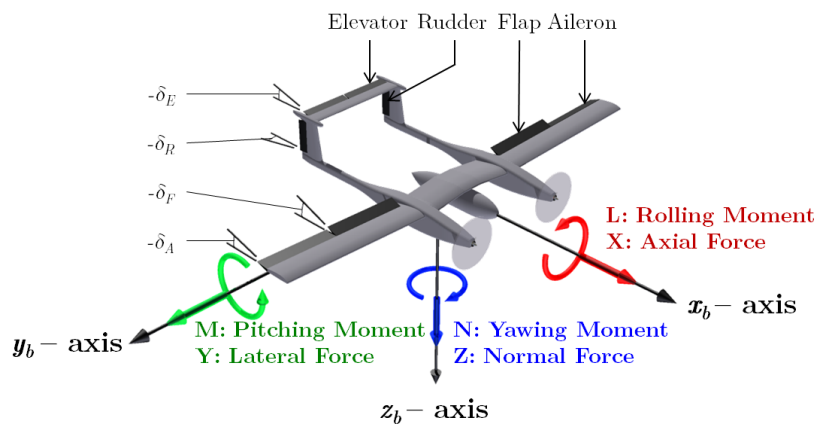


Figure 2.4: Body reference frame with force and moment notations.

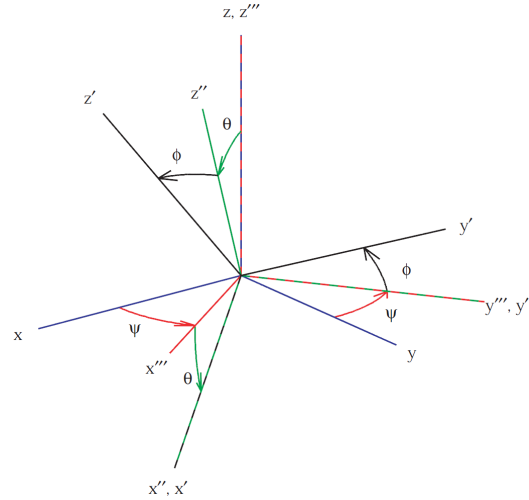


Figure 2.5: Euler angle transformation sequence (3,2,1) in 3D [1].

2.3 Frame Transformations

The aerodynamics of the aircraft are best described in the wind reference frame while the gravitational forces and thrust are described better in the body frame. The position and attitude of the aircraft are however expressed in the inertial reference frame. It is therefore important that vectors should be able to be mapped from one reference frame to another. There are several methods to accomplish this, but three methods worth noting are by using rotation matrices, Euler angles and quaternions. In this research, Euler angles will be used and converted to rotation matrices. Quaternions have benefits (see section 2.3.5) but the control system for the Meraka Modular UAV was developed without their use and subsequently will not be used for the FDI system.

2.3.1 Euler Angles

Using Euler angles is a simple and understandable method used for frame transformation and is therefore a popular choice [1]. The Euler angle transformation is parameterised by three consecutive rotations. There are several different possible non-commutable rotation sequences to describe a specific transformation. The sequence that will be used in this research is the Euler 3-2-1 rotation sequence. This sequence is the same as what is used in the other systems developed at the ESL [3].

In the case of the aircraft attitude the inertial reference frame will be the starting frame and the body frame of the aircraft will be the transformed frame. The angles Ψ , Θ and Φ are called the yaw, pitch and roll angles respectively and they are displayed in figure 2.6 in order of rotation sequence from left to right. This parameterisation has singularities at pitch values of $\Theta = n\pi + \frac{\pi}{2}$ for $n \in \mathbb{Z}$ [1]. At these points, changes in yaw and roll constitute the same motion. This should however not be problematic in the context of this research as it is assumed that the aircraft stays within $|\Theta| \ll \frac{\pi}{2}$.

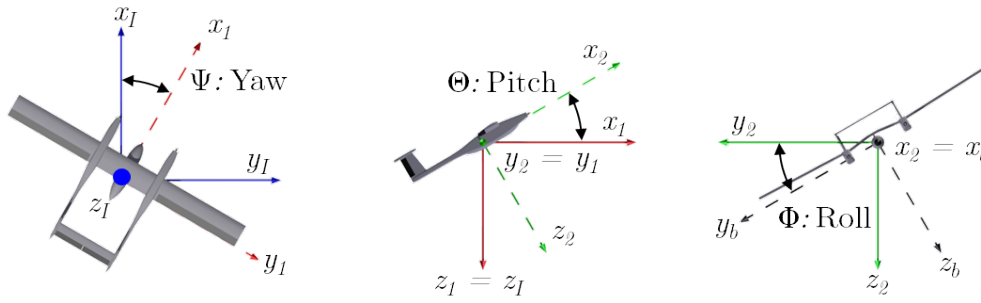


Figure 2.6: Euler angles and the frame transformation.

2.3.2 Rotation Matrices

The Euler angles described in section 2.3.1 are helpful but do not work well with column vectors. To solve this problem Euler angles are converted to rotation matrices that can readily be applied to column vectors to transform them from one reference frame to another.

When \mathbf{c}_I is taken as a column vector in the inertial reference frame and \mathbf{c}_b is taken as a column vector in the body reference frame, the Euler 3-2-1 sequence is realised by [1]

$$\mathbf{c}_I = R_{321}\mathbf{c}_b \quad (2.3.1)$$

$$\text{where } R_{321} = \begin{bmatrix} c_\Theta c_\Psi & c_\Theta s_\Psi & -s_\Theta \\ s_\Phi s_\Theta c_\Psi - c_\Phi s_\Psi & s_\Phi s_\Theta s_\Psi + c_\Phi c_\Psi & c_\Theta s_\Phi \\ c_\Phi s_\Theta c_\Psi + s_\Phi s_\Psi & c_\Phi s_\Theta s_\Psi - s_\Phi c_\Psi & c_\Theta c_\Phi \end{bmatrix} \quad (2.3.2)$$

$$\text{and } s_x = \sin x \quad (2.3.3)$$

$$c_x = \cos x \quad (2.3.4)$$

The matrix R_{321} is also called the direction cosine matrix (DCM). It is shown in [1] that the inverse of R_{321} transforms the body frame to the inertial frame and that the inverse is also equal to its transpose.

2.3.3 Position and Attitude Dynamics

The position of the airplane can be described by the aircraft's North, East and downward position. The dynamics of these positions are given by [29]

$$\begin{bmatrix} \dot{N} \\ \dot{E} \\ \dot{D} \end{bmatrix} = \begin{bmatrix} c_\Psi c_\Theta & c_\Psi s_\Theta s_\Phi - s_\Psi c_\Phi & c_\Psi s_\Theta c_\Phi + s_\Psi s_\Phi \\ s_\Psi c_\Theta & s_\Psi s_\Theta s_\Phi + c_\Psi c_\Phi & s_\Psi s_\Theta c_\Phi - c_\Psi s_\Phi \\ -s_\Theta & c_\Theta s_\Phi & c_\Theta c_\Phi \end{bmatrix} \begin{bmatrix} U \\ V \\ W \end{bmatrix} \quad (2.3.5)$$

where

$$c_x = \cos x \quad (2.3.6)$$

$$s_x = \sin x \quad (2.3.7)$$

The time rate of change of the Euler angles with respect to the other kinematic states are governed by the derivation found in [26] as

$$\begin{bmatrix} \dot{\Phi} \\ \dot{\Theta} \\ \dot{\Psi} \end{bmatrix} = \begin{bmatrix} 1 & \sin \Phi \tan \Theta & \cos \Phi \tan \Theta \\ 0 & \cos \Phi & -\sin \Phi \\ 0 & \sin \Phi \sec \Theta & \cos \Phi \sec \Theta \end{bmatrix} \begin{bmatrix} P \\ Q \\ R \end{bmatrix} \quad \Theta \neq n\pi + \frac{\pi}{2} \quad n \in \mathbb{Z} \quad (2.3.8)$$

2.3.4 Velocity Transformations

It is helpful to break down the velocity vector \mathbf{V} into its body-referenced components using the angle of attack and side slip angles, and vice versa. The components can be determined by investigating figure 2.3 as

$$\begin{bmatrix} U \\ V \\ W \end{bmatrix} = \begin{bmatrix} \cos(\beta) \cos(\alpha) \\ \cos(\beta) \sin(\alpha) \\ \sin(\beta) \end{bmatrix} |\mathbf{V}| \quad (2.3.9)$$

and vice versa

$$\left. \begin{aligned} \alpha &= \arctan\left(\frac{W}{U}\right) \\ \beta &= \arctan\left(\frac{V}{U} \cos(\alpha)\right) \end{aligned} \right\} U \neq 0 \quad (2.3.10)$$

2.3.5 Quaternions

An unwanted consequence of using Euler angles is the singularity at $\Theta = n\pi + \frac{\pi}{2}$ for $n \in \mathbb{Z}$. Quaternions are superior to Euler angles in that they do not display this singularity; however a quaternion transformation between two reference frames is described by four parameters instead of three. As stated previously, quaternions will not be used in this research, so that it conforms to the systems being developed for the Meraka Modular UAV at the ESL. In [1] it is shown that quaternions, Euler angles and rotation matrices can be used interchangeably should the need arise to do so.

2.4 Assumptions

There are six assumptions that must be made before deriving the equations of motion [27]:

1. *The axes x_b and z_b lie in the plane of symmetry of the aircraft and the products of inertia I_{xy} and I_{yz} are equal to zero.* The direction of x_b is generally not along a principal axis, hence $I_{xz} \neq 0$. For the aircraft used in this research however, the inertia tensor element I_{xz} is negligible compared to the rest of the elements.
2. *The mass of the aircraft remains constant throughout the dynamic analysis.* In practice this is not true as there can be cargo such as equipment, ammunition and projectiles loading and unloading during the course of the flight. There is also the inevitable consumption of fuel in most aircraft that reduces the mass of the aircraft during flight. The Meraka Modular UAV uses battery powered motors and no in-flight loading or unloading is done. Therefore the assumption of constant mass is accurate.

3. *The aircraft is a rigid body.* This means that any two points on or within the aircraft will remain stationary relative to one another. This greatly simplifies the equations of motion.
4. *The earth is an inertial reference, and unless otherwise stated, the atmosphere is fixed with respect to the earth.* This assumption is valid for the purpose of this research as it is generally accepted that the gyros and accelerometers on the aircraft cannot discern the angular velocity or accelerations of the earth (not to be confused with gravitational acceleration).
5. *The perturbations from equilibrium state are small.* With this assumption products of small variations can be ignored and small angle assumptions can be made for the relative angles between the equilibrium and disturbed axes. This assumption has been very successful in simplifying the linearisation process without too much loss of accuracy [26].
6. *The airflow over the body of the aircraft is quasi-steady.* Quasi-steady flow assumes the airflow changes instantaneously when the aircraft is disturbed from its equilibrium. This assumption is adequate for low Mach numbers (<0.8) and allows all derivatives with respect to the rates of change of velocities to be omitted when setting up an aerodynamic model of the aircraft.

2.5 Equations of Rigid-Body Motion

In the development of the equations of rigid-body motion, the assumption will be made that the aircraft will be flying in a localised area at low velocity. The flat-earth, non-rotating inertial reference frame simplifies these equations as the effects due to the Coriolis acceleration and centripetal acceleration of the earth can be ignored. In the inertial reference frame the laws of Newton apply.

2.5.1 Equations of Forces

The translation of a rigid body is described by its momentum. Newton's second law relates the change of momentum (the product of the velocity of its CG and its mass) to an external force acting on the body. This is stated as: the summation of all the forces acting on a rigid body equals the time rate of change of its momentum [30]. It can be written as

$$\sum_j \mathbf{F}_j = \left(\frac{d\mathbf{p}_b}{dt} \right)_I \quad (2.5.1)$$

$$= \frac{d}{dt} (m\mathbf{V}_b)_I \quad (2.5.2)$$

where j represents all the forces acting on the aircraft and \mathbf{p}_b is the momentum. The forces are however acting on the rotating body of the aircraft and it would be convenient to have

equation 2.5.2 in terms of the body reference frame. The relation then becomes [30]

$$\sum_j \mathbf{F}_j = \frac{d}{dt} (m\mathbf{V}_b)_b + \boldsymbol{\Omega}_b \times \mathbf{p}_b \quad (2.5.3)$$

$$= \frac{d}{dt} (m\mathbf{V}_b)_b + \boldsymbol{\Omega}_b \times (m\mathbf{V}_b) \quad (2.5.4)$$

where $\boldsymbol{\Omega}_b$ is the angular velocity vector of the aircraft.

2.5.2 Equations of Moments

The rotation of a rigid body is described by its angular motion. Newton's second law can be used to relate the change in angular velocity to the sum of external moments acting on the aircraft body. This can be more formally stated as: the summation of all the moments acting on a rigid body equals the time rate of change of its angular momentum [30]. It can be written as

$$\sum_j \mathbf{M}_j = \left(\frac{d\mathbf{H}_b}{dt} \right)_I \quad (2.5.5)$$

$$= \frac{d}{dt} (\boldsymbol{\Omega}_b)_I \quad (2.5.6)$$

where \mathbf{H}_b is the angular momentum and the angular rate vector

$$\boldsymbol{\Omega} = \begin{bmatrix} P \\ Q \\ R \end{bmatrix} \quad (2.5.7)$$

and \mathbf{I}_b is the mass moment of inertia tensor that is written as

$$\mathbf{I}_b = \begin{bmatrix} I_{xx} & -I_{xy} & -I_{xz} \\ -I_{yz} & I_{yy} & -I_{yz} \\ -I_{zx} & -I_{zy} & I_{zz} \end{bmatrix} \quad (2.5.8)$$

According to the first assumption from section 2.4, the inertia tensor can be greatly simplified into the diagonal matrix

$$\mathbf{I}_b = \begin{bmatrix} I_{xx} & 0 & 0 \\ 0 & I_{yy} & 0 \\ 0 & 0 & I_{zz} \end{bmatrix} \quad (2.5.9)$$

For the same reason as with the external forces, it would be convenient to write equation 2.5.6 in terms of the body reference frame. The relation then becomes [30]

$$\sum_j \mathbf{M}_j = \left(\frac{d\mathbf{H}_b}{dt} \right)_b + \boldsymbol{\Omega}_b \times (\mathbf{H}_b) \quad (2.5.10)$$

$$= \frac{d}{dt} (\boldsymbol{\Omega}_b)_b + \boldsymbol{\Omega}_b \times (\boldsymbol{\Omega}_b \mathbf{I}_b) \quad (2.5.11)$$

2.5.3 General Equations

The two equations (Eq. 2.5.4 and Eq. 2.5.11) are written in vector form. If the assumption holds for a symmetrical aircraft body around the x_b - z_b -plane, these two equations can be expanded into their scalar forms to produce

$$X = m(\dot{U} + WQ - VR) \quad (2.5.12)$$

$$Y = m(\dot{V} + UR - WP) \quad (2.5.13)$$

$$Z = m(\dot{W} + VP - UQ) \quad (2.5.14)$$

$$L = \dot{P}I_{xx} + QR(I_{zz} - I_{yy}) \quad (2.5.15)$$

$$M = \dot{Q}I_{yy} + PR(I_{xx} - I_{zz}) \quad (2.5.16)$$

$$N = \dot{R}I_{zz} + PQ(I_{yy} - I_{xx}) \quad (2.5.17)$$

Each of the equations 2.5.12 to 2.5.17 are composed of aerodynamic, thrust and gravitational forces and moments so that

$$X = X_a + X_t + X_g \quad (2.5.18)$$

$$Y = Y_a + Y_t + Y_g \quad (2.5.19)$$

$$Z = Z_a + Z_t + Z_g \quad (2.5.20)$$

$$L = L_a + L_t + L_g \quad (2.5.21)$$

$$M = M_a + M_t + M_g \quad (2.5.22)$$

$$N = N_a + N_t + N_g \quad (2.5.23)$$

2.6 Aerodynamic Forces and Moments

In this research it is assumed that the aerodynamic stability and control derivatives will be made available by the system identification process running on the aircraft's computer or from off-line parameter estimation techniques. Therefore the research will not be accompanied by an in-depth analysis of these derivatives. Further reading on this topic can be found in [3; 31; 28; 26; 27]. However, a brief explanation of the analysis will be presented.

Aerodynamic forces and moments are produced by a pressure difference over the airfoils of the aircraft. Actuators assist in changing the airflow over the airfoil surface to induce certain desired forces and moments. Because air pressure is the driving force behind these dynamics, Bernoulli's equation and the continuity principle for incompressible fluids are fundamental. It states that the sum of the static (p_{static}) and dynamic pressure ($\bar{q} = 0.5\rho|\mathbf{V}|^2$) stay constant

$$p_{static} + \frac{1}{2}\rho|\mathbf{V}|^2 = \mathbb{C} \quad (2.6.1)$$

where $|\mathbf{V}|$ is the free stream velocity.

It can be shown [31] that the resultant aerodynamic force (and moment) is proportional to the product of the dynamic pressure and the airfoil area (S).

$$F \propto \frac{1}{2}\rho|\mathbf{V}|^2 S \quad (2.6.2)$$

The moments are proportional to the product of the corresponding forces and relevant moment arms. The problem becomes finding the dimensionless coefficients of proportionality so that

$$X_a = C_X \left(\frac{1}{2} \rho |\mathbf{V}|^2 S \right) \quad (2.6.3)$$

$$Y_a = C_Y \left(\frac{1}{2} \rho |\mathbf{V}|^2 S \right) \quad (2.6.4)$$

$$Z_a = C_Z \left(\frac{1}{2} \rho |\mathbf{V}|^2 S \right) \quad (2.6.5)$$

$$L_a = C_L \left(\frac{1}{2} \rho |\mathbf{V}|^2 S \right) b \quad (2.6.6)$$

$$M_a = C_M \left(\frac{1}{2} \rho |\mathbf{V}|^2 S \right) \bar{c} \quad (2.6.7)$$

$$N_a = C_N \left(\frac{1}{2} \rho |\mathbf{V}|^2 S \right) b \quad (2.6.8)$$

where the moment arms b and \bar{c} are the wingspan and mean aerodynamic chord respectively. For the FDI analysis undertaken in this research, preliminary stability and control derivatives were determined using a program called Athena Vortex Lattice (AVL). AVL is a software program for aerodynamic and flight-dynamic analysis of rigid aircraft of arbitrary configuration developed at MIT. The values obtained through AVL corresponded well to wind tunnel results obtained by the CSIR (see section 2.9). With reference to [31; 27], before the aerodynamic forces can be applied to the aircraft in the body frame, a transformation of the drag and lift onto C_X and C_Z are required.

$$C_X = -C_d \cos \alpha + C_l \sin \alpha \quad (2.6.9)$$

$$C_Z = -C_d \sin \alpha - C_l \cos \alpha \quad (2.6.10)$$

Expanding the various coefficients produces

$$C_d = C_{d_0} + \frac{C_l^2}{\pi A e} \quad (2.6.11)$$

$$C_l = C_{l_0} + C_{l_\alpha} \alpha + \cancel{C_{l_\beta}} \beta + \frac{b}{2|\mathbf{V}|} \cancel{C_{l_P}} P + \frac{\bar{c}}{2|\mathbf{V}|} C_{l_Q} Q + \frac{b}{2|\mathbf{V}|} \cancel{C_{l_R}} R + \mathbf{C}_{l_\delta} \boldsymbol{\delta} \quad (2.6.12)$$

$$C_Y = \cancel{C_{Y_0}} + \cancel{C_{Y_\alpha}} \alpha + C_{Y_\beta} \beta + \frac{b}{2|\mathbf{V}|} C_{Y_P} P + \frac{\bar{c}}{2|\mathbf{V}|} \cancel{C_{Y_Q}} Q + \frac{b}{2|\mathbf{V}|} C_{Y_R} R + \mathbf{C}_{Y_\delta} \boldsymbol{\delta} \quad (2.6.13)$$

$$C_L = \cancel{C_{L_0}} + \cancel{C_{L_\alpha}} \alpha + C_{L_\beta} \beta + \frac{b}{2|\mathbf{V}|} C_{L_P} P + \frac{\bar{c}}{2|\mathbf{V}|} \cancel{C_{L_Q}} Q + \frac{b}{2|\mathbf{V}|} C_{L_R} R + \mathbf{C}_{L_\delta} \boldsymbol{\delta} \quad (2.6.14)$$

$$C_M = C_{M_0} + C_{M_\alpha} \alpha + \cancel{C_{M_\beta}} \beta + \frac{b}{2|\mathbf{V}|} \cancel{C_{M_P}} P + \frac{\bar{c}}{2|\mathbf{V}|} C_{M_Q} Q + \frac{b}{2|\mathbf{V}|} \cancel{C_{M_R}} R + \mathbf{C}_{M_\delta} \boldsymbol{\delta} \quad (2.6.15)$$

$$C_N = \cancel{C_{N_0}} + \cancel{C_{N_\alpha}} \alpha + C_{N_\beta} \beta + \frac{b}{2|\mathbf{V}|} C_{N_P} P + \frac{\bar{c}}{2|\mathbf{V}|} \cancel{C_{N_Q}} Q + \frac{b}{2|\mathbf{V}|} C_{N_R} R + \mathbf{C}_{N_\delta} \boldsymbol{\delta} \quad (2.6.16)$$

where the actuator vector

$$\boldsymbol{\delta} = \left[\delta_{Ar} \quad \delta_{Al} \quad \delta_{Er} \quad \delta_{El} \quad \delta_{Fr} \quad \delta_{Fl} \quad \delta_{Rr} \quad \delta_{Rl} \right]^T \quad (2.6.17)$$

represents the actuator deflections for the left and right ailerons, elevators, flaps and rudders. A and e are the aspect ratio of the wing and the Oswald efficiency factor respectively. Most

of the terms in equations 2.6.11 to 2.6.16 can be ignored [31] as indicated by the crossed out terms in these equations. The terms relating the actuator commands to the forces and moments are called the control derivatives (\mathbf{C}_{l_δ} , \mathbf{C}_{Y_δ} , \mathbf{C}_{L_δ} , \mathbf{C}_{M_δ} and \mathbf{C}_{N_δ}) while the rest are called stability derivatives.

The values for the derivatives that were obtained using AVL can be found in Appendix A.

2.7 Gravitational Forces and Moments

The gravitational model is assumed to create a uniform and constant force acting on the aircraft in the direction to the centre of the Earth. It is also assumed that the aircraft is small enough that no moment is created by the fluctuations in the gravitational field acting upon the aircraft. The components of the gravity force along the body reference frame are [27]:

$$X_g = -mg \sin \Theta \quad (2.7.1)$$

$$Y_g = mg \cos \Theta \sin \Phi \quad (2.7.2)$$

$$Z_g = mg \cos \Theta \cos \Phi \quad (2.7.3)$$

$$L_g = M_g = N_g = 0 \quad (2.7.4)$$

2.8 Engine Forces and Moments

The Meraka Modular UAV has two engines that are positioned symmetrically to one another around the x_b - z_b -plane and their rotors point in the x_b direction. The on board computer (OBC) of the aircraft controls the engines in such a way that the thrust generated by the rotors are equal. The total thrust vector is also assumed to run close enough through the CG so that any moments produced by the rotors are negligible. The resulting thrust equations are

$$X_t \approx T \quad (2.8.1)$$

$$0 = Y_t = Z_t = L_t = N_t = M_t \quad (2.8.2)$$

where T is the thrust magnitude.

2.9 Change in Aircraft Coefficients

Most aircraft control systems are designed to be robust to changes in aircraft coefficients. It is important to investigate whether empirical tests correspond with the mathematical model developed earlier so that the susceptibility of FDI error can be minimised in flight tests later.

The Defence, Peace, Safety and Security department at the CSIR in South Africa has done a number of wind tunnel tests on the Meraka Modular UAV. A scale model of the aircraft was placed in a wind tunnel and tested at different angles of α and β . The resulting

aerodynamic coefficients were recorded. The most important coefficients that were analysed were the coefficients $C_d, C_l, C_y, C_L, C_M, C_N$ from equations 2.6.11 to 2.6.16.

The single set of trim stability derivatives obtained through AVL was used in MATLAB[®] to find the solution to the aerodynamic coefficients while changing the values for α and β . The different results for all the coefficients are shown in figures 2.7 to 2.12. Note that in the mathematical model the coefficients C_d, C_l, C_M are not dependent on β and the coefficients C_y, C_L, C_N are not dependent on α .

In figure 2.7 the drag coefficient (C_d) is clearly seen to be quadratically dependent on α . It must be noted that C_d is quadratically dependent on α but significantly less on β . It should be borne in mind that the amplitude of the sideslip angle is usually less than angles of attack because of faster lateral poles relating to yaw rate. It can also be seen that for a positive angle of attack there is a good correspondence between the simulated and empirical values. The increase in the discrepancy when the angle of attack becomes negative is due to the fact that the MATLAB[®] solution is calculated with a single set of derivatives obtained in AVL, with the AVL simulation being run around a trim condition with positive angle of attack. More importantly, AVL does not take into account the change in parasitic drag. The parasitic drag of the UAV changes as the frontal area of the UAV changes, which can be described as a change in the angle of attack.

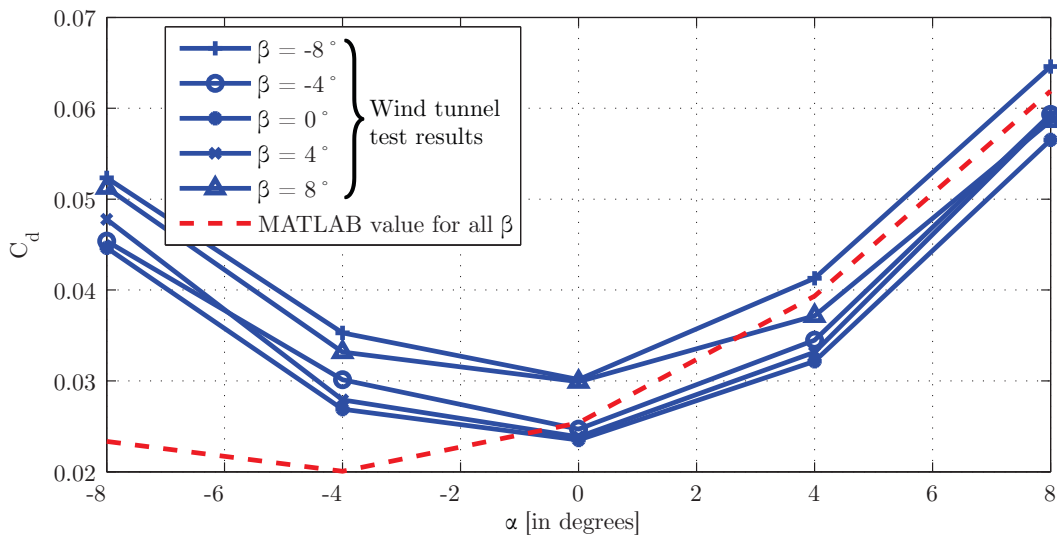


Figure 2.7: The effect of α on the aerodynamic coefficient C_d .

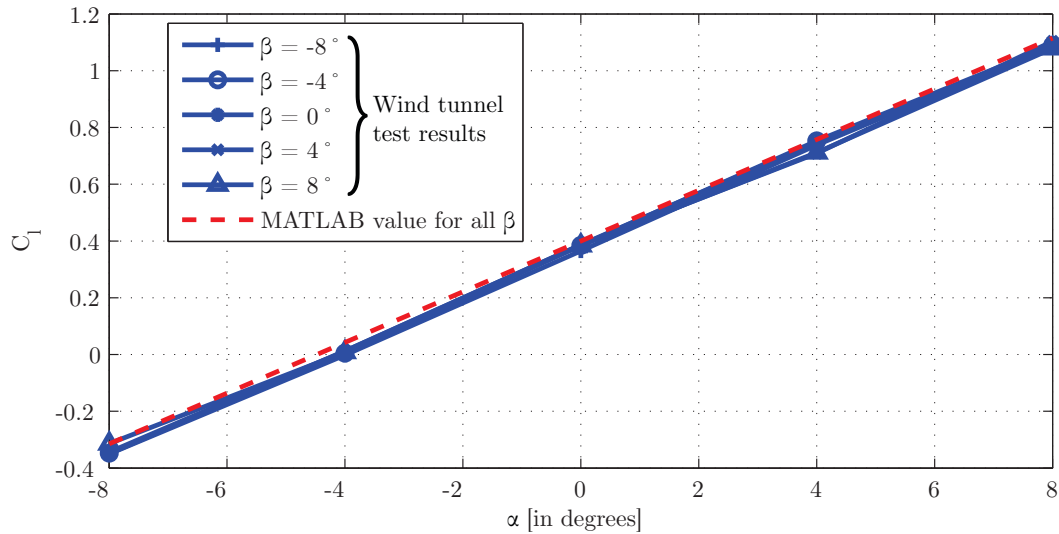


Figure 2.8: The effect of α on the aerodynamic coefficient C_l .

In figure 2.8 the independence of C_l in terms of β is clearly seen. The simulated values as well as the slope correspond well to the empirical values obtained through wind tunnel tests. For FDI analysis the parasitic drag coefficient is of minimal importance. The effect of an actuator failure has little effect on parasitic drag, even if an actuator fault can increase the overall drag force of the aircraft.

The scatter of empirical values in figure 2.9 can be attributed to the small variations in collected data from the wind tunnel test, a non-perfect test setup and/or an aircraft with non-perfect symmetry around the x_b - z_b -plane. If the test had been perfect in all aspects, C_Y would have been zero for all values of α as $\beta = 0$. This is different from what is observed in figure 2.9, but the empirical results still correspond well to the simulated values.

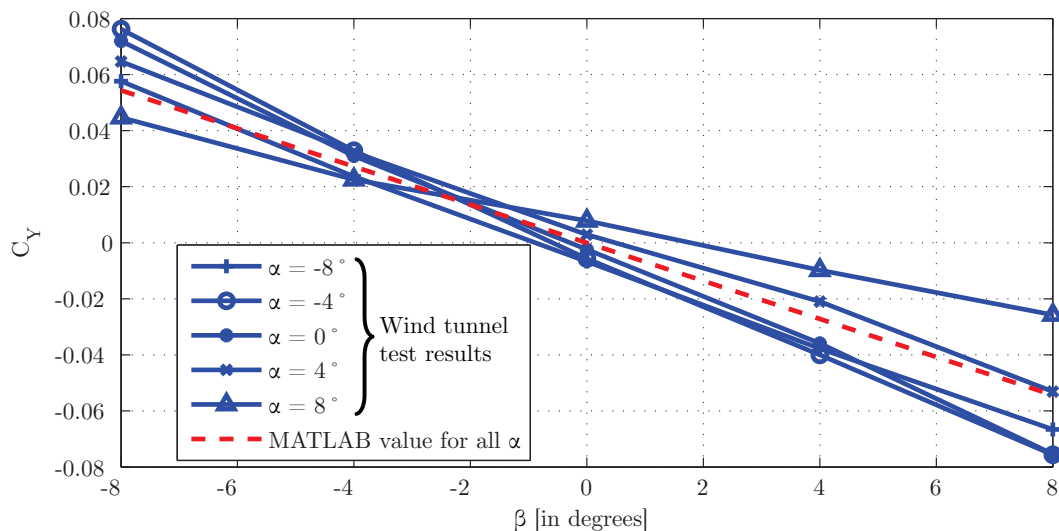


Figure 2.9: The effect of β on the aerodynamic coefficient C_Y .

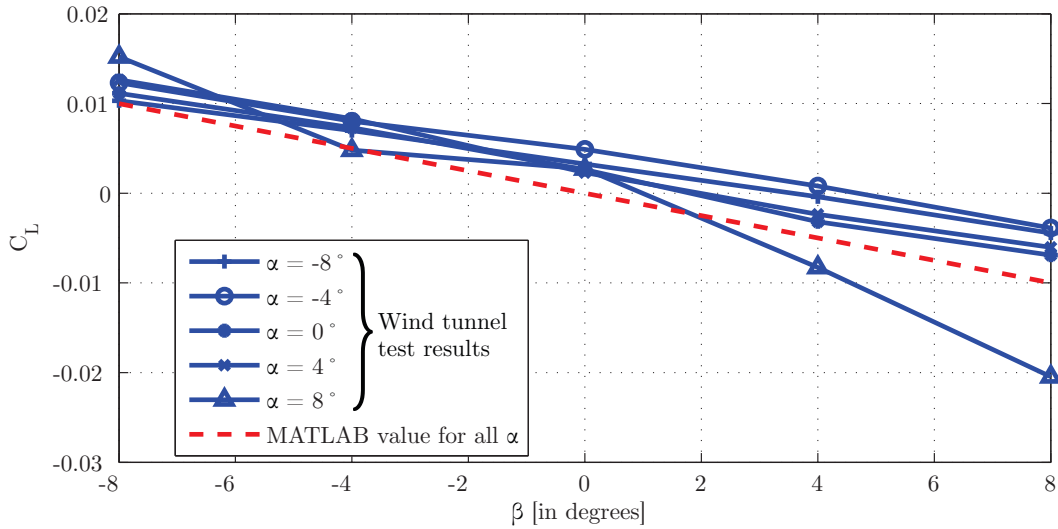


Figure 2.10: The effect of β on the aerodynamic coefficient C_L .

In figure 2.10 the effects of a non-perfect wind tunnel are evident in the non-zero value of C_L at $\beta = 0$. The results are still satisfactory as the slope of the simulation and empirical values are very similar.

Pitching moment and angle of attack are both defined positive as the nose of the aircraft pitches up. The negative slope of figure 2.11 therefore indicates the stabilising effect that the pitching moment has on α . The slope of the empirical data in figure 2.11 matches well with the simulated values.

Yawing moment is defined as a moment that tends to rotate the aircraft in a clockwise manner (looked at from above), whereas β is defined positive if the aircraft is rotated anti-clockwise in terms of the direction of airflow. The positive slope of figure 2.12 therefore indicates the stabilising effect that the yawing moment has on β . The data in figure 2.12

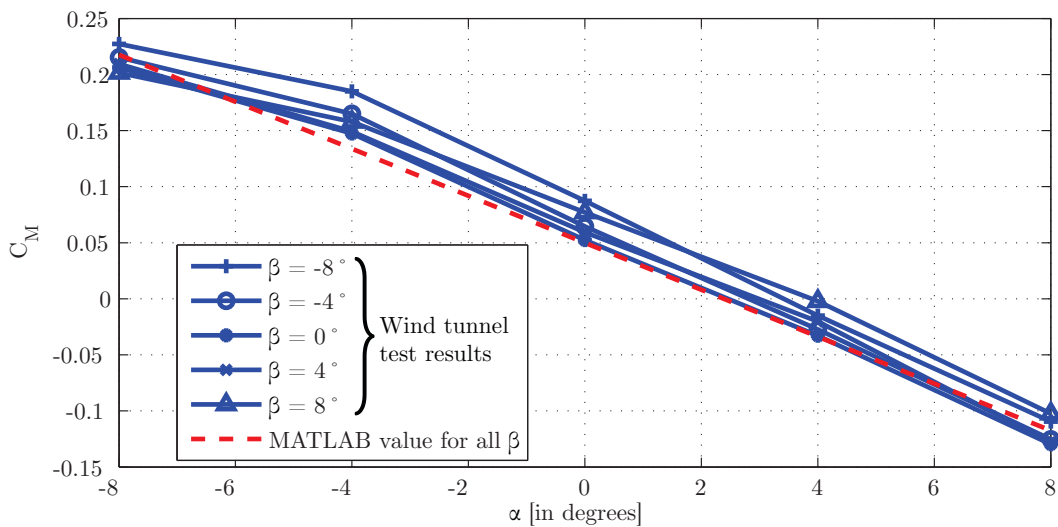


Figure 2.11: The effect of α on the aerodynamic coefficient C_M .

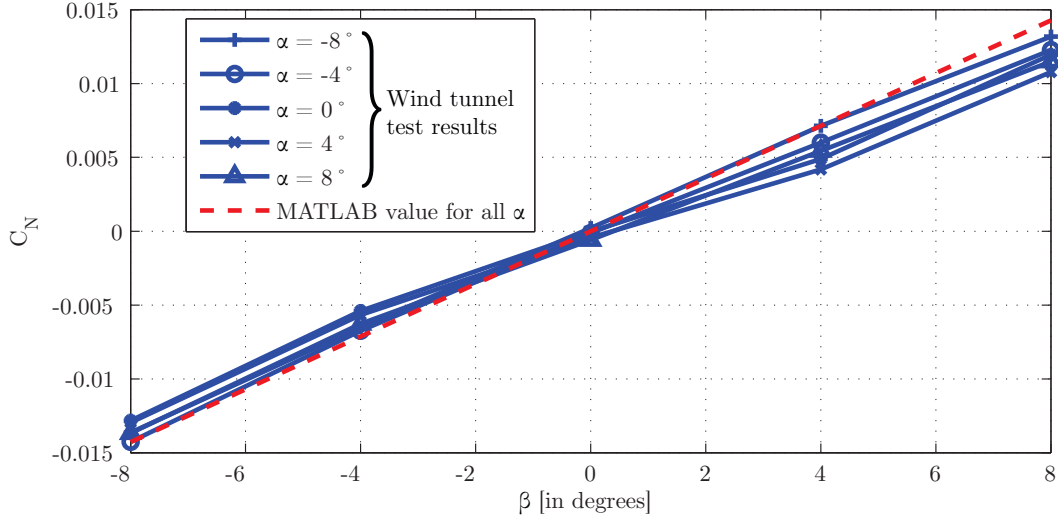


Figure 2.12: The effect of β on the aerodynamic coefficient C_N .

corresponds well with the simulated values.

2.10 Final Set of Non-Linear Differential Equations

This chapter thus far was concerned with establishing the required non-linear equations of motion and accompanying conventions and notations for the dynamics of the Meraka Modular UAV. The resulting equations are rewritten in terms of the rate of change of the twelve states of the system.

$$\dot{U} = \frac{X}{m} + VR - WQ \quad (2.10.1)$$

$$\dot{V} = \frac{Y}{m} - UR + WP \quad (2.10.2)$$

$$\dot{W} = \frac{Z}{m} + UQ - VP \quad (2.10.3)$$

$$\dot{P} = \frac{1}{I_{xx}} (L - QR(I_{zz} - I_{yy})) \quad (2.10.4)$$

$$\dot{Q} = \frac{1}{I_{yy}} (M - PR(I_{xx} - I_{zz})) \quad (2.10.5)$$

$$\dot{R} = \frac{1}{I_{zz}} (N - PQ(I_{yy} - I_{xx})) \quad (2.10.6)$$

$$\dot{\Phi} = P + Q(s_{\Phi}t_{\Theta}) + R(s_{\Phi}t_{\Theta}) \quad (2.10.7)$$

$$\dot{\Theta} = Q(c_{\Theta}) - R(s_{\Phi}) \quad (2.10.8)$$

$$\dot{\Psi} = Q(s_{\Phi}e_{\Theta}) + R(c_{\Phi}e_{\Theta}) \quad (2.10.9)$$

$$\dot{N} = U(c_{\Psi}c_{\Theta}) + V(c_{\Psi}s_{\Theta}s_{\Phi} - s_{\Psi}c_{\Phi}) + W(c_{\Psi}s_{\Theta}c_{\Phi} + s_{\Psi}s_{\Phi}) \quad (2.10.10)$$

$$\dot{E} = U(s_{\Psi}c_{\Theta}) + V(s_{\Psi}s_{\Theta}s_{\Phi} + c_{\Psi}c_{\Phi}) + W(s_{\Psi}s_{\Theta}c_{\Phi} - c_{\Psi}s_{\Phi}) \quad (2.10.11)$$

$$\dot{D} = -U(s_{\Theta}) + V(c_{\Theta}s_{\Phi}) + W(c_{\Theta}c_{\Phi}) \quad (2.10.12)$$

where

$$s_x = \sin(x) \quad (2.10.13)$$

$$c_x = \cos(x) \quad (2.10.14)$$

$$t_x = \tan(x) \quad (2.10.15)$$

$$e_x = \sec(x) \quad (2.10.16)$$

Note that the velocity and angular rate states are described in the body reference frame, while the position and attitude states are described in the inertial reference frame. The linearisation and decoupling of the dynamics will be dealt with in the next section.

2.11 Linearising the Mathematical Model

The two FDI methods developed in this research required a set of linear differential or difference equations. However, the mathematical model developed in this chapter thus far is non-linear. Therefore the system has to be linearised around a working point.

The mathematical model derived in this chapter shows that six simultaneous nonlinear equations (equations 2.5.12 to 2.5.17), together with equations 2.3.5 and 2.3.8, describe the forces and moments that influence the motion of a rigid aircraft. These equations are written in terms of the twelve state derivatives to obtain equations 2.10.1 to 2.10.12. When linearising these state differential equations, 2.10.9 to 2.10.12 are omitted, because the states Ψ , N , E and D do not recouple back into the dynamics of the aircraft, as can be seen by their absence in equations 2.10.1 to 2.10.8. The state and input vectors are chosen from these equations as

$$\mathbf{x} = [U \ V \ W \ P \ Q \ R \ \Phi \ \Theta]^T \quad (2.11.1)$$

$$\mathbf{u} = \begin{bmatrix} \delta \\ T \end{bmatrix} \quad (2.11.2)$$

and the resulting differential equations are

$$\dot{U} = \frac{X}{m} + VR - WQ \quad (2.11.3)$$

$$\dot{V} = \frac{Y}{m} - UR + WP \quad (2.11.4)$$

$$\dot{W} = \frac{Z}{m} + UQ - VP \quad (2.11.5)$$

$$\dot{P} = \frac{1}{I_{xx}} (L - QR(I_{zz} - I_{yy})) \quad (2.11.6)$$

$$\dot{Q} = \frac{1}{I_{yy}} (M - PR(I_{xx} - I_{zz})) \quad (2.11.7)$$

$$\dot{R} = \frac{1}{I_{zz}} (N - PQ(I_{yy} - I_{xx})) \quad (2.11.8)$$

$$\dot{\Phi} = P + Q \sin(\Phi) \tan(\Theta) + R \sin(\Phi) \tan(\Theta) \quad (2.11.9)$$

$$\dot{\Theta} = Q \cos(\Theta) - R \sin(\Theta) \quad (2.11.10)$$

which can be written in compact form as

$$\dot{\mathbf{x}} = \mathbf{f}(\mathbf{x}, \mathbf{u}) \quad (2.11.11)$$

where

$$\mathbf{x} = [U \ V \ W \ P \ Q \ R \ \Phi \ \Theta]^T \quad (2.11.12)$$

$$\mathbf{u} = \begin{bmatrix} \delta \\ T \end{bmatrix} \quad (2.11.13)$$

With reference to equations 2.11.3 to 2.11.10, the aircraft can be described as a system with smooth non-linearities that is continuously differentiable. For such a model, a linear model can be computed around a small localised equilibrium working-point that is valid for small perturbations. The aim will be to rewrite the non-linear set of equations (equation 2.11.11) in the linear form:

$$\dot{\mathbf{x}} = \mathbf{A}\mathbf{x} + \mathbf{B}\mathbf{u} \quad (2.11.14)$$

For small signal linearisation the states and inputs are expanded as the sum of their working point values and the perturbation around the working point as

$$\mathbf{x} = \bar{\mathbf{x}} + \Delta\mathbf{x} \quad (2.11.15)$$

$$\mathbf{u} = \bar{\mathbf{u}} + \Delta\mathbf{u} \quad (2.11.16)$$

where the state perturbations will be written as lower case letters and Greek symbols to clarify the difference between them and the absolute states:

$$\Delta\mathbf{x} = [u \ v \ w \ p \ q \ r \ \phi \ \theta]^T \quad (2.11.17)$$

$$\Delta\mathbf{u} = \begin{bmatrix} \Delta\delta \\ \Delta T \end{bmatrix} \quad (2.11.18)$$

When equations 2.11.15 and 2.11.16 are substituted into equation 2.11.11, the expansion yields an expanding Taylor series

$$\dot{\bar{\mathbf{x}}} + \Delta\dot{\mathbf{x}} = \mathbf{f}(\bar{\mathbf{x}} + \Delta\mathbf{x}, \bar{\mathbf{u}} + \Delta\mathbf{u}) \quad (2.11.19)$$

$$= \mathbf{f}(\bar{\mathbf{x}}, \bar{\mathbf{u}}) + \left. \frac{\partial \mathbf{f}}{\partial \mathbf{x}} \right|_{\text{wp}} \Delta\mathbf{x} + \left. \frac{\partial \mathbf{f}}{\partial \mathbf{u}} \right|_{\text{wp}} \Delta\mathbf{u} + \text{higher order terms} \quad (2.11.20)$$

$$= \mathbf{f}(\bar{\mathbf{x}}, \bar{\mathbf{u}}) + \mathbf{A}_{\text{wp}} \Delta\mathbf{x} + \mathbf{B}_{\text{wp}} \Delta\mathbf{u} + \text{higher order terms} \quad (2.11.21)$$

where the subscript “wp” means the evaluation at the working point and

$$\mathbf{A}_{\text{wp}} = \left. \frac{\partial \mathbf{f}}{\partial \mathbf{x}} \right|_{\text{wp}} \quad (2.11.22)$$

$$\mathbf{B}_{\text{wp}} = \left. \frac{\partial \mathbf{f}}{\partial \mathbf{u}} \right|_{\text{wp}} \quad (2.11.23)$$

can be thought of the best linear fit to the nonlinear function $\dot{\mathbf{x}} = \mathbf{f}(\mathbf{x}, \mathbf{u}) \approx \mathbf{A}\mathbf{x} + \mathbf{B}\mathbf{u}$.

Ignoring the higher order terms that are negligible, while noting $\dot{\bar{\mathbf{x}}} = \mathbf{f}(\bar{\mathbf{x}}, \bar{\mathbf{u}}) = 0$, the dynamics of the system can be described by

$$\Delta \dot{\mathbf{x}} = \mathbf{A}_{\text{wp}} \Delta \mathbf{x} + \mathbf{B}_{\text{wp}} \Delta \mathbf{u} \quad (2.11.24)$$

which is a continuous state space approximation of a set of nonlinear equations around a specified working point.

The linearisation problem now becomes one of finding the partial derivatives that constitute the elements in \mathbf{A}_{wp} and \mathbf{B}_{wp} . Before this process is continued some simplifying assumptions are made specifically for actuator FDI.

From appendix A and section 2.6, note that the actuators have no apparent effect on three of the eight states defined in equations 2.11.3 to 2.11.10. The states that are not affected by the actuators are velocity, yaw and pitch. The FDI will therefore only be interested in the differential equations (and therefore the partial derivatives) relating the actuator inputs to the remaining five states. These states are p, q, r, w and v . This reduced state vector greatly simplifies the FDI and therefore reduces the processing power required on-board without losing significant performance. The rest of the states that are not included can still be accurately estimated on-board with conventional estimators. The new reduced state vector becomes

$$\Delta \mathbf{x} = \begin{bmatrix} p & q & r & w & v \end{bmatrix}^T \quad (2.11.25)$$

All the resulting information for calculating the partial derivatives are contained in the equations for aerodynamic forces and moments (equations 2.6.9 to 2.6.16). The first problem encountered is that the two states, w and v , are not explicitly used in the aerodynamic equations. This can be rectified by using equation 2.3.10 and noting that α and β are measurable. Then according to the small angle assumption made in section 2.4

$$\alpha = \arctan\left(\frac{W}{U}\right) \quad (2.11.26)$$

$$= \arctan\left(\frac{W}{|\mathbf{V}|_{\text{wp}} \cos(\beta) \cos(\alpha)}\right) \quad (2.11.27)$$

$$\approx \frac{W}{|\mathbf{V}|_{\text{wp}}} \quad (2.11.28)$$

$$\beta = \arctan\left(\frac{V}{U} \cos(\alpha)\right) \quad (2.11.29)$$

$$= \arctan\left(\frac{V}{|\mathbf{V}|_{\text{wp}} \cos(\beta) \cos(\alpha)} \cos(\alpha)\right) \quad (2.11.30)$$

$$\approx \frac{V}{|\mathbf{V}|_{\text{wp}}} \quad (2.11.31)$$

The state vector is then changed by substituting α and β for w and v respectively, resulting in a new state vector:

$$\Delta \mathbf{x} = \begin{bmatrix} p & q & r & \alpha & \beta \end{bmatrix}^T \quad (2.11.32)$$

Using equations 2.11.22 and 2.11.23 as a guide, the matrices \mathbf{A}_{wp} and \mathbf{B}_{wp} are expanded into the matrices contained in appendix B.1, equation B.1.1. The calculations of the partial

derivatives in equation B.1.1 are found in appendix B.2 and the linearised state matrices can be found in appendix B.3.

2.12 Discretising the State Space Representation

Both FDI methods developed in this research are discrete recursive processes and will be implemented on digital computers. The continuous state space representations of equation B.3.1 must therefore be discretised into the form

$$\mathbf{x}_{k+1} = \mathbf{F}\mathbf{x}_k + \mathbf{G}\mathbf{u}_k \quad (2.12.1)$$

$$\mathbf{y}_k = \mathbf{H}\mathbf{x}_k \quad (2.12.2)$$

where \mathbf{y}_k is the measurement vector, \mathbf{H} is the measurement matrix and the subscript k denotes the time step.

Assuming a zero-order hold digital process, the discrete state space matrices become [32]

$$\mathbf{F} = e^{\mathbf{A}T} \quad (2.12.3)$$

$$\mathbf{G} = \left(\int_0^T e^{\mathbf{A}\eta} d\eta \right) \mathbf{B} \quad (2.12.4)$$

$$\mathbf{H} = \mathbf{C} \quad (2.12.5)$$

where \mathbf{C} is the continuous measurement matrix and T is the time step length.

The extended Kalman filter must be able to linearise and discretise the state space matrices at each time step. The discretisation proposed above may be intractable due to the heavy matrix exponential and integral operations. A discrete approximation for the state space representation can be found by expanding equation 2.12.3 [32]:

$$\mathbf{F} = e^{\mathbf{A}T} \quad (2.12.6)$$

$$= \mathbf{I} + \mathbf{A}T + \frac{\mathbf{A}^2 T^2}{2!} + \frac{\mathbf{A}^3 T^3}{3!} + \dots \quad (2.12.7)$$

$$\approx \mathbf{I} + \mathbf{A}T \quad (2.12.8)$$

The higher order terms can be ignored as they become significantly smaller as the power of T increases. This is due to the small time step used in the digital computer.

Using the same procedure, equation 2.12.4 can be approximated as

$$\mathbf{G} \approx T\mathbf{B} \quad (2.12.9)$$

The required mathematical model and linearised matrices are ready to be utilised in the design and development of the two FDI processes.

Chapter 3

First Fault Detection and Isolation Method: A Bank of Kalman Filters

In this chapter a classic Multiple Model Adaptive Estimation (MMAE) [2] method for FDI using a bank of Kalman filters will be investigated. Some limitations of this method will be highlighted and a non-linear Extended Multiple Model Adaptive Estimation (EMMAE) method will be developed whereafter the advantages and disadvantages of the latter are discussed.

In this method the measurement residual from each Kalman filter is used in combination with its own residual covariance matrix to detect and isolate the fault. Each fault scenario estimator (Kalman filter) is also modified so that it can estimate the particular actuator deflection.

3.1 The Fault Detection and Isolation Architecture

The bank of Kalman filters is an estimator based method for FDI, which requires several different models of the same aircraft system. The difference between the models is that each one describes a different fault (or no-fault) scenario. The estimator bank is adaptive in the sense that the final estimated state is calculated based on a weighting of the estimates that describe each scenario. The dynamics of the bank of Kalman filters are therefore dependent on the fault scenario in which the aircraft operates. The aircraft states can therefore still be accurately estimated when a fault occurs.

The MMAE architecture is depicted in figure 3.1. Here each filter's residual covariance matrix, as well as its measurement residual, is sent to a probability computation that determines each scenario's probability. This probability is used as a weighting for the state estimate from each filter to produce the best total state estimate. The probabilities are also used in the failure decision-making process that will classify the current fault scenario.

From the eight actuators nine filters can be implemented (one filter for each fault and one for the no-fault scenario) to achieve actuator fault detection. However, the flaps and ailerons are physically similar (see figure 2.4) and therefore mathematically similar (see appendix

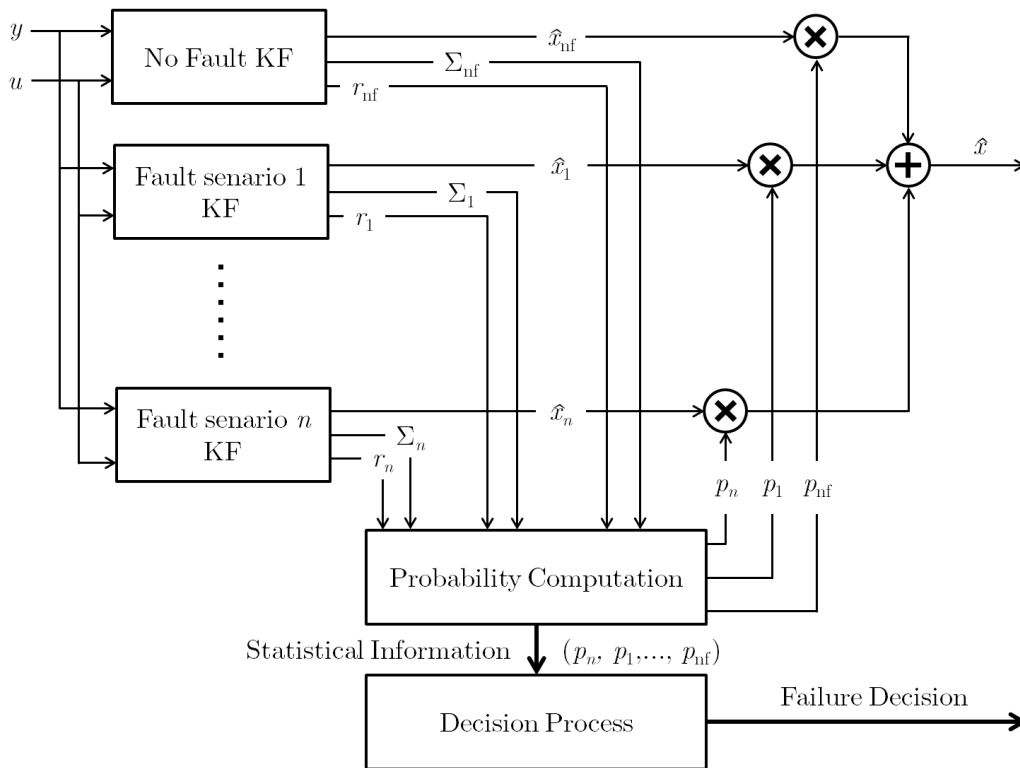


Figure 3.1: Architecture for the bank of Kalman filters.

A). The flaps are also used as passive control surfaces only at landing and take-off. The diagnosis of flap faults will therefore be ignored in this research. The control re-allocation process in [3] however can use them as independent actuators, once a fault has occurred.

3.2 Designing the Kalman Filters

The Kalman filter is a recursive process in which information from the sensors and information obtained from the mathematical propagation of the dynamics are merged. This is done in an optimal way only if specific assumptions hold [33]. Some of these assumptions are that the process is linear, the process and measurement noise must be white, normally distributed, and the distribution parameters of the process and measurement noise must be known. These assumptions do not strictly hold in a typical aircraft system, but are reasonably acceptable in the engineering practice [20].

The state of the aircraft for each scenario will be predicted by the bank of Kalman filters, where each filter is designed to resemble a particular fault (or no-fault) scenario. The philosophy of this technique is that the filter that most closely resembles the true scenario will have the smallest residuals and therefore be most likely to be the true scenario.

The first step of designing the Kalman filters is to obtain a mathematical model and linearise it around a pre-defined working point. The linearising process was done previously in section

2.11. For the bank of linear Kalman filters the trim condition will be chosen as the working point. For the extended Kalman filters the state and input matrix will be linearised at each time step. The second step is to modify each Kalman filter to resemble the fault scenario for which it is responsible.

3.2.1 The Kalman Filter Equations

The development of the bank of Kalman filters will start by designing a bank of linear Kalman filters. The linear Kalman filters will be constructed around the trim conditions of the Meraka Modular UAV.

To determine the trim values the formulas written below (equations 3.2.1 and 3.2.2) can be used bearing in mind the assumptions that the trim angle of attack is small (the fifth assumption in section 2.4) and that the lift force is an order of magnitude greater than the drag force.

The trim condition is calculated as the solution to the equilibrium problem given by the desire of straight and level flight at a specific nominal velocity. The trim velocity is chosen at 22 m/s [3]. The problem assumes a zero value for yaw, roll, sideslip, lateral velocity and all angular rates. The solution then provides a value for the thrust force and elevator deflections as well as the trim angle of attack and pitch angle. The formulas to determine trim with these assumptions are [29]

$$\begin{bmatrix} \alpha \\ \delta_{Er} \end{bmatrix}_T = \begin{bmatrix} C_{L\alpha} & (C_{L\delta_{Er}} + C_{L\delta_{El}}) \\ C_{m\alpha} & (C_{m\delta_{Er}} + C_{m\delta_{El}}) \end{bmatrix}^{-1} \begin{bmatrix} \frac{mg}{q_T S} - C_{L0} \\ -C_{m0} \end{bmatrix} \quad (3.2.1)$$

$$T_T = q_T S C_{D_T} \cos \alpha_T - q_T S C_{L_T} \sin \alpha_T + mg \sin \alpha_T \quad (3.2.2)$$

where the subscript T denotes values evaluated at trim condition and

$$q_T = \frac{1}{2} \rho |\mathbf{V}|_T^2 \quad (3.2.3)$$

and noting that at trim conditions $\delta_{El} = \delta_{Er}$.

Each filter will have different values for the elements in their state, input, and measurement matrices. The structure of the Kalman filter however remains the same and will be described in this section. The linearised mathematical model (equation 2.12.1 and 2.12.2) will be rewritten, but with added noise terms

$$\mathbf{x}_{k+1} = \mathbf{F}\mathbf{x}_k + \mathbf{G}\mathbf{u}_k + \mathbf{w}_k \quad (3.2.4)$$

$$\mathbf{y}_k = \mathbf{H}\mathbf{x}_k + \mathbf{v}_k \quad (3.2.5)$$

where \mathbf{y}_k is the current measurement, \mathbf{w}_k is the random process affecting the system states and \mathbf{v}_k is the measurement noise from the sensors. The subscript k will resemble the k -th time step.

The Kalman filter can be described by two processes running in series: firstly a mathematical prediction step and secondly a measurement update step, if a measurement is available. The

prediction step uses equation 3.2.4 to predict the next state value and the state covariance matrix

$$\hat{\mathbf{x}}_{k|k-1} = \mathbf{F}_k \hat{\mathbf{x}}_{k-1|k-1} + \mathbf{G}_k \mathbf{u}_k \quad (3.2.6)$$

$$\mathbf{P}_{k|k-1} = \mathbf{F}_k \mathbf{P}_{k-1|k-1} \mathbf{F}_k^T + \mathbf{Q}_k \quad (3.2.7)$$

In equations 3.2.6 and 3.2.7 the first part of the subscript (e.g. the k in $\hat{\mathbf{x}}_{k|k-1}$) refers to the time step in which prediction last occurred, whereas the second part (e.g. the $k-1$ in $\mathbf{P}_{k|k-1}$) refers to the time step in which an measurement update last occurred. The state estimate covariance is predicted with the knowledge of the process noise statistical information (equation 3.2.7).

The second process is an update on the predicted estimate, if a measurement is available. The driving force in the update process is the residual, which is the difference between the measured and predicted value

$$\tilde{\mathbf{r}}_k = \mathbf{y}_k - \mathbf{H}_k \hat{\mathbf{x}}_{k|k-1} \quad (3.2.8)$$

The residual covariance is calculated with knowledge of the measurement noise statistical information:

$$\mathbf{S}_k = \mathbf{H}_k \mathbf{P}_{k|k-1} \mathbf{H}_k^T + \mathbf{R}_k \quad (3.2.9)$$

The Kalman gain is then calculated so that a statistically optimal weighting can be given to both the predicted estimate and the measurement to produce a final estimate:

$$\mathbf{K}_k = \mathbf{P}_{k|k-1} \mathbf{H}_k^T \mathbf{S}_k^{-1} \quad (3.2.10)$$

$$\hat{\mathbf{x}}_{k|k} = \hat{\mathbf{x}}_{k|k-1} + \mathbf{K}_k \tilde{\mathbf{r}}_k \quad (3.2.11)$$

The state estimate covariance is then also updated.

$$\mathbf{P}_{k|k} = (\mathbf{I} - \mathbf{K}_k \mathbf{H}_k) \mathbf{P}_{k|k-1} \quad (3.2.12)$$

3.2.2 The Kalman Filter for the No-Fault Scenario

The Kalman filter is a discrete process that requires the covariance matrices of the process and measurement noise that were determined from sensor data sheets and an analysis on the flight dynamics with a wind model affecting the external forces acting on the aircraft. See appendix C for more details on the derivation of the covariance matrices. For the no-fault case the state matrices are just the discrete linearised matrices from equation 2.12.8 and 2.12.9 evaluated at the trim condition:

$$\mathbf{F}_{nf} = \mathbf{F}_T \quad (3.2.13)$$

$$\mathbf{G}_{nf} = \mathbf{G}_T \quad (3.2.14)$$

$$\mathbf{Q}_{nf} = E\{\mathbf{w}_k \mathbf{w}_k^T\} \quad (3.2.15)$$

$$\mathbf{R}_{nf} = E\{\mathbf{v}_k \mathbf{v}_k^T\} \quad (3.2.16)$$

In the Meraka Modular UAV there are sensors that directly measure all five of the required states and therefore the measurement matrix will be an identity matrix of size 5×5 . The measurement matrix is the same as for the continuous state space system

$$\mathbf{H}_{nf} = \mathbf{I} \quad (3.2.17)$$

3.2.3 The Kalman Filters for the Fault Scenarios

There are important adjustments that must be made for each fault scenario Kalman filter. Note that after a fault has occurred, the control signal is independent of the true control surface deflection, however, the control surface still has an effect on the dynamics of the system. The actuator deflection therefore becomes one of the system states and must be estimated. With this adjustment the required actuator information for the control re-allocation is also readily available when needed.

The new augmented state vector includes the estimated actuator deflection

$$\mathbf{x}_i = \begin{bmatrix} \mathbf{x} \\ \hat{\delta}_i \end{bmatrix} \quad (3.2.18)$$

where i represents the i^{th} Kalman filter for the i^{th} fault scenario.

The dynamics of the i^{th} actuator are described by its corresponding column in the no-fault input matrix, \mathbf{G}_{nf} . To augment the fault state space matrices, the i^{th} column is nulled in the input matrix and added to the state matrix. It is also assumed that the states of the system have little to no effect on the deflection of the actuator once a fault has occurred. The last row in the state matrix is therefore nulled except for the element corresponding to the actuator deflection itself. This will be set as unity, since the deflection is assumed to have no increasing or decreasing effect on the future state of the deflection.

$$\mathbf{F}_i = \begin{bmatrix} \mathbf{F}_{nf} & \mathbf{G}_{nf}^{(i)} \\ \mathbf{0} & 1 \end{bmatrix} \quad (3.2.19)$$

$$\mathbf{G}_i = \begin{bmatrix} \mathbf{G}_{nf}^{(0,i)} \\ \mathbf{0} \end{bmatrix} \quad (3.2.20)$$

where $\mathbf{G}_{nf}^{(i)}$ represents the i^{th} column of \mathbf{G}_{nf} and $\mathbf{G}_{nf}^{(0,i)}$ corresponds to replacing the i^{th} column of \mathbf{G}_{nf} with zeros.

There are no sensors that directly measure the deflection of the control surfaces, which is one of the objectives of this research. The additional column corresponding to the actuator deflection is therefore nulled and the measurement matrix becomes

$$\mathbf{H}_i = \begin{bmatrix} \mathbf{H}_{nf} & \mathbf{0} \end{bmatrix} \quad (3.2.21)$$

$$= \begin{bmatrix} \mathbf{I} & \mathbf{0} \end{bmatrix} \quad (3.2.22)$$

The state equations for the i^{th} fault scenario Kalman filters becomes

$$\mathbf{x}_i(k+1) = \mathbf{F}_i \mathbf{x}_i(k) + \mathbf{G}_i \mathbf{u}(k) + \mathbf{w}_i(k) \quad (3.2.23)$$

$$\mathbf{y}_i(k) = \mathbf{H}_i \mathbf{x}_i(k) + \mathbf{v}_i(k) \quad (3.2.24)$$

where the covariance matrices

$$\mathbf{Q}_i(k) = E\{\mathbf{w}_i(k)\mathbf{w}_i^T(k)\} \quad (3.2.25)$$

$$\mathbf{R}_i(k) = E\{\mathbf{v}_i(k)\mathbf{v}_i^T(k)\} \quad (3.2.26)$$

The covariance matrices for the process and measurement noise in the case of the fault scenarios must take the effect of the actuator fault into account. The derivation of these covariance matrices are shown in appendix C.

The same Kalman filter process is followed as in section 3.2.1 to estimate the states of the fault scenarios. It is interesting to note that while the process is running on-board the aircraft, the fault scenario filters still estimate the actuator deflections so that they correspond with what is observed through the measurements. This fact translates into two different observations.

The first is that when a fault occurs with enough actuator excitation, the residuals of the incorrect Kalman filters will be larger than the correct one. However, when there is no actuator excitation, the filters should have small, similar residuals that makes discerning between different fault scenarios more difficult.

The second is that when a fault occurs, all the fault filters will still estimate their particular actuator deflection so that the state estimate resembles what is observed through the sensors. This creates interesting responses from filters whose fault is not actually active. This does not affect the performance of the FDI in providing accurate information to the re-allocation process as only the information of the real faulty sensor is sent to it. This phenomenon is clearly shown and discussed in the results later in the chapter.

3.2.4 Replacing the Linear Kalman Filters with Extended Kalman Filters

The aircraft is a naturally non-linear system as can be seen in equations 2.10.1 to 2.10.12. The inability of the linear Kalman filters to deal with the non-linearities can be bypassed by using extended Kalman filters (EKF) instead. A separate module with a bank of extended Kalman filters will be developed, which will run parallel to the bank of linear Kalman filters. This allows us to compare the advantages and disadvantages that an extended Kalman filter has over the use of linear Kalman filters.

One of the differences between the extended Kalman filter and the linear Kalman filter is that the system matrices, covariances and Kalman gains change with time. These changes are the result of the linearising process that occurs at every time step. The prediction step is also substituted with the non-linear solution of equation 2.11.11 with the previous state estimate as the initial condition

$$\hat{\mathbf{x}}_{k|k-1} = \hat{\mathbf{x}}_{k-1|k-1} + T\mathbf{f}(\hat{\mathbf{x}}_{k-1|k-1}, \mathbf{u}_{k-1}) \quad (3.2.27)$$

where T is the time step length.

At each time step the dynamic pressure, the airflow velocity as well as the angular rates are re-evaluated and used in the linearising process to alter the state and input matrices. \mathbf{A}_k

and \mathbf{B}_k are then used in the EKF to recalculate the covariance matrices and the Kalman gains.

The same decision process will be used on both the bank of extended and linear Kalman filter residuals and residual covariance matrices.

3.3 Decision Process

The decision process is concerned with making an informed automated decision over whether or not a fault has occurred. This is not truly the probability that a fault has occurred but rather a likelihood in the form of a probability. The first step in the decision process is to find a quantitative way to categorise the fault state in which the system is operating. This will be done by determining the probability that the system is in a specific fault state. The second part is to employ this information to make a final fault decision.

3.3.1 Gaussian Bayes Classifier

To calculate the probability of the faults, a Gaussian Bayes Classifier (GBC) will be used. The use of a GBC is ideal because the bank of Kalman filters provides all the statistical information (the residuals $\tilde{\mathbf{r}}_k$ and the residual covariance matrix \mathbf{S}_k) required to construct a likelihood function for all the parameters in all the fault scenarios. The GBC then uses the likelihood functions to create probabilities of the fault scenarios.

The aim of the GBC is to determine a likelihood of a specific class variable, C , given a number of feature variables or evidence $\mathbf{F} = [F_1, F_2, \dots, F_n]$. In this research the class variable will be the type of fault, denoted by θ , and the evidence will be the sequence of last observed sensor values $\mathbf{Y}(k) = [\mathbf{y}(k), \mathbf{y}(k-1), \mathbf{y}(k-2), \dots, \mathbf{y}(0)]^T$.

$$p(C|\mathbf{F}) = p(\theta|\mathbf{Y}(k)) \quad (3.3.1)$$

According to Bayes' theorem,

$$p(\theta|\mathbf{Y}(k)) = \frac{p(\theta)p(\mathbf{Y}(k)|\theta)}{p(\mathbf{Y}(k))} \quad (3.3.2)$$

We denote the i^{th} fault as θ_i and the probability of the i^{th} fault being active as $p_i(k)$ at time step k . More formally stated

$$p_i(k) = p(\theta = \theta_i|\mathbf{Y}(k)) \quad (3.3.3)$$

$$= \frac{p(\mathbf{Y}(k)|\theta = \theta_i)p(\theta = \theta_i)}{p(\mathbf{Y}(k))} \quad (3.3.4)$$

A reasonable assumption is that the fault scenarios can happen independently from one another. The probability $p(\mathbf{Y}(k))$, found in the denominator of equation 3.3.4, can therefore be expanded with the use of the chain rule as

$$p(\mathbf{Y}(k)) = p(\mathbf{Y}(k)|\theta = \theta_1)p(\theta = \theta_1) + \dots + p(\mathbf{Y}(k)|\theta = \theta_N)p(\theta = \theta_N) \quad (3.3.5)$$

$$= \sum_{j=1}^N p(\mathbf{Y}(k)|\theta = \theta_j)p(\theta = \theta_j) \quad (3.3.6)$$

where N is the number of fault scenarios, including the no-fault case. Equation 3.3.4 then becomes

$$p_i(k) = \frac{p(\mathbf{Y}(k)|\theta = \theta_i)p(\theta = \theta_i)}{\sum_{j=1}^N p(\mathbf{Y}(k)|\theta = \theta_j)p(\theta = \theta_j)} \quad (3.3.7)$$

In its current form, all the covariances and values for the last sequence of measurements must be known to determine the probability. To transform equation 3.3.7 into a recursive formula and save on computational power, the sequence of measurements is re-written as $[\mathbf{y}(k), \mathbf{Y}(k-1)]^T$. With the use of the chain rule again, the probability of $\mathbf{Y}(k)$ given a specific fault scenario becomes

$$p(\mathbf{Y}(k)|\theta = \theta_i) = p([\mathbf{y}(k), \mathbf{Y}(k-1)]^T|\theta = \theta_i) \quad (3.3.8)$$

$$= p(\mathbf{y}(k)|\mathbf{Y}(k-1), \theta = \theta_i)p(\mathbf{Y}(k-1)|\theta = \theta_i) \quad (3.3.9)$$

$$= p(\mathbf{y}(k)|\theta = \theta_i, \mathbf{Y}(k-1))p(\theta = \theta_i|\mathbf{Y}(k-1)) \quad (3.3.10)$$

$$= p(\mathbf{y}(k)|\theta = \theta_i, \mathbf{Y}(k-1))p_i(k-1) \quad (3.3.11)$$

Substituting equation 3.3.11 into equation 3.3.7 gives [2]

$$p_i(k) = \frac{p(\mathbf{y}(k)|\theta = \theta_i, \mathbf{Y}(k-1))p_i(k-1)\cancel{p(\theta = \theta_i)}}{\sum_{j=1}^N p(\mathbf{y}(k)|\theta = \theta_j, \mathbf{Y}(k-1))p_j(k-1)\cancel{p(\theta = \theta_j)}} \quad (3.3.12)$$

$$= \frac{p(\mathbf{y}_i(k)|\theta = \theta_i, \mathbf{Y}(k-1))p_i(k-1)}{\sum_{j=1}^N p(\mathbf{y}_j(k)|\theta = \theta_j, \mathbf{Y}(k-1))p_j(k-1)} \quad (3.3.13)$$

The probability that any of the fault scenarios are active, without any other prior knowledge, is assumed to be equal. Therefore $p(\theta = \theta_i) = \frac{1}{N}$ for $i = 1, 2, \dots, N$ and the terms $p(\theta = \theta_i)$ and $p(\theta = \theta_j)$ cancel each other out in equation 3.3.12. Note that the denominator of equation 3.3.13 is the sum of the numerators of all the fault probability computations, so that all the fault probabilities add up to one. Also note that the probability is determined as the product of a current probability and the previous probability. It is therefore important to prevent the probability from reaching zero and so becoming locked at zero.

The problem in equation 3.3.13 is finding an explicit formula for $p(\mathbf{y}(k)|\theta = \theta_i, \mathbf{Y}(k-1))$. In the flight simulation and flight tests a set of observed sensor values $\mathbf{y}(k)$ are given. The likelihood that a specific fault has occurred, given the set of observations in the flight test, must be determined. Probability and likelihood are however mathematically similar and formally stated, “[t]he likelihood of a specific hypothesis (or class variable), given a set of observed features, is proportional the probability of the data outcomes given the specific hypothesis being true” [34]

$$\mathcal{L}(C|F) \propto p(F|C) \quad (3.3.14)$$

where C is the class variable and F is the observed features. The conditional probability in equation 3.3.11 can therefore be written as a likelihood

$$p(\mathbf{y}_i(k)|\theta = \theta_i, \mathbf{Y}(k-1)) = C_1 \mathcal{L}(\theta = \theta_i, \mathbf{Y}(k-1)|\mathbf{y}_i(k)) \quad (3.3.15)$$

where C_1 is a constant of proportionality. Equation 3.3.13 can therefore be rewritten as a likelihood ratio test, which translates into a probability

$$p_i(k) = \frac{C_1 \mathcal{L}(\theta = \theta_i, \mathbf{Y}(k-1) | \mathbf{y}(k)) p_i(k-1)}{\sum_{j=1}^N C_1 \mathcal{L}(\theta = \theta_j, \mathbf{Y}(k-1) | \mathbf{y}(k)) p_j(k-1)} \quad (3.3.16)$$

The sensor outputs have continuous values (note, not time continuous but value continuous) and the normal distribution function described by the residual covariance matrix returns a probability density. According to [34], the likelihood function of a hypothesis, given a continuous parameter, is proportional to the probability density function of the parameter, given a specific hypothesis

$$\mathcal{L}(\theta = \theta_i, \mathbf{Y}(k-1) | \mathbf{y}_i(k)) = C_2 f(\mathbf{y}_i(k) | \theta = \theta_i, \mathbf{Y}(k-1)) \quad (3.3.17)$$

The actual value of a likelihood function bears no meaning, but is used to compare it to the likelihood of belonging to a specific density distribution. It is now necessary to derive the probability density $f(\mathbf{y}(k) | \theta = \theta_i, \mathbf{Y}(k-1))$ and it is chosen to be a normal distributed density function as all the required information is available from the Kalman filters

$$f(\mathbf{y}(k) | \theta = \theta_i, \mathbf{Y}(k-1)) = \frac{1}{(2\pi)^{\frac{m}{2}} |\boldsymbol{\Sigma}|^{\frac{1}{2}}} \exp\left(-\frac{1}{2}(\mathbf{y}(k) - \boldsymbol{\mu}(k))^T \boldsymbol{\Sigma}^{-1}(\mathbf{y}(k) - \boldsymbol{\mu}(k))\right) \quad (3.3.18)$$

where $\boldsymbol{\Sigma}$ is the covariance matrix and $\boldsymbol{\mu}(k)$ is the mean value of the measurement at time step k . m is the dimension of the measurement (in this case $m=5$). If the mean value in equation 3.3.18 is substituted with the expected value of the measurement, $\hat{\mathbf{y}}(k) = \mathbf{H}\hat{\mathbf{x}}(k)$, the term $(\mathbf{y}(k) - \boldsymbol{\mu}(k))$ conveniently becomes the Kalman filter residual

$$(\mathbf{y}(k) - \boldsymbol{\mu}(k)) = (\mathbf{y}(k) - \mathbf{H}\hat{\mathbf{x}}(k)) \quad (3.3.19)$$

$$= \tilde{\mathbf{r}}(k) \quad (3.3.20)$$

and the covariance chosen as the residual covariance matrix $\boldsymbol{\Sigma} = \mathbf{S}_k$. Equation 3.3.18 can now be written in compact form as

$$f(\mathbf{y} = \mathbf{y}_i(k) | \theta = \theta_i, \mathbf{Y}(k-1)) = \lambda_i(k) e^{-\frac{\tilde{\mathbf{r}}_i(k)^T \mathbf{S}_k \tilde{\mathbf{r}}_i(k)}{2}} \quad (3.3.21)$$

where

$$\lambda_i(k) = \frac{1}{(2\pi)^{\frac{m}{2}} |\mathbf{S}_k|^{\frac{1}{2}}} \quad (3.3.22)$$

Equation 3.3.13 is finally written as

$$p_i(k) = \frac{C_1 e_2 f(\mathbf{y} = \mathbf{y}_i(k) | \theta = \theta_i, \mathbf{Y}(k-1)) p_i(k-1)}{\sum_{j=1}^N C_1 e_2 f(\mathbf{y} = \mathbf{y}_j(k) | \theta = \theta_j, \mathbf{Y}(k-1)) p_j(k-1)} \quad (3.3.23)$$

$$p_i(k) = \frac{f(\mathbf{y} = \mathbf{y}_i(k) | \theta = \theta_i, \mathbf{Y}(k-1)) p_i(k-1)}{\sum_{j=1}^N f(\mathbf{y} = \mathbf{y}_j(k) | \theta = \theta_j, \mathbf{Y}(k-1)) p_j(k-1)} \quad (3.3.24)$$

where $f(\mathbf{y} = \mathbf{y}_i(k) | \theta = \theta_i, \mathbf{Y}(k-1))$ is given by equation 3.3.21.

A simplified representation of equation 3.3.24 is given in figure 3.2. In the figure three

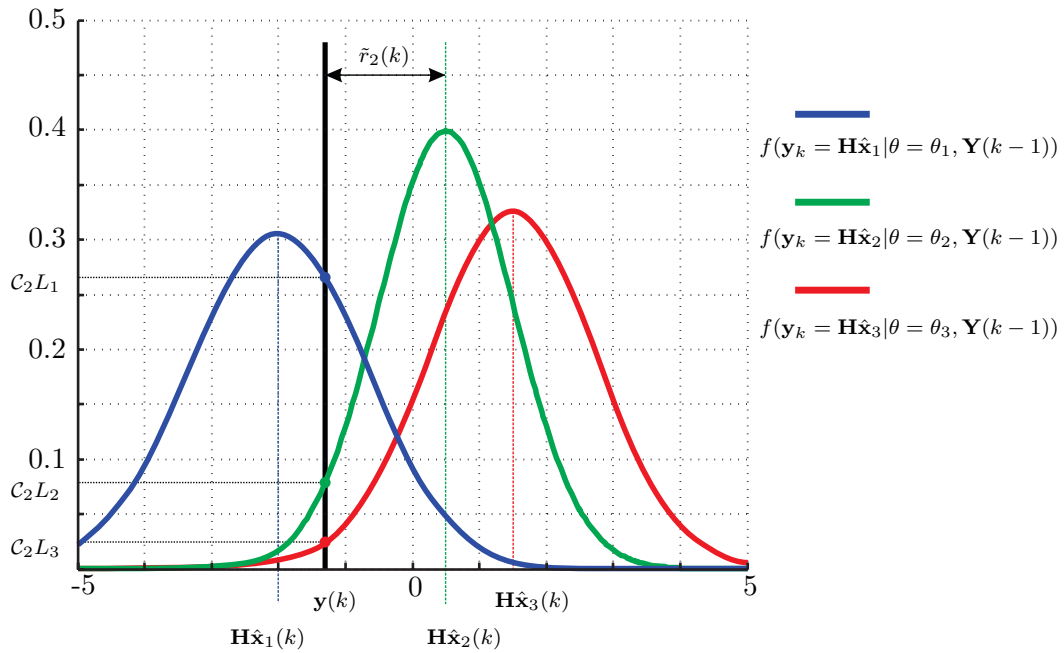


Figure 3.2: Conditional probability density for a one-dimensional feature case with three possible fault scenarios.

probability density functions (PDF) are given, assuming a one-dimensional residual, as if there are only three possible fault hypothesis and one sensor on board the aircraft. These density functions also define the likelihood functions of the three residuals as explained in equation 3.3.17. The predicted values for the sensors, $\mathbf{H}\hat{\mathbf{x}}_i(k)$, are taken as the mean value for the respective PDFs. The residual $\tilde{r}_i(k)$ is taken as the difference between the predicted and observed value for the sensor. In the figure, $\tilde{r}_2(k)$ is shown as an example. The values of the PDFs at the particular value for their residuals (the black vertical line) is then taken as a scaled value for the likelihood \mathcal{L}_i .

An interesting conclusion can be made from figure 3.2. When there is little to no actuator excitation, the residuals will be similar and close to zero. The covariance for the no-fault case is the smallest (see appendix C) and subsequently the PDF relating to the no-fault case will then have the highest peak. The likelihood for the no-fault case will always be the highest even if an actuator is at fault. This shows that the system has difficulty finding faults with small actuator excitation.

3.3.2 State Estimate

The estimated state is determined by a weighted sum of all the different Kalman filters' estimated states. The i^{th} fault scenario will be designated by the subscript i including the no-fault scenario. With this information the state estimate is determined with

$$\hat{\mathbf{x}}(k) = \sum_i \hat{\mathbf{x}}_i(k) p_i(k) \quad (3.3.25)$$

where $\hat{\mathbf{x}}_i(k)$ is the state estimate of the i^{th} filter and $p_i(k)$ is the probability that the i^{th} scenario is active.

3.3.3 Final Decision Process

The information gained from the Bayes classifier must be used to make a final formal decision. This decision will activate the control re-allocation process and inform any users or flight log of the fault. If the Bayes classifier could determine the probability of the fault exactly it would be intuitive to use the probability directly as the fault decision. The classifier is however built upon simplifying assumptions. The same is true for the mathematics describing the matrices used in the Kalman filter, as well as in determining the process and measurement noise covariance matrices.

A conservative decision is then necessary to improve the decision quality. The quality is quantified by its false alarm rate and missed detection rate [8]. A threshold method will be incorporated to define the decision process because of its simplicity and stability. The quality of the decision process will then be tested with the simulation as well as in flight tests. Two thresholds will be used to quantify that a fault has occurred:

1. If the probability of a scenario reaches above 90% it becomes eligible to be classified as active.
2. If a scenario is eligible for longer than two seconds it is classified as active.

A scenario is declared inactive when the probability reaches below 10% for two seconds. When no scenario is declared active according to the decision process thus far, the no-fault scenario is assumed active.

3.4 Simulations for the Bank of Kalman Filters FDI Method

The simulation was run in MATLAB[®] R2008b with the implementation of Simulink. The architecture of the Simulink model is shown in figure 3.3. The non-linear aircraft model uses an embedded code written in C to simulate the aerodynamic, gravitational and thrust forces and moments to determine the position, velocities, attitude and angular rates of the aircraft during simulation.

The simulation also incorporates a simple linear control system to keep the aircraft within its flight envelope and induce desired manoeuvres when necessary. The design and development of the control system falls outside the scope of this research.

amount of natural actuator excitation, as this will probably be the mission with the worst FDI performance. 2.5° locked-in-place faults will only be simulated on the straight and level flight, with minimal process noise, mission.

The measurement and process noise was also simulated in accordance with the covariance matrices determined in appendix C. Note that in the linear Kalman filter the residual and state covariance matrices, as well as the Kalman gains have constant values and can be determined beforehand [35].

The simulation was run for 400 seconds. The system scenario is changed each 30 seconds from a no-fault state to a fault state, then back to a no-fault state. Table 3.1 summarises the sequence of simulated events.

Fault Scenario	Active time in seconds
No-fault	0-30
Right aileron fault	30-60
No-fault	60-90
Left aileron fault	90-120
No-fault	120-150
Right elevator fault	150-180
No-fault	180-210
Left elevator fault	210-240
No-fault	240-270
Right rudder fault	270-300
No-fault	300-330
Left rudder fault	330-360
No-fault	360-400

Table 3.1: Sequence of fault scenarios in the simulation.

In the simulations two important outputs from the FDI system are recorded. The first is the fault decision based on the probability of the faults. The second is the estimated deflections of the actuators.

Each mission's simulation results show seven graphs, each one depicting the probability and decision information for each fault hypothesis. The top graph is the no-fault scenario, the second one the right-aileron fault scenario and so forth until the left rudder fault scenario. In each graph the probability from both the linear and extended Kalman filter is given, as well as the fault decision based on these probabilities.

The decision value is set as unity when the decision is positive for the specific scenario and zero if it is negative. The graphs also show the correct fault decision in dashed lines. The closer the decision output is to the correct fault decision, the better the FDI performance.

The FDI system can accurately estimate the deflection of the actuators. The results of the actuator deflection estimation will only be shown for the last mission (2.5° locked-in-place) as it shows the dynamics and performance of the actuator deflection estimation the best.

3.4.1 Simulation Results for a Straight and Level Flight with Minimal Process Noise

In figure 3.4 it is evident that low process noise, as well as low actuator excitation, gives poor FDI performance. This is exactly what would be expected from the current system. The driving force for isolating the fault is directly coupled with the amplitude of the residuals. The residuals are in turn linked to the amplitude of the actuator excitations. The results are the same for the bank of linear Kalman filters and the bank of extended Kalman filters.

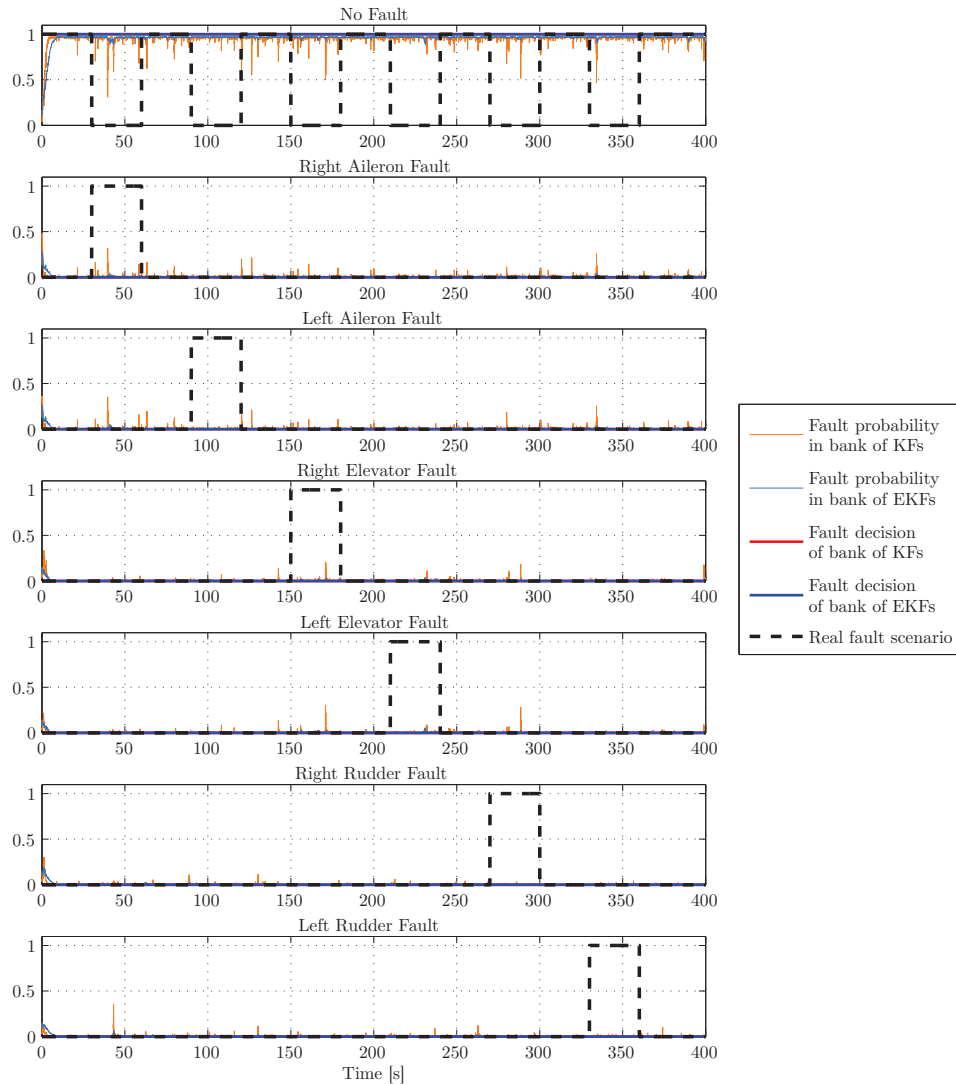


Figure 3.4: Probabilities for a straight and level flight with minimal process noise.

3.4.2 Simulation Results for a Straight and Level Flight with Substantial Process Noise

With substantial process noise in the form of wind there is much better performance than without the wind, as is evident from figure 3.5. The windy simulation induces actuator excitation, which improves the performance of the FDI system. It must be noted however that there is still a considerable amount of time that passes before the fault is isolated. This is due to the fact that the prediction steps in the Kalman filter do not predict the effect of wind. The conclusion is therefore that the FDI performance is more sensitive to actuator excitation than it is to external disturbances.

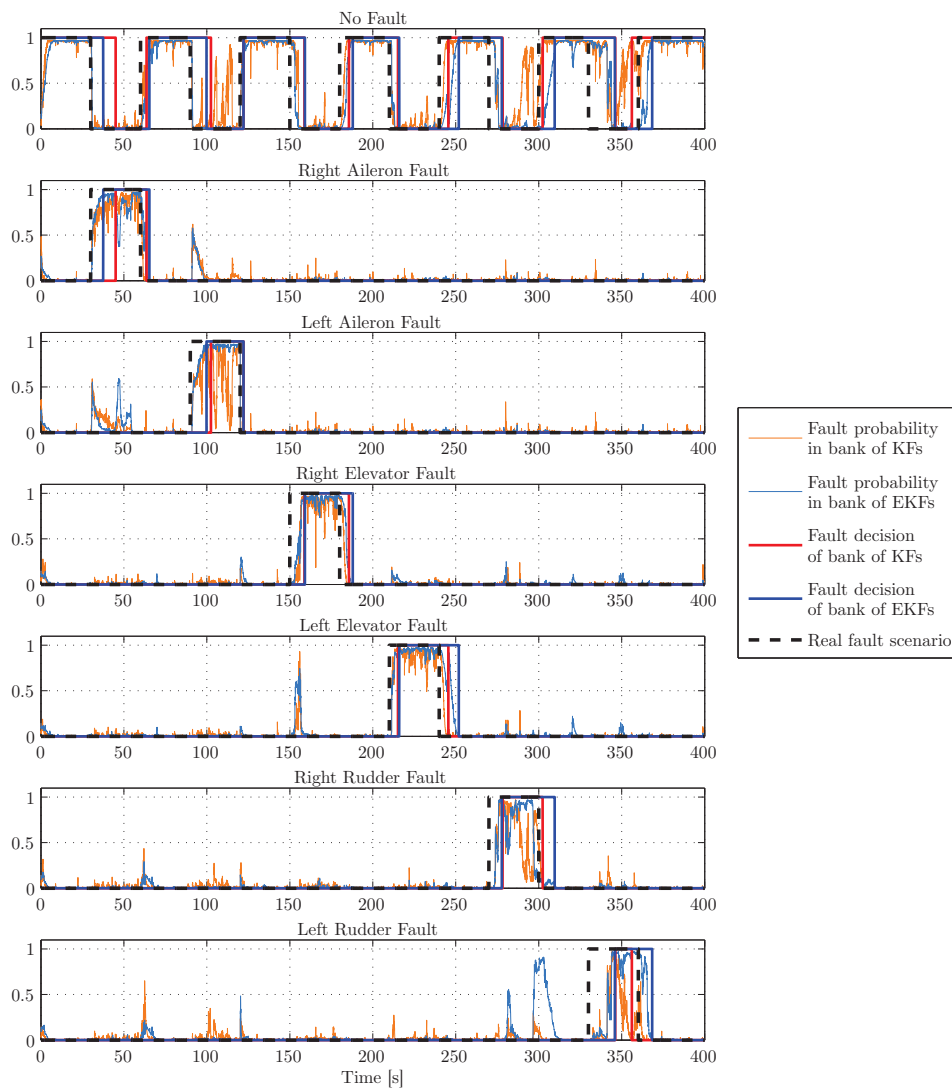


Figure 3.5: Probabilities for a straight and level flight with substantial process noise.

3.4.3 Simulation Results for a Circular Flight Path that Closely Resembles the Flight Test Trajectory

This simulation represents the most realistic of the five simulations. From figure 3.6 it can be seen that the bank of linear Kalman filters perform poorly against the bank of extended Kalman filters. This can be due to the fact that with aircraft manoeuvres the operating point of the aircraft drifts away from the trim conditions. The linear Kalman filters are designed to operate at these trim conditions, whereas the extended Kalman filters can operate in a much larger flight envelope. This is why the bank of extended Kalman filters demonstrate superior performance.

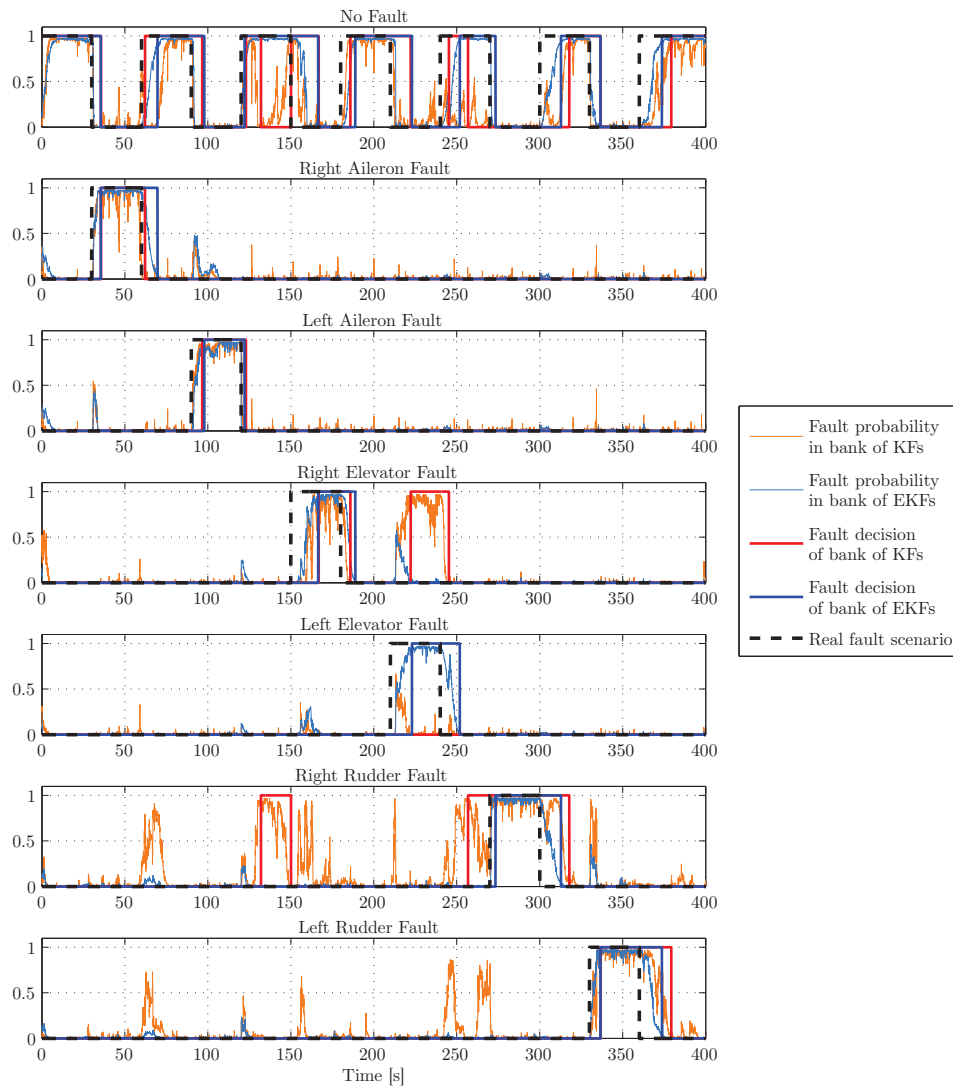


Figure 3.6: Probabilities for a circular flight path that closely resembles the flight test trajectory.

3.4.4 Simulation Results for a Randomly Generated Flight Mission that Induces Actuator Excitation

With the random flight mission the aircraft still stays within the flight envelope, but there is more actuator excitation. This clearly induces much better FDI performance, as can be seen in figure 3.7.

It is important to note that the bank of linear Kalman filters is about one or two seconds faster with some of the fault isolations. This can be attributed to the fact that a linear Kalman filter's Kalman gain and residual covariance matrix remain constant. The extended Kalman filter on the other hand determines the Kalman gain as well as all of its covariance matrices recursively. There will therefore always be some induced error in the extended Kalman filters due to the transients of the recursive processes inside the filter.

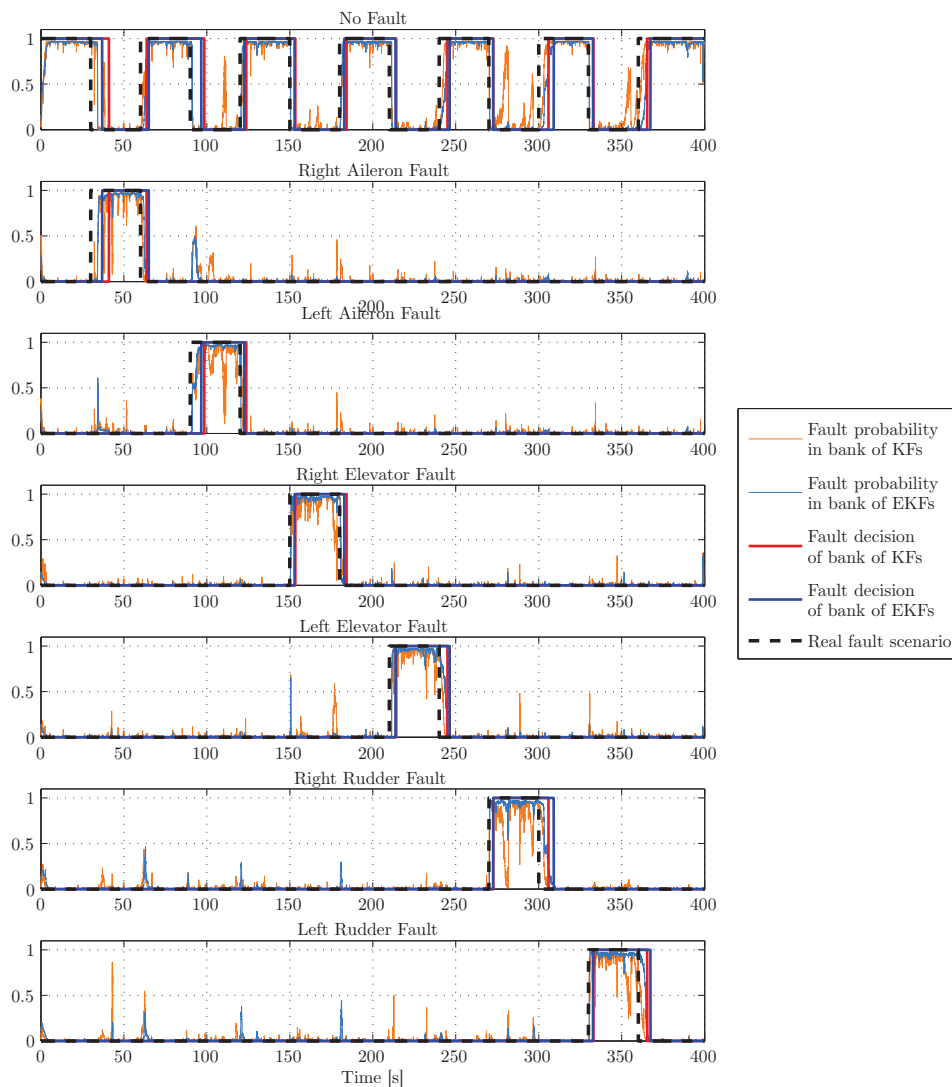


Figure 3.7: Probabilities for a randomly generated flight mission.

3.4.5 Simulation Results for a Straight and Level Flight with Minimal Process Noise, but the Actuators Fail with a Non-Zero Locked-in-Place Fault

The locked-in-place faults create large residuals which in turn allow for exceptional FDI performance as observed in figure 3.8.

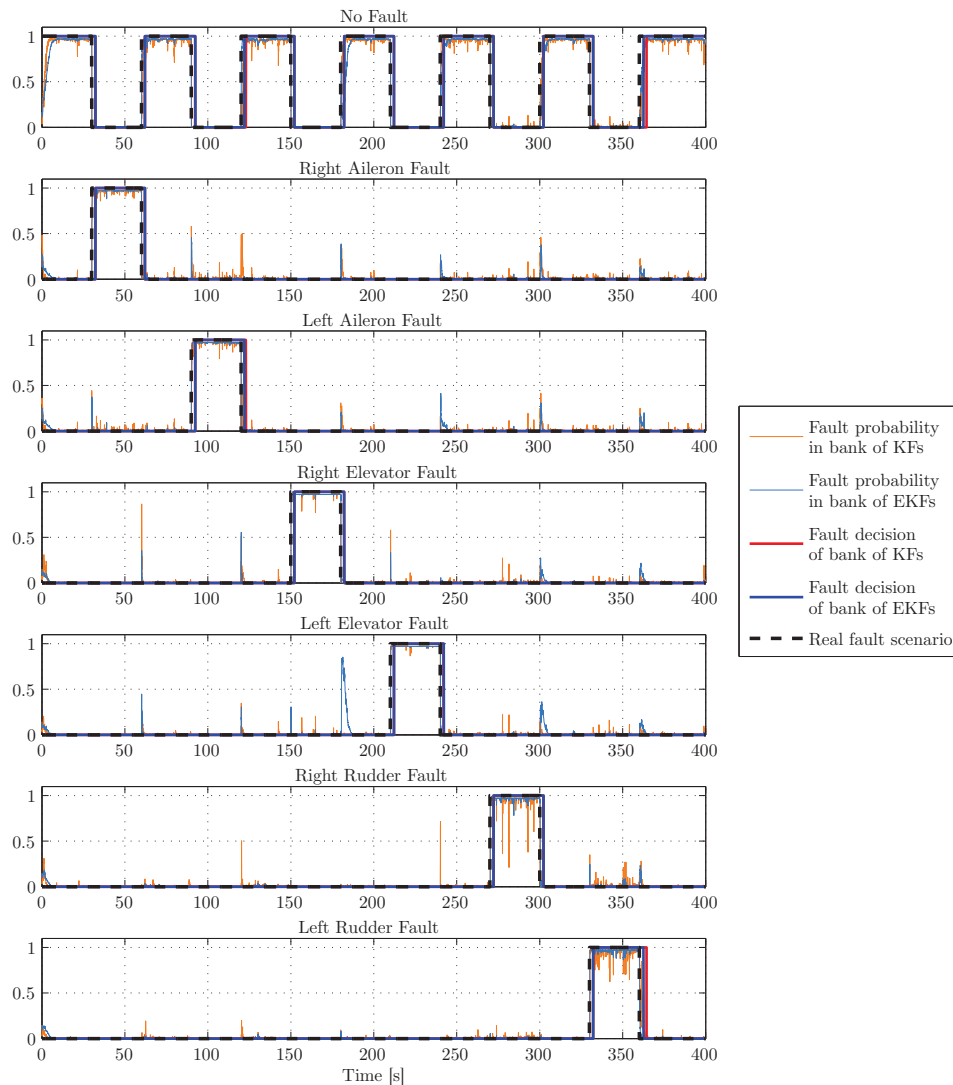


Figure 3.8: Probabilities for a randomly generated flight mission where the actuators fail with a locked-in-place fault of 2.5° .

The actuator deflection estimation is shown in figure 3.9. Only the non-greyed out areas on the graphs are sent to the re-allocation process. It is interesting to note that both the linear and extended Kalman filters estimate the actuator quite accurately.

There is however a very important phenomenon that illustrates the way that the Kalman filters estimate the deflections. Each Kalman filter is set up in such a way that the filter

itself always believes that its own fault scenario is active. For example, the Kalman filter for the left elevator fault is always trying to estimate the true value for only the left elevator. The Kalman gain will always try to steer the estimated variables to values that lie between the measured values and the predicted values. The Kalman filters then try to push the estimated actuator deflection in such a way as to obtain a final state-only estimate that resembles the measured state more closely.

An interesting fact is that the Kalman filters will estimate the actuator deflection even when that particular actuator is not faulty. This is why in figure 3.9 the estimated actuator deflections are erroneous when another fault is occurring (in the greyed out areas). This should not cause any concern, as the information about the estimated actuator deflection is only sent to the control re-allocation process once it is decided that it is indeed that particular actuator that is at fault (non-greyed out areas). This phenomenon also illustrates how easily actuators can have the same effect as other actuators.

For example, the right elevator could induce the same dynamic effect as the faulty right aileron, as seen in figure 3.9 from 30 to 60 seconds. The right elevator is not that effective at mimicking the effect of a left aileron fault, seen as the lower estimated amplitude at 90 to 120 seconds. It must be noted that no single actuator will be able to mimic exactly the effect of another actuator, as is evident from the input matrix as well as the aerodynamic

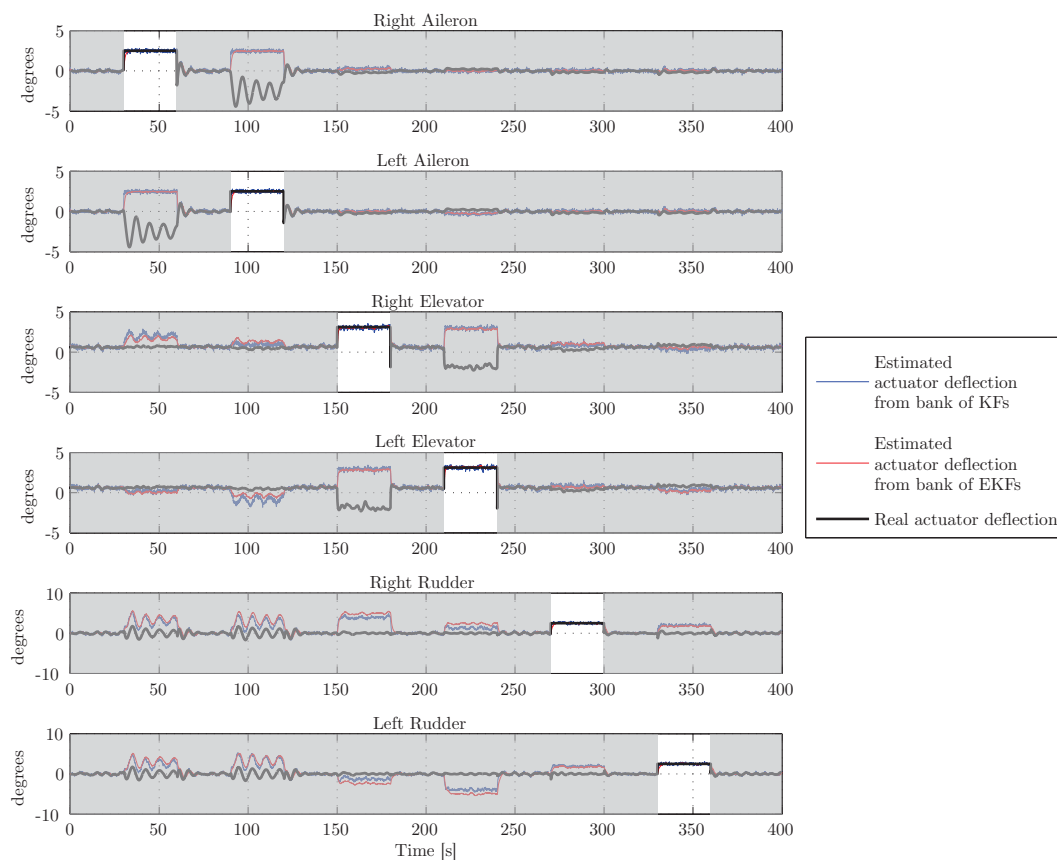


Figure 3.9: Estimated actuator deflections for a random generated flight mission where the actuators fail with a non-zero locked-in-place fault.

control derivatives in appendix A.

3.5 Fault Detection and Isolation Performance

In section 3.4 the performance of the FDI in some typical flight missions were shown. In this section a more comprehensive simulation was run to show the FDI performance over a large range of situations. The simulations were run on only the bank of extended Kalman filters.

According to [8] the quality of an FDI method can be based on the false alarm rate and missed detection rate. The detection performance is further classified by the fault sensitivity, detection time (reaction speed) and robustness. Three separate arrangements were set up on the system of figure 3.3. Several simulations were run on each arrangement to determine the FDI performance. The three arrangements were:

1. The aerodynamic stability and control derivatives were changed to test for robustness. A constant amount of natural actuator excitation and process noise was present.
2. The process noise was increased from zero to a substantial amount of wind to test for robustness.
3. The actuator excitation was increased from zero to 3° amplitude on all actuators to test for fault sensitivity.

All three arrangements also tested for detection time.

For each arrangement, a value was set for its specific simulation parameter (such as the amount of process noise) and ten, 400-second simulations with the same failing sequence as in table 3.1 were run. To test for the false alarm rate, the same simulations were run, but no fault occurred. The number of false alarms were then counted.

The simulation was run ten times with different random values for the process and measurement noise to give a more accurate statistical result. The maximum, minimum and average missed detection and false alarm rates were recorded for the ten simulations. The average values for the detection times and false alarm rates for the separate actuators were also recorded. This process was repeated for all the different simulation parameter values of an arrangement.

The length of a fault was set as 30 seconds. Therefore a detection time larger than 30 seconds indicates a missed fault detection.

Note that these simulations used a bank of extended Kalman filters designed for a specific amount of process noise (see appendix C). In figure 3.12 (section 3.5.3) the effects of using different design values for the process noise covariance matrix will be discussed.

3.5.1 The Effect of Parameter Changes on FDI Performance

The aerodynamic stability and control derivatives were changed from 90% of their original values to 110%. For this arrangement some natural actuator excitation was present, as well as a nominal amount of process noise. The FDI performance is expected to be the greatest at around 100% of the original values, as the Kalman filters were designed with these values.

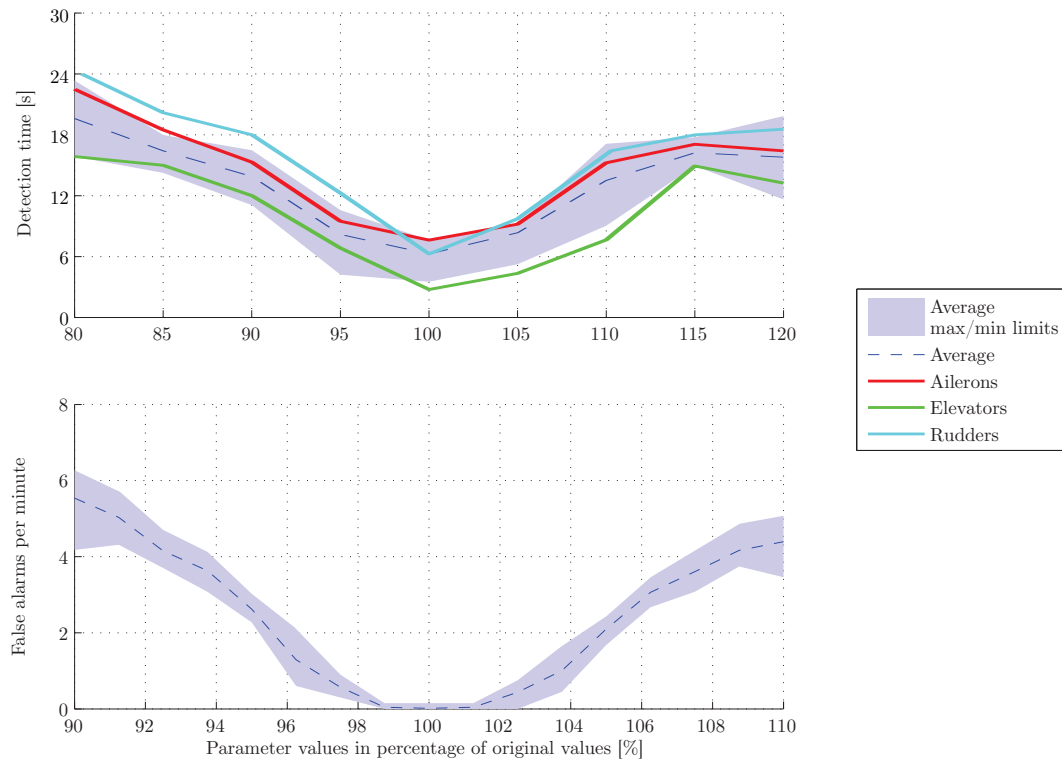


Figure 3.10: The effect of parameter changes on the bank of extended Kalman filters FDI performance.

From figure 3.10 it is seen that the lowest missed detection rate and lowest false alarm rate is around the 100% original aerodynamic values, indicating the best FDI performance at this point. As the aerodynamic values diverge from their original values, the performance of the FDI also degrades. There is a narrow 3% margin to either side of the 100% parameter values where the FDI has less than one false alarm per minute, but beyond 3% parameter change the FDI becomes less effective.

3.5.2 The Effect of Process Noise on FDI Performance

The effect of process noise is twofold. The first effect is that it induces actuator excitation to reject the disturbances, which increases the FDI performance as the process noise increases. However, the uncertainty in process noise creates some confusion in the FDI system and large amounts of process noise therefore degrades the FDI performance.

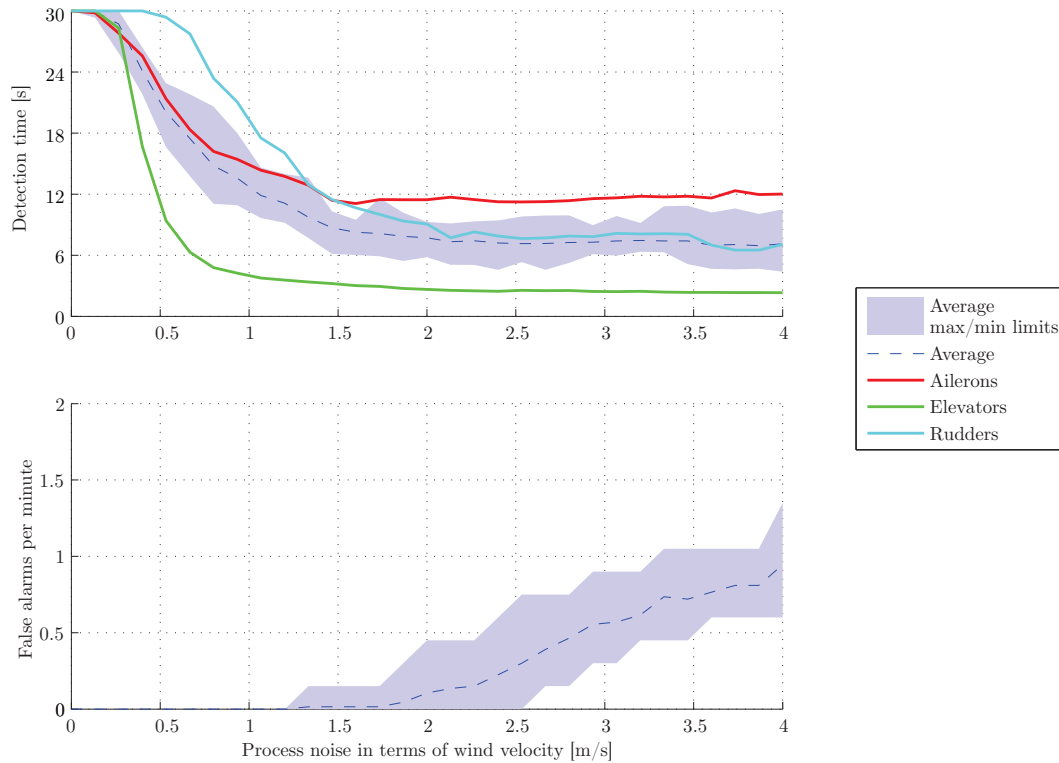


Figure 3.11: The effect of process noise on the bank of extended Kalman filters' FDI performance.

In figure 3.11 it is evident that an increase in process noise improves the detection time as the actuator excitation increases. The false alarms, however, increase as the process noise increases, degrading the FDI performance as expected.

3.5.3 The Effect of Actuator Excitation on FDI Performance

Actuator excitation should have a positive effect on FDI performance, as discussed in section 3.3.1. Note that in figure 3.12 the effect of different process noise covariance matrices on the design of the bank of Kalman filters is shown. The broken lines represent average detection times for the bank of Kalman filters using different process noise covariance matrices. The solid lines represent the detection times for only the simulations using an expected wind velocity of 2 m/s.

The effect of using larger values for the design wind velocity is that the fault sensitivity decreases.

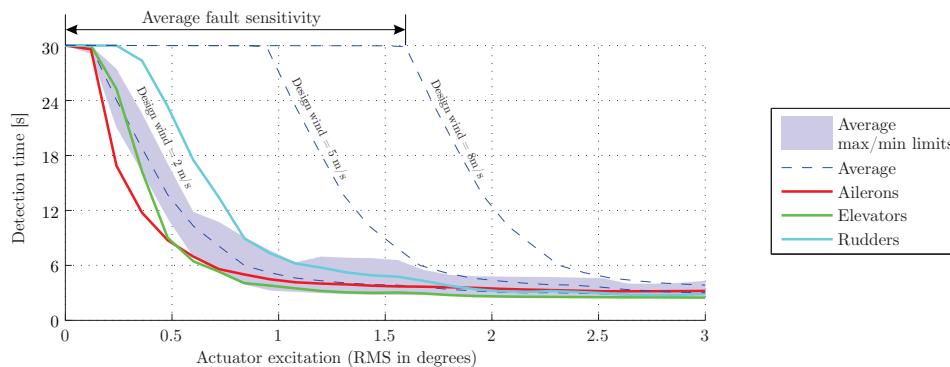


Figure 3.12: The effect of actuator excitation on the bank of extended Kalman filters' FDI performance.

The average fault sensitivity indicates the average size of faults. Smaller faults are not detected and in figure 3.12 this is indicated by the plateau at a detection time of 30 seconds. Note that the length of the fault is chosen randomly at 30 seconds. However, the actual average fault sensitivity should be similar.

In figure 3.12 it can be seen that the performance of the FDI increases significantly with actuator excitation. The FDI performance stabilises at 1° actuator amplitude at about 4 seconds detection time.

As the actuator excitation becomes large, the aircraft tends to fly well outside the trim conditions where non-linearities become significant. The extended Kalman filters are designed to work under these non-linear conditions. This is seen in figure 3.12 as the 4 seconds detection time plateau and does not increase significantly at higher actuator excitation values.

From figure 3.12 it is seen that the aileron fault detection time decrease at lower actuator excitation than the rudders. This implies that aileron faults are more easily detected than rudder faults. The effectiveness of the FDI to detect elevator faults lie between the ailerons and rudders.

The false alarm rates for the bank of Kalman filters are not shown, as no false alarms were detected by increasing actuator excitation on the simulations alone, as was expected. Recall

that the extended Kalman filters are designed to work even at large actuator excitation amplitudes.

Chapter 4

Second Fault Detection and Isolation Method: The Parity Space Approach

As described in figure 1.3, a fault detection and isolation system creates residuals from the aircraft observables, that is, on the command inputs and measured outputs. The parity space approach is a method of pairing all the analytical redundancies between these inputs and outputs of a system. The benefit of the parity space approach is that it provides a quantitative measure of the achievable level of robustness in the residuals in the early stages of a design [23].

4.1 Parity Relations (Analytical Redundancy)

The concept of residual generation stems from analytical redundancy among dissimilar instruments, in which knowledge of the functional relationships among the variables being measured is used [36]. Analytical redundancy can take on two forms:

- Direct redundancy - the functional relationship between components at a specific time step
- Temporal redundancy - the functional relationship between components over a specific time range

The residuals that are created out of these redundancies are the divergence between the expected behaviour and the observed sensor outputs. For an understanding of the analytical redundancy in a system, consider the discrete state space system:

$$\mathbf{x}(k+1) = \mathbf{F}\mathbf{x}(k) + \mathbf{G}\mathbf{u}(k) \quad (4.1.1)$$

$$\mathbf{y}(k) = \mathbf{H}\mathbf{x}(k) \quad (4.1.2)$$

where $\mathbf{x}(k)$ is the N -dimensional state vector, \mathbf{F} is the $N \times N$ state matrix, \mathbf{G} is the $N \times M$ input matrix, and \mathbf{H} is a $L \times N$ constant measurement matrix. It is clear that N is the number of states, M is the number of input actuators and L is the number of sensors. The

vector $\mathbf{u}(k)$ represents the known input to the actuators and the vector $\mathbf{y}(k)$ represents the measurements from the sensors.

Direct redundancy relations exist where a variable measured by a sensor can be obtained through the algebraic relationships of the instantaneous outputs of the other sensors. This implies that there are some rows in \mathbf{H} that are linearly dependent and therefore their output can be compiled as a linear combination of some of the other sensors. Consider for example

$$y_1(k) = \sum_{i=2}^L \alpha_i y_i(k) \quad (4.1.3)$$

where $y_i(k)$ is the i^{th} element in the measurement vector.

In the absence of faults in the sensor or sensor noise, the residual

$$y_1(k) - \sum_{i=2}^L \alpha_i y_i(k) \quad (4.1.4)$$

should be zero. If a large enough residual exists, it would indicate a sensor fault. While sensor faults can be detected, there is a flaw in direct redundancy in that it cannot indicate an actuator fault. Temporal redundancy on the other hand relates sensor outputs and actuator inputs and the potential exists that it can be used to create residuals that can detect actuator faults. This is due to the fact that an actuator's effect is only seen in the next time step (see equation 4.1.1). Temporal redundancy can also facilitate relationships between sensors where no direct redundancy exists.

This extra information in the form of temporal redundancy relations between dissimilar actuators and sensors may detect a greater number of failures, however it does increase the required computational power. The major problem with these relations is the uncertainty in aircraft parameters, process noise and sensor noise. These uncertainties affect the residual signals and can lead to false alarms and missed fault detections. The robustness of the residual generation is therefore of importance.

The parity relations help the design process in this regard. First the redundancies of the components under consideration are determined in the form of parity relations. The residuals, that are the least sensitive to parameter changes and disturbances, are then built up from these relations by means of an optimisation process. The parity relations also enable us to quantify to an extent the effect of uncertainties on residuals.

4.2 The Generalised Parity Space

Let us define from the discrete state space system in equations 4.1.1 and 4.1.2

$$\mathbf{O}(l) = \begin{bmatrix} \mathbf{H} \\ \mathbf{HF} \\ \vdots \\ \mathbf{HF}^l \end{bmatrix} \quad (4.2.1)$$

for the combination of sensors on board the aircraft. The Cayley-Hamilton theorem implies that there exists an $n, 1 \leq n \leq N$, so that the rank of $\mathbf{O}(l)$ can be stated as [23]

$$\text{rank } \mathbf{O}(l) = \begin{cases} l + 1 & l < n \\ n & l \geq n \end{cases} \quad (4.2.2)$$

The null space of the matrix $\mathbf{O}(n - 1)$ is known as the unobservable subspace of the set of sensors. The rows of $\mathbf{O}(n - 1)$ span the observable subspace of the set of sensors and the rows have the dimension N . Note that in the above equation $\mathbf{O}(l)$ has $(n + 1) \times L$ rows while it is only of rank n . The reason for this will become apparent when the parity relations are built up.

To comprehend the generalised parity space, start with defining the set of sensor outputs in terms of the current state and the input signal. From equation 4.1.2

$$\mathbf{y}(k) = \mathbf{H}\mathbf{x}(k) \quad (4.2.3)$$

If temporal redundancy is desired, it is not only the current state that is taken into account, but signals from several time steps (the number of time steps will be determined by the order of the system and the rank of the observability matrix). Taking the next time step signal and substituting equation 4.1.1 into equation 4.2.3 and continuing this process

$$\mathbf{y}(k + 1) = \mathbf{H}\mathbf{x}(k + 1) \quad (4.2.4)$$

$$= \mathbf{H}[\mathbf{F}\mathbf{x}(k) + \mathbf{G}\mathbf{u}(k)] \quad (4.2.5)$$

$$= \mathbf{H}\mathbf{F}\mathbf{x}(k) + \mathbf{H}\mathbf{G}\mathbf{u}(k) \quad (4.2.6)$$

$$\mathbf{y}(k + 2) = \mathbf{H}\mathbf{x}(k + 2) \quad (4.2.7)$$

$$= \mathbf{H}\mathbf{F}\mathbf{x}(k + 1) + \mathbf{H}\mathbf{G}\mathbf{u}(k + 1) \quad (4.2.8)$$

$$= \mathbf{H}\mathbf{F}^2\mathbf{x}(k) + \mathbf{H}\mathbf{F}\mathbf{G}\mathbf{u}(k) + \mathbf{H}\mathbf{G}\mathbf{u}(k + 1) \quad (4.2.9)$$

⋮

$$\mathbf{y}(k + n) = \mathbf{H}\mathbf{x}(k + n) \quad (4.2.10)$$

$$= \mathbf{H}\mathbf{F}^n\mathbf{x}(k) + \mathbf{H}\mathbf{F}^{n-1}\mathbf{G}\mathbf{u}(k) + \dots + \mathbf{H}\mathbf{G}\mathbf{u}(k + n - 1) \quad (4.2.11)$$

time shifted to the most recent sensor output

$$\mathbf{y}(k) = \mathbf{H}\mathbf{x}(k) \quad (4.2.12)$$

$$= \mathbf{H}\mathbf{F}^n\mathbf{x}(k - n) + \mathbf{H}\mathbf{F}^{n-1}\mathbf{G}\mathbf{u}(k - n) + \dots + \mathbf{H}\mathbf{G}\mathbf{u}(k - 1) \quad (4.2.13)$$

The generalisation of equations 4.2.3 to 4.2.11 can be written as

$$\mathbf{Y}(k) = \mathbf{O}\mathbf{x}(k - n) + \mathbf{J}\mathbf{U}(k, n) \quad (4.2.14)$$

where

$$\mathbf{J} = \begin{bmatrix} 0 & 0 \\ \mathbf{HG} & 0 \\ \mathbf{HFG} & \mathbf{HG} \\ \mathbf{HF}^2\mathbf{G} & \mathbf{HFG} \\ \vdots & \\ \mathbf{HF}^{n-1}\mathbf{G} & \mathbf{HF}^{n-2}\mathbf{G} \dots \mathbf{HG} & 0 \end{bmatrix} \quad (4.2.15)$$

$$\mathbf{U}(k, n) = \begin{bmatrix} \mathbf{u}(k-n) \\ \vdots \\ \mathbf{u}(k) \end{bmatrix} \quad (4.2.16)$$

Because the goal of the parity space in fault detection and isolation is the generation of residuals, equation 4.2.14 is rewritten as

$$0 = \mathbf{Y}(k) - \mathbf{O}\mathbf{x}(k-n) - \mathbf{J}\mathbf{U}(k, n) \quad (4.2.17)$$

It is clear from the equation above, that if there were no model uncertainties or noise, the equation would hold if there are no faults occurring. Therefore the above equation relates the output signal, the states and the input signal to one another in the case of a fault-free scenario. It would be best to relate the input signals to the output signals without dependence on the states, thereby eliminating the necessity for a state observer. This can be done by defining the parity vector as

$$\mathbf{P}(k) = \mathbf{\Omega}[\mathbf{Y}(k) - \mathbf{O}\mathbf{x}(k-n) - \mathbf{J}\mathbf{U}(k, n)] \quad (4.2.18)$$

If the left null space $\mathbf{\Omega}$ can be found so that $\mathbf{\Omega}\mathbf{O} = 0$ for any $\mathbf{x}(k)$ then the parity vector gains independence in terms of the system states. To find the left null space, a singular value decomposition is done on \mathbf{O} so that

$$\mathbf{O} = \mathbf{U}\mathbf{S}\mathbf{V}^T \quad (4.2.19)$$

where \mathbf{U} and \mathbf{V} are orthonormal matrices and \mathbf{S} is a rectangular diagonal scaling matrix. The diagonal elements in \mathbf{S} are denoted $s_1, s_2, \dots, s_{\max\{m, n\}}$ and are called the singular values of \mathbf{O} . The columns v_i of \mathbf{V} that correspond to $s_i = 0$ form an orthonormal basis of the null space of \mathbf{O} [37].

When the null space $\mathbf{\Omega}$ is found, equation 4.2.17 is changed into

$$\mathbf{P}(k) = \mathbf{\Omega}\mathbf{Y}(k) - \cancel{\mathbf{\Omega}\mathbf{O}\mathbf{x}(k)} - \mathbf{\Omega}\mathbf{J}\mathbf{U}(k, n_0) \quad (4.2.20)$$

$$\mathbf{P}(k) = \mathbf{\Omega}[\mathbf{Y}(k) - \mathbf{J}\mathbf{U}(k, n)] \quad (4.2.21)$$

Now note that equation 4.2.21 is independent of the state $\mathbf{x}(k)$. In the absence of failures, noise and uncertainty, $\mathbf{P}(k) = \mathbf{0}$. In the presence of zero-mean noise and no failures, $\mathbf{P}(k)$ will be a zero-mean random vector [23]. When a non-zero mean fault occurs, the parity vector will become biased and each different failure will create a different bias in the parity

$$\mathbf{L}_w = \begin{bmatrix} 0 & 0 & 0 & & \\ \mathbf{HS}_w & 0 & 0 & & \\ \mathbf{HFS}_w & \mathbf{HS}_w & 0 & & \\ \mathbf{HF}^2\mathbf{S}_w & \mathbf{HFS}_w & \mathbf{HS}_w & & \\ \vdots & & & & \\ \mathbf{HF}^{n-1}\mathbf{S}_w & \mathbf{HF}^{n-2}\mathbf{S}_w & \mathbf{HF}^{n-3}\mathbf{S}_w & \dots & \mathbf{HS}_w & 0 \end{bmatrix} \quad (4.2.29)$$

$$\mathbf{L}_v = \begin{bmatrix} \mathbf{S}_v & 0 & 0 & & \\ 0 & \mathbf{S}_v & 0 & & \\ 0 & 0 & \mathbf{S}_v & & \\ \vdots & & & & \\ 0 & 0 & 0 & \dots & 0 & \mathbf{S}_v \end{bmatrix} \quad (4.2.30)$$

Note that $\mathbf{P}(k)$ is the parity relations vector and $\mathbf{P}(k, n)$ is the sequence of last $n + 1$ faults. Equation 4.2.24 can be rewritten

$$0 = \mathbf{Y}(k) - \mathbf{O}\mathbf{x}(k) - \mathbf{J}\mathbf{U}(k, n) - \mathbf{L}_f\mathbf{P}(k, n) - \mathbf{L}_w\mathbf{N}_w(k, n) - \mathbf{L}_v\mathbf{N}_v(k, n) \quad (4.2.31)$$

$$0 = \mathbf{\Omega}[\mathbf{Y}(k) - \mathbf{O}\mathbf{x}(k) - \mathbf{J}\mathbf{U}(k, n) - \mathbf{L}_f\mathbf{P}(k, n) - \mathbf{L}_w\mathbf{N}_w(k, n) - \mathbf{L}_v\mathbf{N}_v(k, n)] \quad (4.2.32)$$

$$\mathbf{\Omega}[\mathbf{Y}(k) - \mathbf{J}\mathbf{U}(k, n)] = \mathbf{\Omega}[\mathbf{L}_f\mathbf{P}(k, n) + \mathbf{L}_w\mathbf{N}_w(k, n) + \mathbf{L}_v\mathbf{N}_v(k, n)] \quad (4.2.33)$$

$$\mathbf{P}(k) = \mathbf{\Omega}[\mathbf{Y}(k) - \mathbf{J}\mathbf{U}(k, n)] \quad (4.2.34)$$

$$= \mathbf{\Omega}[\mathbf{L}_f\mathbf{P}(k, n) + \mathbf{L}_w\mathbf{N}_w(k, n) + \mathbf{L}_v\mathbf{N}_v(k, n)] \quad (4.2.35)$$

where equation 4.2.34 describes the residual generator that uses known outputs and inputs to form residuals, and equation 4.2.35 constitutes the unknown disturbances and faults that must be found. The residuals formed by equation 4.2.34 will be called the primary residuals, as they are not yet optimised for fault detection and isolation. A linear transformation of these residuals that optimise the parity relations must be found so that the faults are sufficiently discernable.

4.3 Optimising the Residuals for Fault Detection and Isolation

A linear transformation of equation 4.2.34 can be optimised for FDI. This is done by multiplying equation 4.2.34 with a transformation matrix \mathbf{T} that will be determined in this section:

$$\mathbf{R}(k) = \mathbf{TP}(k) \quad (4.3.1)$$

$$= \mathbf{T}\mathbf{\Omega}[\mathbf{Y}(k) - \mathbf{J}\mathbf{U}(k, n)] \quad (4.3.2)$$

$$= \mathbf{T}\mathbf{\Omega}[\mathbf{L}_f\mathbf{P}(k, n) + \mathbf{L}_w\mathbf{N}_w(k, n) + \mathbf{L}_v\mathbf{N}_v(k, n)] \quad (4.3.3)$$

Recall that any linear combination of the rows in $\mathbf{\Omega}$ still form a null vector when multiplied by \mathbf{O} [37]. The optimisation problem is therefore to find an optimal linear sum of the rows in $\mathbf{\Omega}$ to form a new optimised row. The optimisation will be conducted several times, each time to optimise the sensitivity to a different fault scenario and thereby increasing the discernability

between residuals. The element values in each row of \mathbf{T} resemble the weightings given for each row in $\mathbf{\Omega}$. The different rows $\mathbf{T}_1, \mathbf{T}_2, \dots, \mathbf{T}_i$ in \mathbf{T} therefore resemble the different optimisation solutions for each fault scenario.

4.3.1 The Order of the Parity Space

Looking at the discrete state space system developed in chapter 2 there are five states in $\mathbf{x}(k)$, eight controlled actuators in $\mathbf{u}(k)$ and five sensed values in $\mathbf{y}(k)$. The dimensions for the state space is therefore

$$N = 5 \tag{4.3.4}$$

$$M = 8 \tag{4.3.5}$$

$$L = 5 \tag{4.3.6}$$

For the parity space design the dynamics of the aircraft are linearised around the trim conditions, as was done in chapter 3. In this research it was found that the order n of the observability matrix was five. The order of the parity space is therefore five, which means that the information contained in the residuals spans over six $(n+1)$ time steps. This is done so that a null space of \mathbf{O} can always be found.

The number of actuator faults that will be detected was chosen in chapter 2 to be six. These include detecting and isolating the right and left faults for the ailerons, elevators and rudders of the aircraft.

4.3.2 The Process Noise Input Matrix

The disturbance vector $\mathbf{n}_w(k)$ is assumed to be random white noise (as in chapter 3), but where its covariance matrix will be set as an identity matrix. This is done so that constructing the matrix \mathbf{L}_w in equation 4.2.29 becomes possible. The matrices \mathbf{S}_w then transform $\mathbf{n}_w(k)$ into the effect of process noise on the residuals. \mathbf{S}_w must however be conditioned in such a way as to assist with the optimisation process. To quantify the effect of process noise on the sensors in the parity relations, the matrix \mathbf{S}_w is chosen as the element-by-element square root of the process noise covariance matrix (found in appendix C):

$$\mathbf{S}_w = \begin{bmatrix} 3.39 & 2.84 & 0 & 0 & 0 \\ 2.84 & 4.34 & 0 & 0 & 0 \\ 0 & 0 & 3.89 & 2.37 & 3.35 \\ 0 & 0 & 2.37 & 3.09 & 1.78 \\ 0 & 0 & 3.35 & 1.78 & 4.78 \end{bmatrix} \times 10^{-5} \tag{4.3.7}$$

This gives an approximate standard deviation of the effect that the process noise has on the system.

4.3.3 The Measurement Noise Input Matrix

The measurement noise input matrix \mathbf{S}_v will be taken as the element-by-element square root of the measurement noise covariance matrix for the same reasons as for the process noise input matrix:

$$\mathbf{S}_v = \begin{bmatrix} 4.5 & 0 & 0 & 0 & 0 \\ 0 & 10 & 0 & 0 & 0 \\ 0 & 0 & 4.5 & 0 & 0 \\ 0 & 0 & 0 & 10 & 0 \\ 0 & 0 & 0 & 0 & 4.5 \end{bmatrix} \times 10^{-3} \quad (4.3.8)$$

4.3.4 The Faults Input Matrix

The faults will be described as the difference between the desired actuator deflection and the real actuator deflection. The fault input matrix is then simply the same as the actuator input matrix

$$\mathbf{S}_f = \mathbf{G} \quad (4.3.9)$$

$$\therefore \mathbf{L}_f = \mathbf{J} \quad (4.3.10)$$

With this configuration the estimated actuator deflections can be found by a pseudoinverse estimation technique as will be shown in section 4.5 later.

4.3.5 Multi-Objective Optimisation

The optimisation process will be repeated for each specific fault scenario. The optimisation problem for the FDI has multiple objectives. These objectives relating to the residuals created by equation 4.3.2 are:

1. Increase residual sensitivities if a specific fault occurs
2. Decrease sensitivity to other faults
3. Decrease sensitivity to disturbances

These objectives are combined to form a single aggregate cost function with the use of the well-known weighted linear sum of the individual objectives. The optimisation problem becomes finding a solution of

$$\underset{\mathbf{T}_i}{\text{maximise}} \quad f(\mathbf{T}_i) \quad (4.3.11)$$

$$\text{subject to} \quad g_i(\mathbf{T}_i) \leq 0, \quad i = 1, \dots, m \quad (4.3.12)$$

$$h_i(\mathbf{T}_i) = 0, \quad i = 1, \dots, p \quad (4.3.13)$$

where $f(\mathbf{T}_i)$ is the single aggregate cost function composed of

$$f(\mathbf{T}_i) = c_1 J_1(\mathbf{T}_i) - c_2 J_2(\mathbf{T}_i) - c_3 J_3(\mathbf{T}_i) \quad (4.3.14)$$

and g and h are the inequality and equality constraints, respectively. c_1, c_2 and c_3 is the respective weighting given to each cost function and \mathbf{T}_i is the i^{th} row of the transformation matrix, of which we are trying to optimise the element values.

Six optimisation processes will be conducted, one for each specific fault scenario. With this configuration six residuals will be created with the largest residual resembling the active fault scenario. The cost functions will be set up as follows: the first cost function quantifies the effect of the fault $\theta = \theta_i$ on the residuals

$$J_1(\mathbf{T}_i) = \left(\mathbf{T}_i \boldsymbol{\Omega} \mathbf{L}_f^{(i)} \right)^2 \quad (4.3.15)$$

where $\mathbf{L}_f^{(i)}$ is a matrix made up of all the $i + 6l$ ($l \in [0, 1, \dots, n-1]$) columns of \mathbf{L}_f . When a larger value for c_1 is chosen, the effect will be that more weight is placed on the specific fault, so that the fault is easier to detect in the specific residual.

The second cost function relates the effect of other faults ($\theta \neq \theta_i$) on the residuals and must be minimised

$$J_2(\mathbf{T}_i) = \left(\mathbf{T}_i \boldsymbol{\Omega} \mathbf{L}_f^{(i=0)} \right)^2 \quad (4.3.16)$$

where $\mathbf{L}_f^{(i=0)}$ is a matrix made up of nulling all the $i + 6l$ ($l \in [0, 1, \dots, n-1]$) columns in \mathbf{L}_f . Other faults can corrupt the residual and the value of c_2 is increased so that the optimising procedure penalises other faults. This includes penalising the left actuator if the specific residual is designed for the right actuator and vice versa. There is a strong correlation between the effect of a left and right actuator pair, so increasing c_2 too much can have a negative effect on the quality of the specific residual.

The third cost function quantifies to an uncertain extent the effect that disturbances have on the residuals and should also be minimised:

$$J_3(\mathbf{T}_i) = (\mathbf{T}_i \boldsymbol{\Omega} \mathbf{L}_n)^2 + (\mathbf{T}_i \boldsymbol{\Omega} \mathbf{L}_v)^2 \quad (4.3.17)$$

The consequence of increasing c_3 is to minimise the effect of the disturbances of both the measurement and process noise. All the parity relations are corrupted by disturbances, so increasing c_3 too much will give a solution that produce too small residuals that are meaningless. Another effect of c_3 is that more weight is placed on more recent values of the inputs and outputs as the disturbances have a less cumulative effect on them.

The inequality constraints are that all the elements in \mathbf{T}_i are inside the bound $[-1,1]$ so that the solution can become non-trivial

$$-1 \leq t_{i,j} \leq 1 \quad j = 1, 2, \dots, n \times N \quad (4.3.18)$$

The weightings were determined in an iterative manner. The first iteration was chosen as

$$c_1 = 5 \quad c_2 = 1 \quad c_3 = 1 \quad (4.3.19)$$

This was chosen because the effect of an actuator failure will be about five times smaller than the sum of the other actuator failure effects. The weighting c_3 is set as unity.

4.3.6 Optimisation Technique

The optimisation procedures were implemented using a generalised reduced gradient non-linear optimisation code, which was developed by Leon Lasdon and Alan Waren. More technical information regarding the code can be found at [38]. The implementation of the code can be found in Microsoft® Excel® 2007's solver add-in.

In the optimisation code the conjugate search method is used because of the large number of values that must be optimised. It uses less memory but takes more iterations to reach the solution. The derivatives were computed using central differencing as opposed to forward differencing. Central differencing takes more iterations to find a solution but it is more accurate. The initial estimates were taken as tangent estimates instead of using quadratic estimates. Quadratic estimates are only necessary for highly non-linear systems, which is not the case for this research's optimisation problem.

4.3.7 Optimisation Results

The rows in the transformation matrix \mathbf{T} were arranged so that each row represents a specific fault scenario:

1. Right aileron fault
2. Left aileron fault
3. Right elevator fault
4. Left elevator fault
5. Right rudder fault
6. Left rudder fault

The complexity of the fault and disturbance input matrices made choosing the weightings c_1 , c_2 and c_3 an iterative process to find acceptable solutions. Table 4.1 gives a summary of the final chosen values.

Specific Fault	c_1	c_2	c_3
Right aileron	5	1.6	1
Left aileron	5	1.6	1
Right elevator	5	0.8	1
Left elevator	5	0.8	1
Right rudder	5	0.4	1
Left rudder	5	0.4	1

Table 4.1: Summary of chosen weighting values.

The solutions to the six optimisation procedures are summarised in equation: 4.3.20

$$\begin{bmatrix} \mathbf{T}_1 \\ \mathbf{T}_2 \\ \mathbf{T}_3 \\ \mathbf{T}_4 \\ \mathbf{T}_5 \\ \mathbf{T}_6 \end{bmatrix} = \begin{bmatrix} 0.19 & -0.93 & 0 & 1 & 0 & 0.23 & 0.47 & 0 & 0.30 & 0 & 0.27 & 0.2 & 0 & 0.20 & 0 & 0.3 & 0.13 & 0 & 0.16 & 0 & 0.33 & 0.093 & 0 & 0.14 & 0 \\ -0.19 & 0.93 & 0 & 1 & 0 & -0.23 & -0.47 & 0 & 0.30 & 0 & -0.27 & -0.2 & 0 & 0.20 & 0 & -0.3 & -0.13 & 0 & 0.16 & 0 & -0.33 & -0.093 & 0 & 0.14 & 0 \\ 0.12 & -1 & 0 & 0.17 & 0 & 0.14 & 0.3 & 0 & 0.05 & 0 & 0.16 & 0.07 & 0 & 0.034 & 0 & 0.19 & 0.078 & 0 & 0.027 & 0 & 0.2 & 0.058 & 0 & 0.024 & 0 \\ 0.12 & -1 & 0 & -0.17 & 0 & 0.14 & 0.3 & 0 & -0.05 & 0 & 0.16 & 0.07 & 0 & -0.034 & 0 & 0.19 & 0.078 & 0 & -0.027 & 0 & 0.2 & 0.058 & 0 & -0.024 & 0 \\ 0.019 & -0.093 & 0 & 0 & 0 & 0.023 & 0.047 & 0 & 0 & 0 & 0.026 & 0.02 & 0 & 0 & 0 & 0.03 & 0.013 & 0 & 0 & 1 & 0.033 & 0.0093 & 0 & 0 & 0 \\ -0.019 & 0.093 & 0 & 0 & 0 & -0.023 & -0.047 & 0 & 0 & 0 & -0.026 & -0.02 & 0 & 0 & 0 & -0.03 & -0.013 & 0 & 0 & 1 & -0.033 & -0.0093 & 0 & 0 & 0 \end{bmatrix} \quad (4.3.20)$$

Some interesting features are found in equation 4.3.20. Some of the columns are nulled completely. These columns correspond to rows that have no significant advantage for the optimisation procedure, over the other rows in the primary residuals (equation 4.2.34).

Another feature found in equation 4.3.20 is that the values for the left and right actuator pair's rows are identical except for some values that change in sign. These values correspond to primary residuals on which the effect of the left and right actuators are opposite. These rows therefore help in the process of discerning between the left and right actuator. The values in equation 4.3.20 that are identical correspond to rows in the primary residuals that help to amplify the effect of an actuator type (such as an aileron) irrespective of whether it is a left or right actuator.

4.3.7.1 The Transformation Matrix

The final transformation matrix is then normalised so that each residual produces an amplitude of unity for a 1° of actuator deflection fault. This resulted in a final transformation matrix of

$$\mathbf{T} = \begin{bmatrix} 36.87\mathbf{T}_1 \\ 36.87\mathbf{T}_2 \\ 124.5\mathbf{T}_3 \\ 124.5\mathbf{T}_4 \\ 193.2\mathbf{T}_5 \\ 193.2\mathbf{T}_6 \end{bmatrix} \quad (4.3.21)$$

It is interesting to note that these scaling values roughly correspond to how well the sensors associated with a particular fault scenario can detect that a fault has occurred. Note that before normalisation the residuals are all corrupted by roughly the same amount of unknown disturbances. When a higher value for a residual is required, a greater number of uncertainty is contained in the residual. A higher value therefore indicates difficulty in detecting a fault whereas a smaller value indicates that a fault can be detected more easily. According to the results in equation 4.3.21 it is more difficult for a rudder fault to be detected by the set of sensors than it is for an aileron fault.

4.4 Decision Process

The parity space method for FDI creates residuals of which the mean and variance can increase when a fault has occurred, whereas in the bank of Kalman filters the most correct Kalman filter in the bank will have the smallest residuals. A different decision process is therefore required for the parity space FDI method.

The residuals' mean and covariance depend on whether a fault is active, as well as on the type of fault. When there is no faults the residuals should have a zero mean, as was discussed in section 4.2. When actuator faults occur at zero locked-in-place deflection, the residuals will still have a zero-mean, subject to straight and level flight. When a non-zero locked-in-place fault occurs or the aircraft flies outside the straight and level trim condition, the residuals will exhibit a non-zero mean. There is no prior information on which type of fault will occur and therefore no information regarding how the mean of the residuals will change. The accepted mean for both the healthy and faulty residual distributions will be chosen as zero. The statistical parameters, mean and variance, of the residuals are healthy when no faults are active and faulty when a fault is active.

However when a fault occurs, the variance of the particular residual pertaining to the specific fault will increase. The residuals are also optimised to be sensitive to the specific fault and less sensitive to disturbances and other faults. Hence the residual variance will reflect the variance of the specific fault more closely. The decision process will therefore be specialised to identify a change in residual variance to detect and isolate faults.

4.4.1 The Cumulative Sum Procedure

The cumulative sum (CUSUM) procedure is one of the most powerful and yet simple tools to detect a shift in statistical parameters [39]. The residuals generated by the parity space approach are assumed normally distributed random variables. When a fault occurs the residuals' mean and variance change, given enough actuator excitation. The CUSUM method is therefore suitable to detect these changes in each separate residual and assists in making a fault decision.

The parity functions create sequential residuals at each time step. To derive an iterative method for the CUSUM procedure start by assuming that the sequence of residuals are random variables with a variance that changes when a fault has occurred. The first set of residuals $r_i(1), r_i(2), \dots, r_i(m)$ are assumed to belong to a healthy normal distribution $\mathcal{N}_H(\mu_H, \sigma_H^2)_i$. After m time steps a fault occurs and the rest of the sequence $r_i(m+1), r_i(m+2), \dots, r_i(n)$ belongs to a faulty distribution $\mathcal{N}_F(\mu_F, \sigma_F^2)_i$ where $\mathcal{N}_H(\mu_H, \sigma_H^2)_i \neq \mathcal{N}_F(\mu_F, \sigma_F^2)_i$ and i represents the i^{th} fault residual. Dropping the subscript i , the CUSUM procedure signals that the shift has occurred for the first time [39] when

$$S(k) = \sum_{j=1}^k \ln \frac{f_F(r(j))}{f_H(r(j))} - \min_{n \leq k} \sum_{j=1}^n \ln \frac{f_F(r(j))}{f_H(r(j))} > L \quad (4.4.1)$$

where f_H and f_F are densities corresponding to \mathcal{N}_F and \mathcal{N}_H respectively. The L is a constant that determines the operating characteristics of the CUSUM procedure. The CUSUM procedure in equation 4.4.1 is stated recursively as

$$S(k) = \max \left(S(k-1) + \ln \frac{f_F(r(k))}{f_H(r(k))}, 0 \right) \quad (4.4.2)$$

Equation 4.4.2 can be rescaled by dividing the logarithmic term and L parameter with the same constant. This creates a procedure with the same characteristics that is easier to use.

Assume that the residual belongs to either the healthy normal distribution with variance σ_H^2 or a faulty normal distribution with variance $\sigma_F^2 = C\sigma_H^2$. This type of shift from σ_H^2 to $C\sigma_H^2$ is the simplest shift possible and accurately resembles real shifts in variance [39].

With this setup the logarithmic term in equation 4.4.2 becomes

$$\ln \frac{f_F(r(k))}{f_H(r(k))} = \ln \left(\frac{\frac{1}{\sqrt{2\pi C\sigma_H^2}} e^{(-0.5r^2(k)/(C\sigma_H^2))}}{\frac{1}{\sqrt{2\pi\sigma_H^2}} e^{(-0.5r^2(k)/\sigma_H^2)}} \right) \quad (4.4.3)$$

$$= \ln \left(C^{-\frac{1}{2}} e^{\left(-0.5\left(\frac{r(k)}{\sigma_H}\right)^2\left(\frac{1}{C}-1\right)\right)} \right) \quad (4.4.4)$$

$$= -\frac{1}{2} \ln C + 0.5 \left(\frac{r(k)}{\sigma_H} \right)^2 \left(1 - \frac{1}{C} \right) \quad (4.4.5)$$

Note that the mean values are assumed to be zero as discussed previously. Substituting equation 4.4.5 into 4.4.2 and rescaling it

$$S(k) = \max \left(S(k-1) + \left(\frac{r(k)}{\sigma_H} \right)^2 - K, 0 \right) \quad (4.4.6)$$

where the CUSUM “leak” parameter becomes

$$K = \ln(C) \left(\frac{C}{C-1} \right) \quad (4.4.7)$$

4.4.2 Final Decision Process

The healthy and faulty variance of each residual and each CUSUM’s K value must be found. The residuals are influenced by both the disturbances and the faults. The variance of the residuals are therefore influenced by a combination of the covariances of the disturbances and faults. According to [40] the variance of a linear combination of random signals is given by

$$\text{Cov}(\mathbf{A}\mathbf{X}) = \mathbf{A}\mathbf{\Sigma}\mathbf{A}^T \quad (4.4.8)$$

where \mathbf{A} is a constant matrix and $\mathbf{\Sigma}$ is the covariance matrix of \mathbf{X} . To find the covariance matrix for the healthy set of residuals consider equation 4.3.3, noting that there are no faults present

$$\mathbf{R}_H(k) = \mathbf{T}\mathbf{\Omega}[\mathbf{L}_w\mathbf{N}_w(k, n) + \mathbf{L}_v\mathbf{N}_v(k, n)] \quad (4.4.9)$$

where $\mathbf{T}\mathbf{\Omega}\mathbf{L}_w$ and $\mathbf{T}\mathbf{\Omega}\mathbf{L}_v$ represent the linear transformation of the disturbance vectors $\mathbf{N}_w(k, n)$ and $\mathbf{N}_v(k, n)$ into the residuals respectively. From section 4.3.2 it was decided that the disturbance vectors $\mathbf{n}_w(k)$ and $\mathbf{n}_v(k)$ are assumed to have identity covariance matrices. Looking at equation 4.4.8 the healthy residual covariance matrix can be computed by

$$\text{Cov}(\mathbf{R}_H(k)) = \mathbf{\Sigma}_H \quad (4.4.10)$$

$$= \text{Cov}(\mathbf{T}\mathbf{\Omega}[\mathbf{L}_w\mathbf{N}_w(k, n) + \mathbf{L}_v\mathbf{N}_v(k, n)]) \quad (4.4.11)$$

$$= \text{Cov}(\mathbf{T}\mathbf{\Omega}\mathbf{L}_w\mathbf{N}_w(k, n)) + \text{Cov}(\mathbf{T}\mathbf{\Omega}\mathbf{L}_v\mathbf{N}_v(k, n)) \quad (4.4.12)$$

$$= (\mathbf{T}\mathbf{\Omega}\mathbf{L}_w)\mathbf{\Sigma}_{\mathbf{N}_w(k, n)}(\mathbf{T}\mathbf{\Omega}\mathbf{L}_w)^T + (\mathbf{T}\mathbf{\Omega}\mathbf{L}_v)\mathbf{\Sigma}_{\mathbf{N}_v(k, n)}(\mathbf{T}\mathbf{\Omega}\mathbf{L}_v)^T \quad (4.4.13)$$

$$= (\mathbf{T}\mathbf{\Omega}\mathbf{L}_w)\mathbf{I}(\mathbf{T}\mathbf{\Omega}\mathbf{L}_w)^T + (\mathbf{T}\mathbf{\Omega}\mathbf{L}_v)\mathbf{I}(\mathbf{T}\mathbf{\Omega}\mathbf{L}_v)^T \quad (4.4.14)$$

This method of obtaining the healthy variances proved effective and compared well to the healthy variances obtained through simulations. The variance for each fault residual was found to be equal for the left and right actuator pairs. The covariances between left and right residual pairs were also found to be strongly correlated, which makes sense as the effect of a right actuator fault is similar to that of a left actuator fault. The calculated healthy residual covariance matrix $\mathbf{\Sigma}_H$ can be found in appendix D.1. It is interesting to note that the variances are higher for the residuals that are concerned with the rudders and lower for those concerned with the ailerons. The transformation matrix from equation 4.3.21 gives more weight to the rudder residuals and less to the aileron residuals. The disturbances therefore have a greater effect on the residuals concerned with the rudders. The variances on the rudder residuals are therefore expected to be higher. Other factors, such as the specific values in the rows of \mathbf{T} , also influence the variances obtained in equation D.1.2.

Looking at the residuals with the effect of the i^{th} additive actuator fault without the effects of other faults or disturbances, equation 4.3.3 can be written as

$$\mathbf{R}_{F,i}(k) = \mathbf{T}\mathbf{\Omega}\mathbf{L}_f^{(i)}\mathbf{P}^{(i)}(k, n) \quad (4.4.15)$$

where $\mathbf{L}_f^{(i)}$ is the fault input matrix made up of only the columns of \mathbf{L}_f relating to the i^{th} fault and $\mathbf{P}^{(i)}$ is the sequence of faults pertaining to only the i^{th} fault

$$\mathbf{P}^{(i)}(k, n) = \begin{bmatrix} f_i(k-n) \\ f_i(k+1-n) \\ \vdots \\ f_i(k) \end{bmatrix} \quad (4.4.16)$$

In relation to equation 4.4.8 the variance of the residual due to only the i^{th} fault is

$$\text{Cov}(\mathbf{R}_{F,i}(k)) = (\boldsymbol{\Sigma}_{F,i})_{\mathbf{N}(k,n)=0} \quad (4.4.17)$$

$$= (\mathbf{T}\boldsymbol{\Omega}\mathbf{L}_f^{(i)})_{\boldsymbol{\Sigma}_{\mathbf{P}^{(i)}(k,n)}}(\mathbf{T}\boldsymbol{\Omega}\mathbf{L}_f^{(i)})^T \quad (4.4.18)$$

To obtain the faulty residual variance, examine the covariance matrix of the nondeterministic additive fault

$$\boldsymbol{\Sigma}_{\mathbf{P}^{(i)}(k,n)} = E \left[(\mathbf{P}^{(i)}(k, n) - E[\mathbf{P}^{(i)}(k, n)])(\mathbf{P}^{(i)}(k, n) - E[\mathbf{P}^{(i)}(k, n)])^T \right] \quad (4.4.19)$$

simplifying $\mathbf{P}^{(i)}(k, n)$ as \mathbf{P}_k and $f_i(k-n)$ as f_{-n}

$$\boldsymbol{\Sigma}_{\mathbf{P}_k} = \begin{bmatrix} \text{Var}(f_{-n}) & \text{Cov}(f_{-n}, f_{-n+1}) & \cdots & \text{Cov}(f_{-n}, f_0) \\ \text{Cov}(f_{-n+1}, f_{-n}) & \text{Var}(f_{-n+1}) & & \text{Cov}(f_{-n+1}, f_0) \\ \vdots & & \ddots & \vdots \\ \text{Cov}(f_0, f_{-n}) & \text{Cov}(f_0, f_{-n+1}) & \cdots & \text{Var}(f_0) \end{bmatrix} \quad (4.4.20)$$

Once a fault has occurred, the signal $\mathbf{P}_{k+\tau}$ is assumed statistically stationary and τ is an arbitrary lag time. Therefore all the variances in equation 4.4.20 are equal and all the covariances with the same time shift will also be equal

$$\left. \begin{array}{l} \text{Var}(f_{-n}) = \text{Var}(f_{-n+\tau}) \\ \text{Cov}(f_{-n}, f_{-n+\tau}) = \text{Cov}(f_{-n+c}, f_{-n+\tau+c}) \end{array} \right\} \tau, c \in \mathbb{N} \quad (4.4.21)$$

where c is also an arbitrary lag time. The problem of finding the covariance matrix in equation 4.4.20 is reduced to finding the following $n+1$ covariances:

$$\begin{array}{l} \text{Var}(f_\tau) = \text{Cov}(f_\tau, f_\tau) \\ \text{Cov}(f_\tau, f_{\tau+1}) \\ \vdots \\ \text{Cov}(f_\tau, f_{\tau+n}) \end{array} \quad (4.4.22)$$

The variance of \mathbf{P}_τ is dependent on the type and size of the fault, whereas the covariances are also dependent on the frequency of the fault. No prior information indicating the frequency and amplitudes of the faults is available. A nominal fault frequency and amplitude must therefore be chosen to determine the covariances. It is advantageous to choose a lower limit on the fault amplitude that must be detected, because even if a low limit is chosen, a larger

fault will still be detected even better by the CUSUM procedure. A too low limit however can corrupt the quality of the procedure by allowing the disturbances to have a greater affect on the fault decision.

A minimum fault amplitude of 1° (0.01745 rads) was chosen as the lower limit of fault detection. The fault frequency was chosen as the lowest natural frequency of the aircraft system. Determined from the eigenvalues of the continuous state matrix in equation 2.11.14, the lowest frequency was 0.9 rad/s. From these parameters and remembering $n = 5$, the following values were obtained for the fault covariances:

$$\text{Var}(f_\tau) = 1.523 \times 10^{-4} \quad (4.4.23)$$

$$\text{Cov}(f_\tau, f_{\tau+1}) = 1.522 \times 10^{-4} \quad (4.4.24)$$

$$\text{Cov}(f_\tau, f_{\tau+2}) = 1.519 \times 10^{-4} \quad (4.4.25)$$

$$\text{Cov}(f_\tau, f_{\tau+3}) = 1.514 \times 10^{-4} \quad (4.4.26)$$

$$\text{Cov}(f_\tau, f_{\tau+4}) = 1.507 \times 10^{-4} \quad (4.4.27)$$

$$\text{Cov}(f_\tau, f_{\tau+5}) = 1.498 \times 10^{-4} \quad (4.4.28)$$

With equation 4.4.18 the covariance matrices of the faulty residuals for each different fault were determined and can be found in appendix D.2. It is interesting to see that all the faulty residuals have the same variance for the same size and type of fault. This is in line with the objective of scaling the residuals so that a 1° fault would show an amplitude of 1. The variance of $\sigma^2 = 0.5$ is the same as the variance of a sinusoidal signal with an amplitude of 1. Note that these covariances do not reflect the effects of disturbances. The disturbances are assumed to not change when a fault occurs and their statistical behaviour remains the same. With disturbances

$$\mathbf{R}_{F,i}(k) = \mathbf{T}\mathbf{\Omega} \left[\mathbf{L}_f^{(i)} \mathbf{P}^{(i)}(k, n) + \mathbf{L}_n \mathbf{N}(k, n) \right] \quad (4.4.29)$$

$$\text{Cov}(\mathbf{R}_{F,i}(k)) = \text{Cov}(\mathbf{T}\mathbf{\Omega}\mathbf{L}_f^{(i)} \mathbf{P}^{(i)}(k, n)) + \text{Cov}(\mathbf{T}\mathbf{\Omega}\mathbf{L}_n \mathbf{N}(k, n)) \quad (4.4.30)$$

$$\therefore \mathbf{\Sigma}_{F,i} = (\mathbf{\Sigma}_{F,i})_{\mathbf{N}(\tau,n)=0} + \mathbf{\Sigma}_{H,i} \quad (4.4.31)$$

Note that the values in the healthy covariance matrices are higher than in the faulty (without disturbances) case. This implies that the faults have a smaller effect than the disturbances. The frequencies of the faults are assumed to be much lower than that of sensor noise and other disturbances. If the residuals are put through a low pass filter the variance of the fault should not decrease dramatically, but the high frequency disturbances from the sensors can be attenuated.

The healthy covariance matrix was recalculated when the residuals were passed through a low pass filter with a bandwidth of 2π rad/s. The 2π rad/s was seen to attenuate the measurement noise significantly without losing much effect from the faults. The new healthy covariance matrix was determined from simulation and can be found in appendix D.1. The final faulty residuals covariance matrices can be found in appendix D.3.

The CUSUM procedure will focus only on determining a shift in each separate residual's variance. The covariance matrices in appendix D.3 give an indication of how faults can

corrupt the residual not concerned with the fault at hand. How the decision process deals with the coupling between the left and right actuator residual pairs are dealt with later in this section. From the covariance matrices it is easy to determine the values for C by dividing the faulty variances with the healthy variances. Note that the left and right actuator pairs have the same C , K and L values.

$$C_A = 49.29 \quad (4.4.32)$$

$$C_E = 20.5 \quad (4.4.33)$$

$$C_R = 5.88 \quad (4.4.34)$$

$$\therefore K_A = 3.98 \quad (4.4.35)$$

$$K_E = 3.18 \quad (4.4.36)$$

$$K_R = 2.13 \quad (4.4.37)$$

The values of L were determined to detect a fault in at least four seconds with the minimum fault amplitude of 1° . This was determined with the help of simulations as

$$L_A = 130 \quad (4.4.38)$$

$$L_E = 120 \quad (4.4.39)$$

$$L_R = 120 \quad (4.4.40)$$

A limit was also placed on the CUSUM procedure so that after a fault has occurred and the system is back in a no-fault scenario, the decision process will be able to see that the system is back to a no-fault scenario. The limits were chosen as double the CUSUM's respective L values so that the no-fault scenario can also be detected in a minimum time of 4 seconds. The residuals have been optimised to be insensitive to other faults but there are always some effects of the faults that spill into the other residuals. This phenomenon is particularly visible in the left-right actuator pairs of all the CUSUMs, as can be seen in the strong correlations in the covariance matrices in appendix D.3. To discern between the left and right faults, another set of CUSUM procedures run in parallel. They do not have upper limits imposed on them, but the CUSUM values are reset once the limited CUSUM process have small values. This assists the decision process in distinguishing between the left and right actuator pairs in the way described in figure 4.1.

Figure 4.1 represents a conceptual CUSUM procedure checking the variance of the left and right actuator pairs respectively. The limited CUSUM procedure is used to detect if a fault is active or inactive. A fault is declared active if a CUSUM has crossed the detection limit L and a fault is declared inactive when no CUSUM is above that limit. The unlimited CUSUM procedure is used when more than one CUSUM is above the detection limit. In this case the maximum CUSUM in the unlimited CUSUM procedure is chosen as the active fault scenario. This greatly increases the accuracy of the fault diagnosis. The unlimited CUSUM procedure's CUSUMs can increase to high levels when a fault is active for a long enough time. Therefore when the limited CUSUM procedure's CUSUMs are low enough, the unlimited CUSUMs are reset. In figure 4.1 the right actuator developed a fault whereafter both the left and right CUSUMs increased. The unlimited CUSUM procedure helped to

disturbance term. The i^{th} fault can be estimated as

$$\therefore \mathbf{P}^{(i)}(k, n) \approx \left(\boldsymbol{\Omega} \mathbf{L}_f^{(i)} \right)^{-1} \boldsymbol{\Omega} [\mathbf{Y}(k) - \mathbf{J} \mathbf{U}(k, n)] \quad (4.5.3)$$

$$f_i(k) = \text{mean} \left(\left(\boldsymbol{\Omega} \mathbf{L}_f^{(i)} \right)^{-1} \boldsymbol{\Omega} [\mathbf{Y}(k) - \mathbf{J} \mathbf{U}(k, n)] \right) \quad (4.5.4)$$

The $\left(\boldsymbol{\Omega} \mathbf{L}_f^{(i)} \right)^{-1}$ term is a pseudo inverse of the rectangular matrix $\boldsymbol{\Omega} \mathbf{L}_f^{(i)}$. The pseudo inverse matrix represents a least squares best fit solution to the system of linear equations in 4.5.4 that calculates the i^{th} actuator deflection fault from information from the sensors and the actuator inputs. The actuator deflection is then estimated as the sum of the input signal and the fault signal

$$\hat{\delta}_i = f_i(k) + u_i(k) \quad (4.5.5)$$

It is interesting to note that the same phenomenon present in section 3.4.5 can be seen with equation 4.5.4. Equation 4.5.4 is always calculating the i^{th} actuator deflection fault to best describe the observations from the sensors and inputs. This happens even though the i^{th} actuator is not at fault.

4.6 Simulations for the Parity Space FDI Method

The simulations for the parity space FDI method were run in MATLAB[®] R2008b with the implementation of Simulink. The architecture of the Simulink model is shown in figure 4.2. The only difference between this simulation and the bank of Kalman filters' simulation (figure 3.3) is the different FDI module. The control system, aircraft model, process noise and measurement noise are all the same.

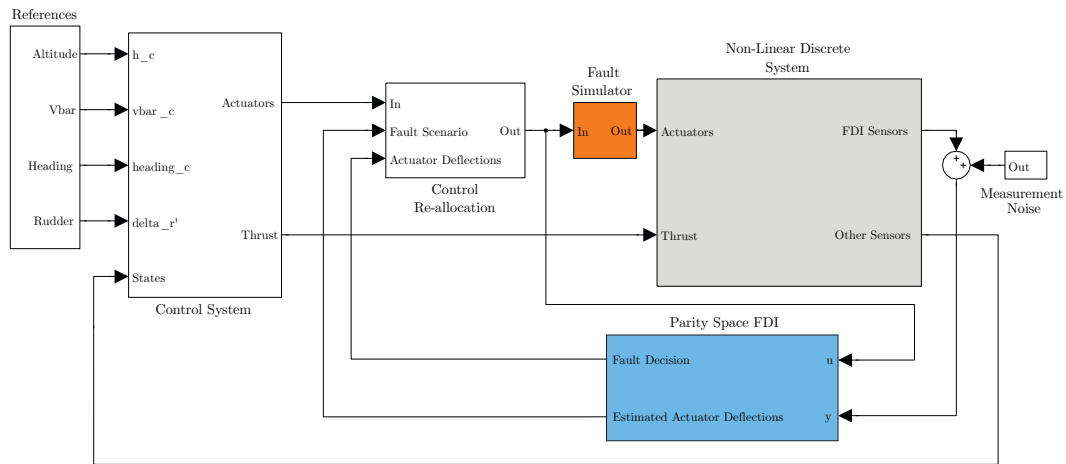


Figure 4.2: The Simulink model used to simulate the performance of a parity space FDI method.

The same five simulated missions were conducted as for the bank of Kalman filters in section 3.4. The length of the simulation was kept at 400 seconds and the length of the active faults

at 30 seconds each. The different flight missions that were simulated are repeated below. They are:

1. Straight and level flight with minimal process noise
 - 0° degree locked-in-place fault for each fault scenario
2. Straight and level flight with substantial process noise
 - 0° degree locked-in-place fault for each fault scenario
3. A circular flight path that closely resembles the flight test trajectory
 - 0° degree locked-in-place fault for each fault scenario
4. A zero-mean random generated flight mission that induces actuator excitation
 - 0° degree locked-in-place fault for each fault scenario
5. Straight and level flight with minimal process noise
 - 2.5° degree locked-in-place fault for each fault scenario

In the simulation results (section 4.6.1 to 4.6.5) a decision is declared if the value on the graph is unity. The decision is undeclared when the value is zero. The desired behaviour of the FDI system's decision is to follow the actual fault scenario as closely as possible.

The parity space FDI should be able to estimate the actual actuator deflections. The actuator deflection estimates will be shown for the last mission only (figure 4.8), as it clearly shows the dynamics and performance of the actuator deflection estimation process.

4.6.1 Simulation Results for a Straight and Level Flight with Minimal Process Noise

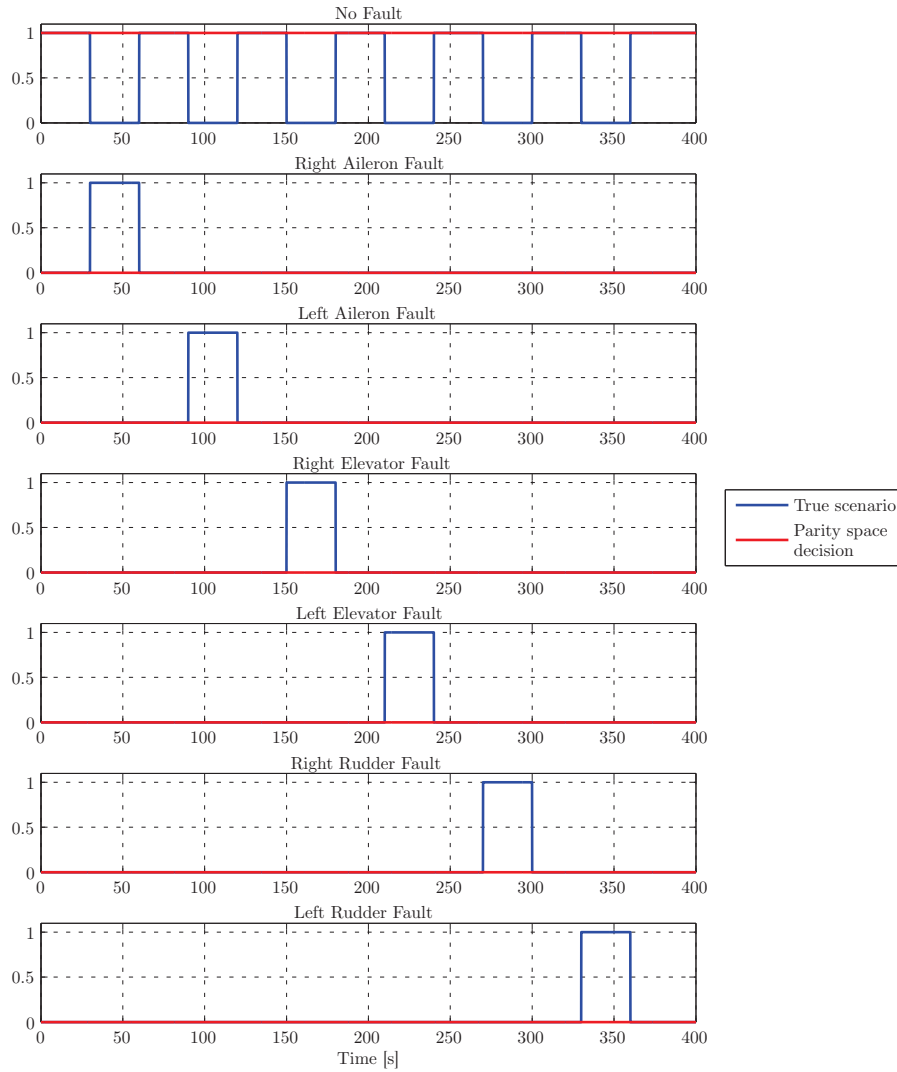


Figure 4.3: Fault decisions for a straight and level flight with minimal process noise.

In the case of a straight and level flight with minimal process noise, low actuator excitation is expected. In figure 4.3 it can be seen that the FDI process could not isolate any faults. This result was expected as no actuator had any significant level of excitation, while the CUSUM method required some level of actuator excitation to detect faults.

4.6.2 Simulation Results for a Straight and Level Flight with Substantial Process Noise.

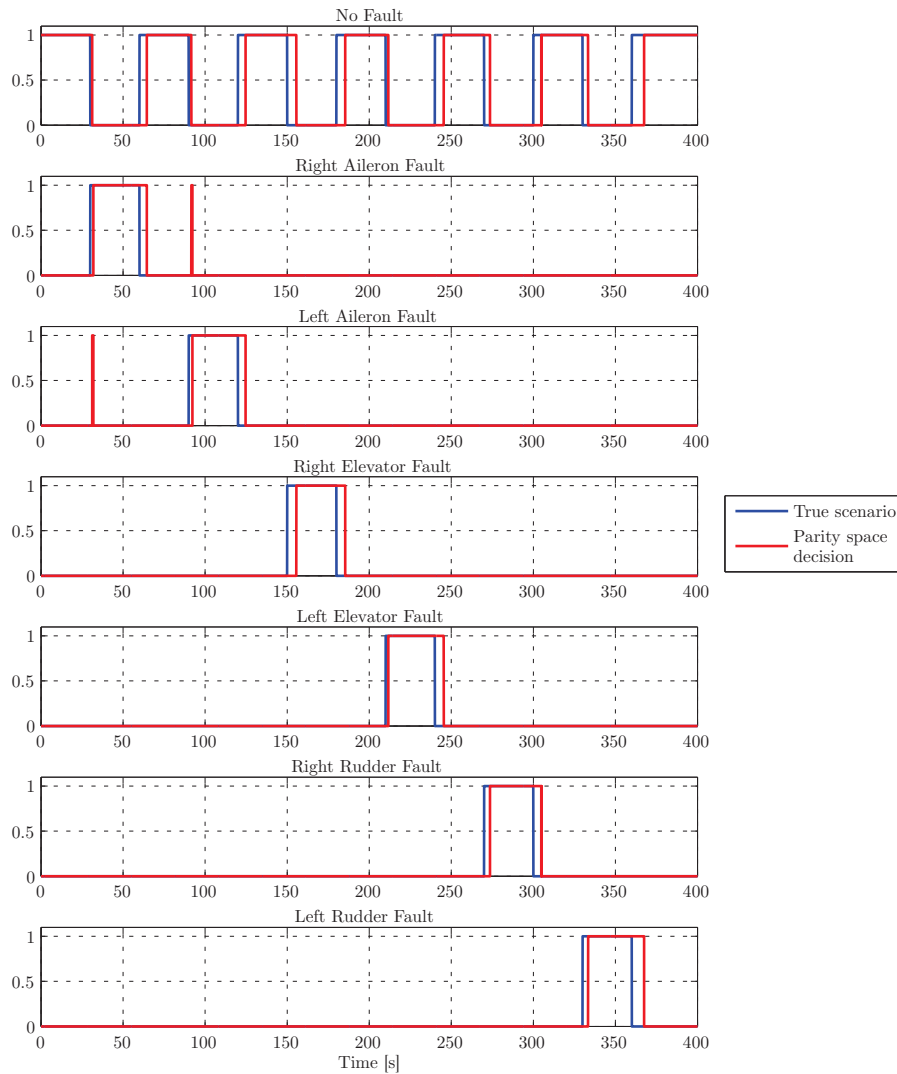


Figure 4.4: Fault decisions for a straight and level flight with substantial process noise.

The extra process noise increases the performance of the FDI process significantly. The aileron faults are detected after two seconds, but it takes another second to correctly discern which aileron is at fault. This can be attributed to the negative effect of unwanted disturbances, which can lead to the wrong aileron CUSUM having a slightly higher value. The right aileron CUSUM eventually increases enough and the correct isolation is done. The removed aileron faults are detected after four seconds.

The elevator faults are detected after six seconds. The detection of a removed fault also takes about six seconds.

The rudder faults are isolated within four seconds and the removal of the fault is detected after eight seconds. It takes a longer time to detect the removal of the rudder faults, since the effect of disturbances on the rudder residuals are larger than on the other actuators. Disturbances increase the residual variances and therefore can help with the detection of a fault, but it hampers the detection of a removed fault.

4.6.3 Simulation Results for a Circular Flight Path that Closely Resembles the Flight Test Trajectory.

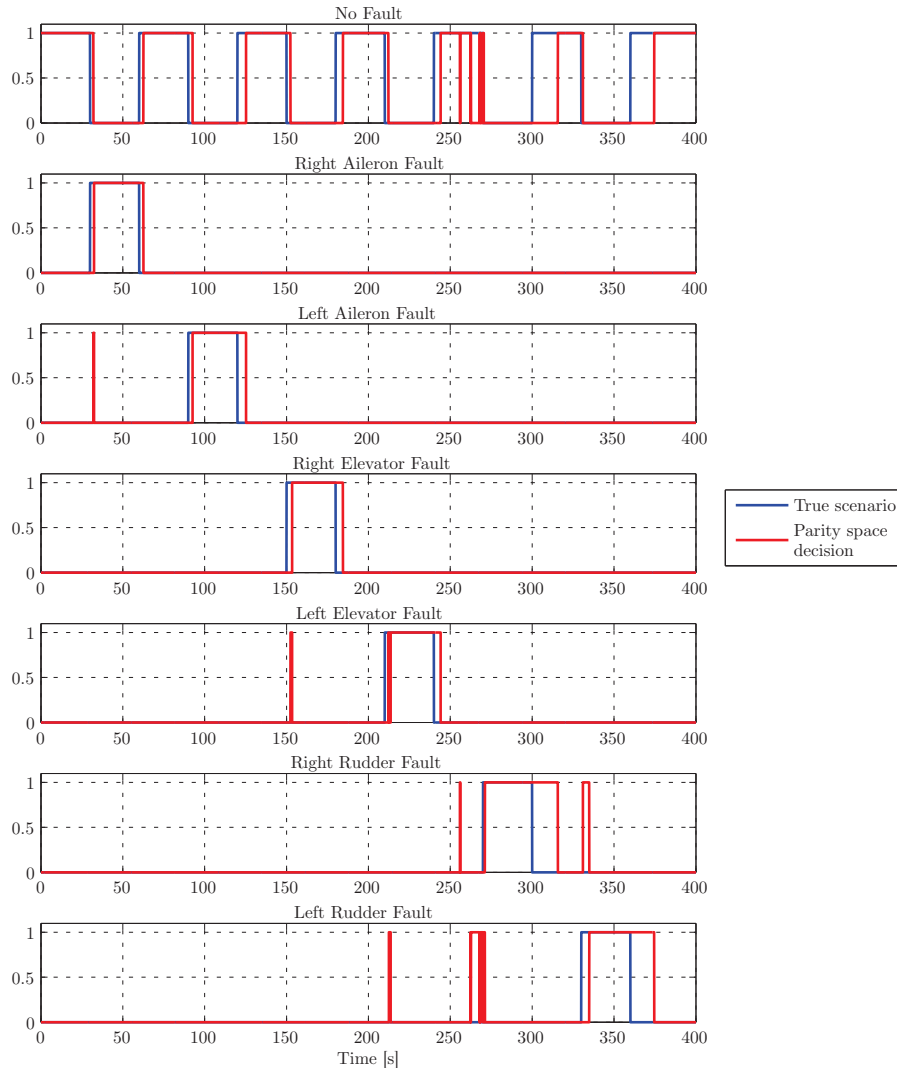


Figure 4.5: Fault decisions for a circular flight path that closely resembles the flight test trajectory.

For the circular flight trajectory the FDI isolated aileron faults within three seconds, as can be seen in figure 4.5. Some expected confusion exists at the onset of the right aileron fault but is quickly corrected. The aileron faults are declared removed after four seconds.

The elevator faults are also detected and isolated within three seconds and a removed elevator fault detected after four seconds.

It is evident from figure 4.5 that the parity space method has trouble isolating rudder faults. In this mission the aircraft is flying a circular trajectory, which creates biases in the yaw and pitch rates of the aircraft. The parity space approach is designed around a trim working condition. The manoeuvres of the aircraft allow it to fly outside the trim conditions. This created unwanted parity space residual signals and subsequently degrades the FDI performance.

4.6.4 Simulation Results for a Random Generated Flight Mission.

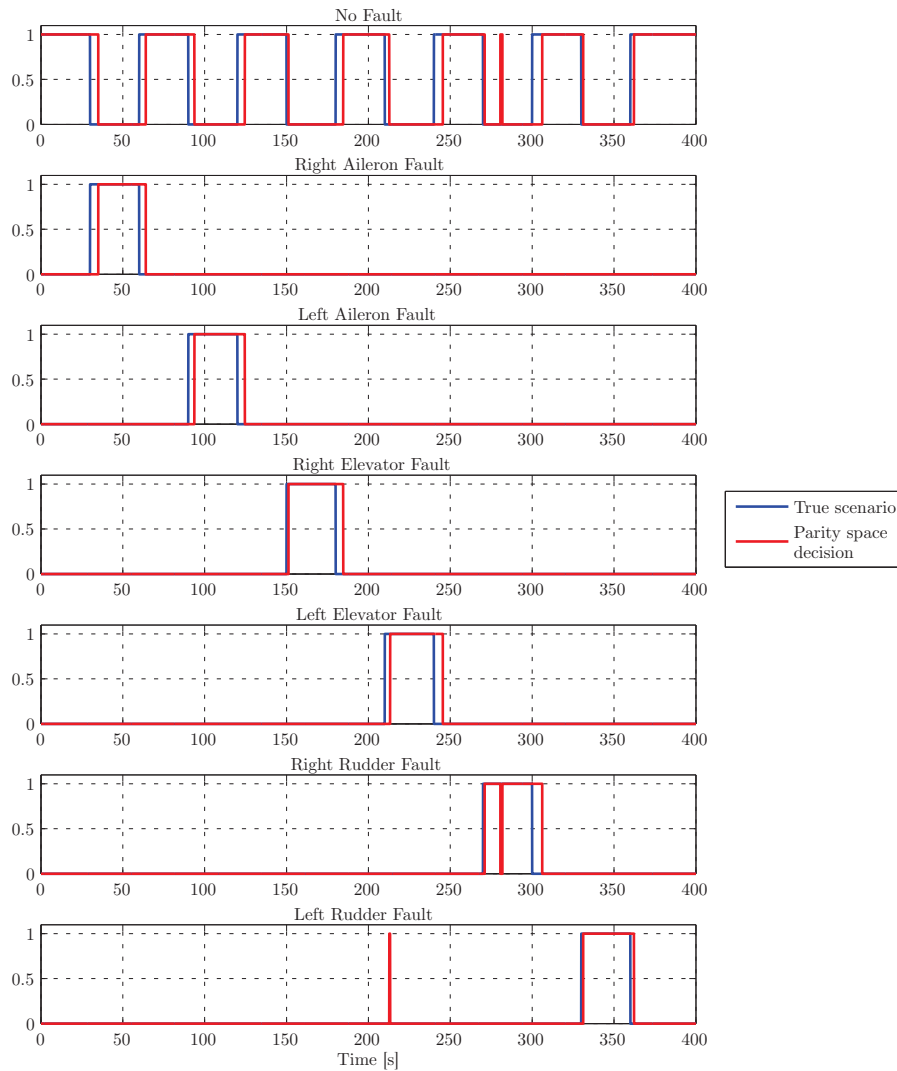


Figure 4.6: Fault decisions for a randomly generated flight mission.

The randomly generated flight mission creates a substantial amount of actuator excitation. As can be seen in figure 4.6 the FDI process performance is acceptable. The anomalies in

the results are removed within one second and all the faults are isolated within two to five seconds. All faults are correctly declared removed after seven seconds.

4.6.5 Simulation Results for a Randomly Generated Flight Mission, but the Actuators Fail with a Locked-in-Place Fault of 2.5°

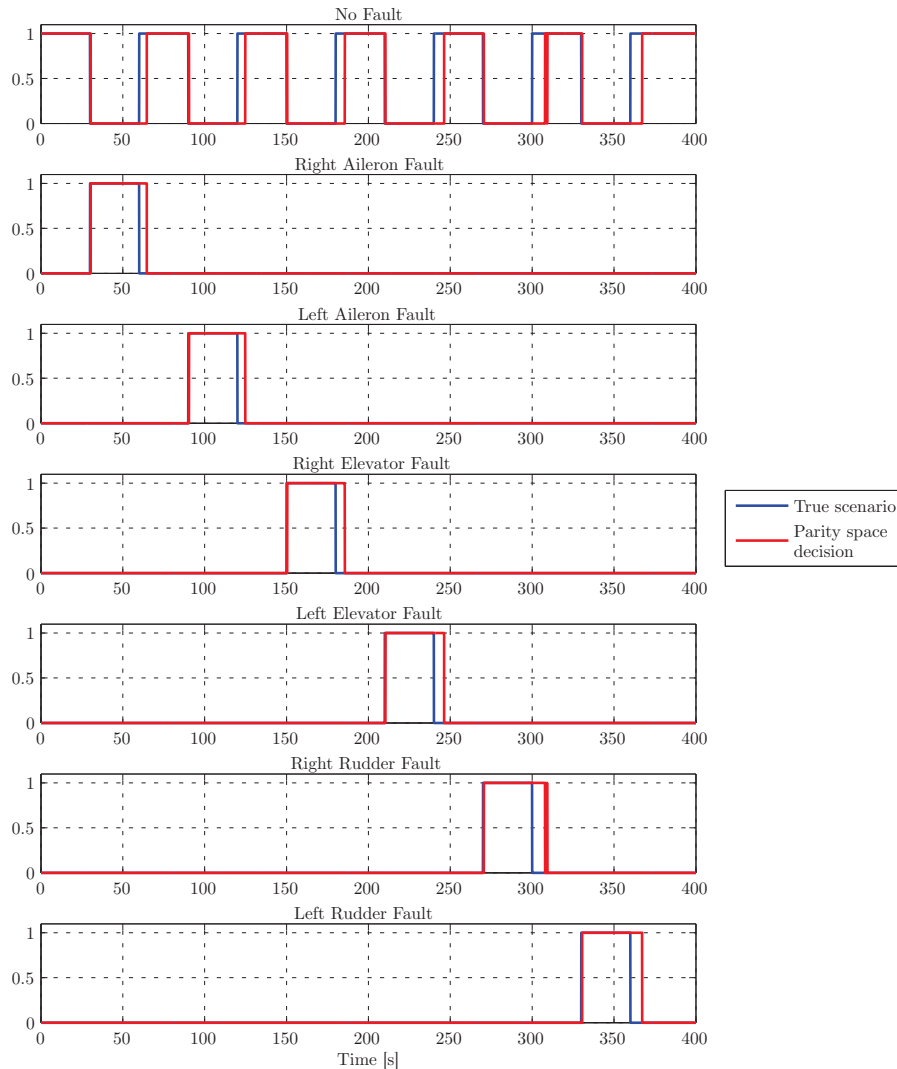


Figure 4.7: Fault decisions for a randomly generated flight mission where the actuators fail with a locked-in-place fault of 2.5° .

A 2.5° locked-in-place fault is much larger than the minimum 1° amplitude that the FDI process is designed to detect. From figure 4.7 it is evident that the FDI performance increases dramatically as actuator deflection increases and subsequently the parity space residuals increase. All the faults are detected within one second and all faults declared removed within seven seconds.

The actuator deflection estimation for the parity space based approach for FDI is shown in figure 4.8. In the figure the greyed out portions of the graphs are not sent to the control re-allocation system. However, when a fault occurs, the estimated deflection of the actuator is sent to the re-allocation process, which is indicated by the non-greyed out portions of figure 4.8.

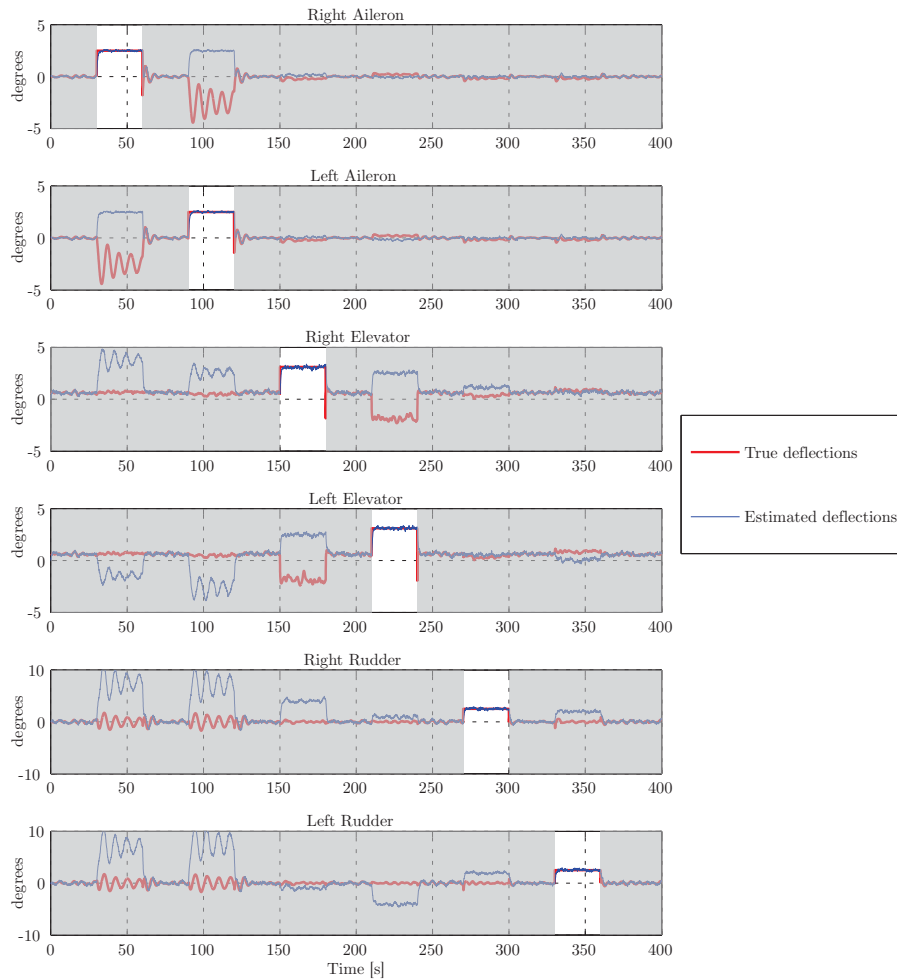


Figure 4.8: Actuator deflection estimation for a randomly generated flight mission where the actuators fail with a locked-in-place fault of 2.5° .

In figure 4.8 it can be seen that all the actuator deflections are accurately estimated when that particular actuator is locked-in-place at 2.5° . Here the actuator deflection estimates are incorrect when other faults are active, similar to section 3.4.5. This is attributed to the solution of equation 4.5.4 that consistently calculates an actuator deflection fault that satisfies the observed inputs and outputs of the aircraft. Therefore when a fault occurs, the other actuator estimators will estimate a deflection value for their particular actuator that will result in the same aircraft behaviour that the original fault is causing.

4.7 Fault Detection and Isolation Performance

In the previous section (4.6) the FDI performance for some typical flight situations was demonstrated. In this section the quality of the parity space based approach to FDI will be simulated for a broader arrangement of flight situations in the same manner as was done with regards to the bank of Kalman filters in section 3.5.

The three arrangements will be repeated below:

1. The aerodynamic stability and control derivatives were changed to test for robustness. A constant amount of natural actuator excitation and process noise was present.
2. The process noise was increased from zero to a substantial amount of wind to test for robustness.
3. The actuator excitation was increased from zero to 3° amplitude on all actuators to test for fault sensitivity.

All three arrangements were also tested for detection time.

4.7.1 The Effect of Parameter Changes on FDI Performance

The aerodynamic stability and control derivatives were changed from 90% of their original values to 110% and the FDI performance was measured at intervals between these two extremes. For this arrangement some natural actuator excitation was present, as well as a nominal amount of process noise. The FDI performance is expected to be the greatest at around 100% of the original values, as the parity space FDI was designed with these values in mind.

From figure 4.9 it is clear that the lowest detection time and lowest false alarm rate is around the 100% original aerodynamic values indicating the best FDI performance at this point, as expected. When the aerodynamic derivatives change more than about 8% from their original values, the FDI performance begins to degrade rapidly.

4.7.2 The Effect of Process Noise on FDI Performance

Process noise has two main effects on the performance of an FDI process. The first effect is that the control system induces actuator excitation to reject the disturbances. A larger amount of process noise therefore improves the FDI performance. However, the uncertainty in process noise creates some confusion in the FDI system and too much process noise will degrade the FDI performance.

From figure 4.10 it is evident that an increase in process noise improves the detection time as the actuator excitation increases. The false alarms and the detection times however increase as the process noise increases, degrading the FDI performance as expected.

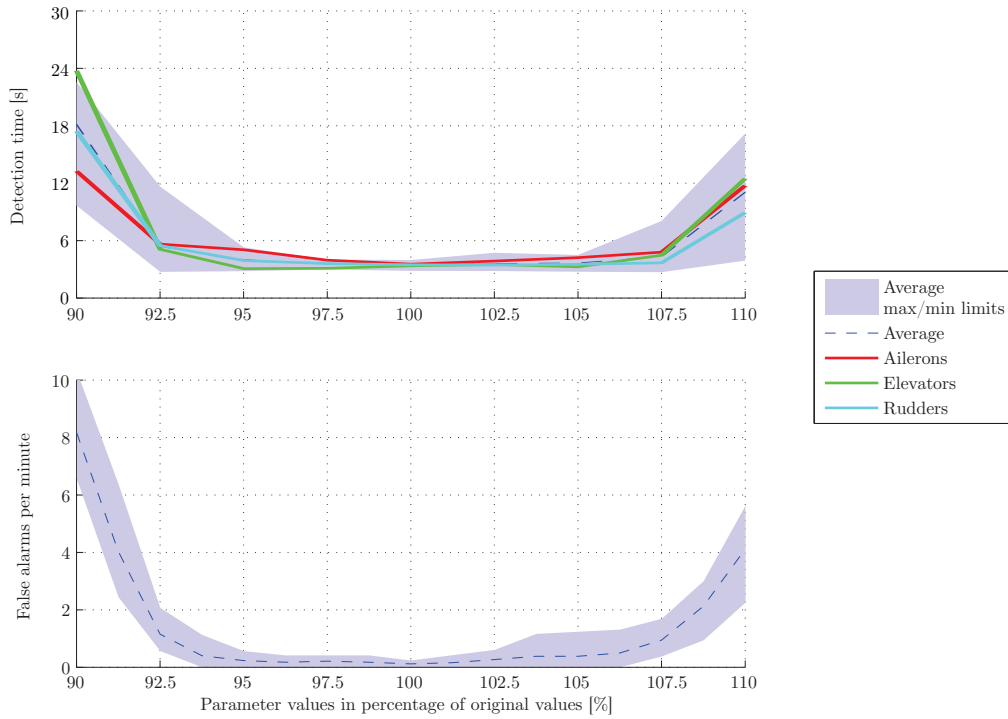


Figure 4.9: The effect of parameter changes on the parity space FDI performance.

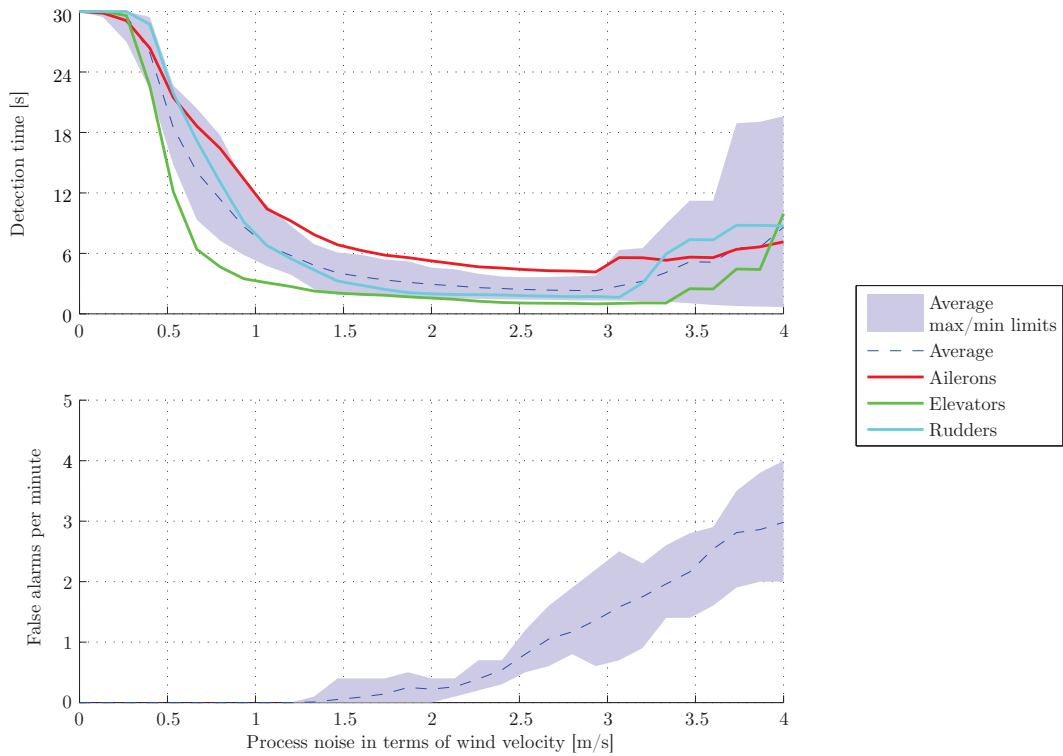


Figure 4.10: The effect of process noise on the parity space FDI performance.

4.7.3 The Effect of Actuator Excitation on FDI Performance

Actuator excitation should have a positive effect on FDI performance, as discussed in section 3.3.1. Note that in figure 4.11 the effect of larger disturbance input matrices (representing more wind) on the design of the parity space FDI is shown. The broken lines represent average detection times and false alarm rates of the parity space FDI using different disturbance input matrices for the design process. The solid lines represent the detection times and false alarms for only the simulations using the nominal wind velocity of 2 m/s.

The effect of using larger values for expected wind is that the fault sensitivity and false alarms decrease while the detection time increases.

From figure 4.11 it is seen that the aileron fault detection time decrease at lower actuator excitation than the elevators. This implies that aileron faults are more easily detected than elevator faults. The effectiveness of the parity space FDI to detect a rudder fault is similar to that of detecting an elevator fault.

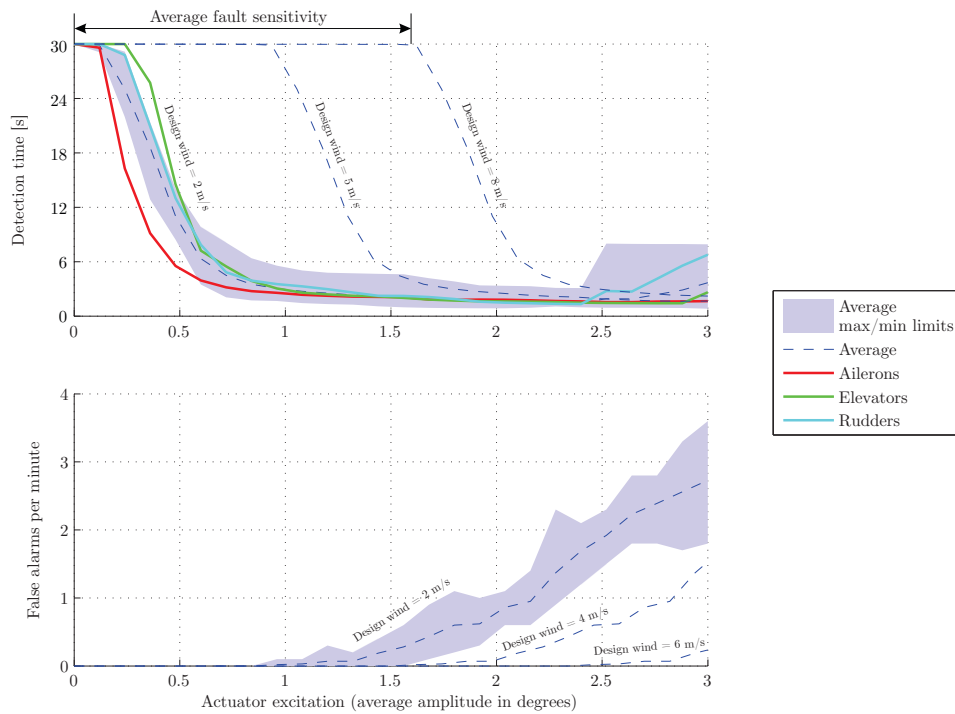


Figure 4.11: The effect of actuator excitation on the parity space FDI performance.

In figure 4.11 it can clearly be seen that the average fault that is not detected becomes larger (decreased fault sensitivity), as the design wind velocity increases. Another effect of increasing the process noise used in the design procedure is the decrease in false alarms.

In figure 4.11 it can be seen that the performance of the FDI increases significantly with actuator excitation. The FDI performance flattens out at 1° actuator amplitude at about 4 seconds detection time. However, with too much actuator excitation the FDI performance starts to degrade. This is due to the fact that as the actuator excitation becomes larger,

the aircraft tends to fly outside the trim conditions where non-linearities become significant. The parity space approach is designed on an aircraft model that was linearised around the trim conditions. FDI performance degradation is inevitable at large actuator excitations as the non-linearities at large flight manoeuvres confuse the system.

Chapter 5

Flight Tests

Flight tests are an integral part of testing and understanding the theoretical work done as part of this research. Two flight tests were conducted to test the performance of the two FDI methods developed in this study, similar to the simulations run in section 3.4 and section 4.6. The first test was to fail different actuators with a 0° locked-in-place fault. The second test was to fail different actuators with a 2.5° locked-in-place fault.

5.1 Physical Aircraft

The Meraka Modular UAV, which is shown in figure 5.1, is the aircraft on which the flight tests were conducted. The mathematics regarding the dynamics of the aircraft were explained in chapter 2, and both the bank of Kalman filters and parity space FDI methods were developed for use on the Meraka Modular UAV.



Figure 5.1: The Meraka Modular UAV.

The outcomes of the flight tests are dependent on the observable effect of the actuators on the aircraft, quantified by the control derivatives. The use of AVL in computing the control derivatives is only an approximation. Some expected behaviour however can be deduced from investigating the geometry of the actuators on the actual aircraft.

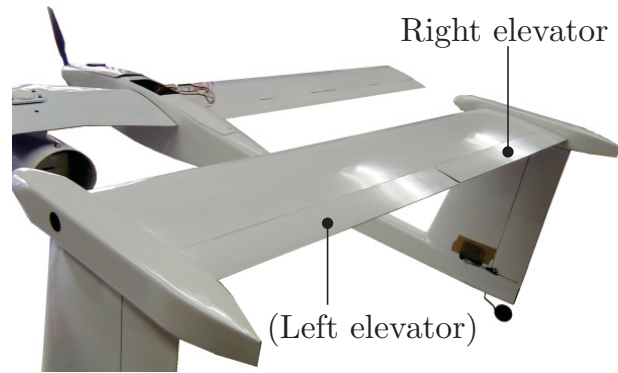


Figure 5.2: Physical right elevator at -2.5° deflection.

The elevators of the Meraka Modular UAV, shown in figure 5.2, are seen to cover small areas relative to the area of the tailplane, but their moment arms around the y_b -axis are large. It is therefore expected that an elevator fault is mainly detectable through deviations in Q (angular rate around the y_b -axis). The problem is however that the elevators has a small moment arm around the x_b . The FDI uses the effect of the actuators around these secondary moment arms, to discern between a left and right actuator fault, not only for the elevator, but also for the rudders and ailerons. It is thus expected that discerning between the left and right elevator will be difficult.

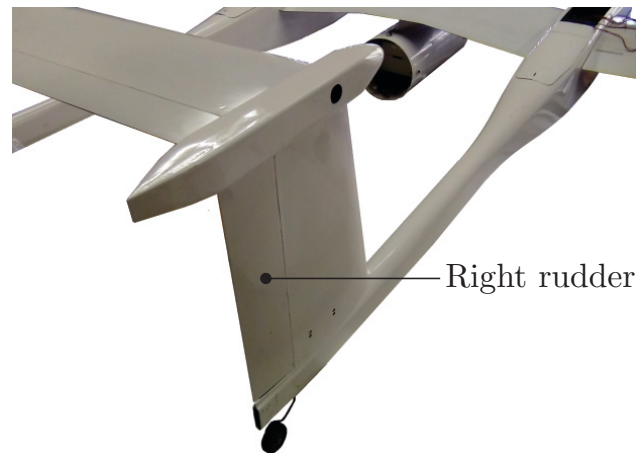


Figure 5.3: Physical right rudder at $+2.5^\circ$ deflection.

The right rudder is shown in figure 5.3 and it is seen to cover a small area relative to the horizontal tail structure, but it has a large moment arm around the z_b -axis indicating that a rudder fault is mainly detected by deviations in R . The rudders however have a small moment arm around the x_b -axis. The moment of inertia is also greatest around the z_b -axis (see appendix A), which further reduces the effect of rudders on the dynamics of the aircraft. It is therefore expected that detecting a rudder fault will be difficult in comparison with an elevator or aileron fault. This phenomenon was also discovered through the development of both FDI methods.

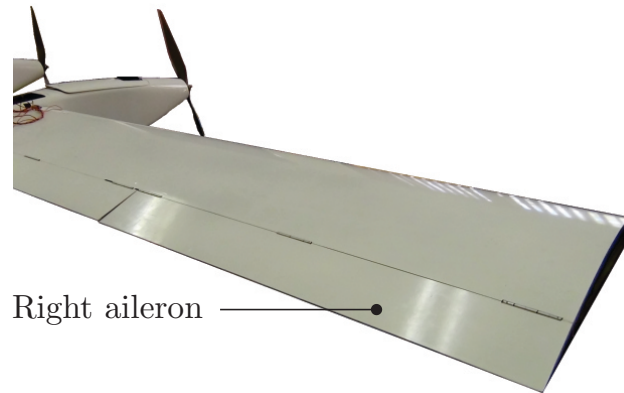


Figure 5.4: Physical right aileron at $+2.5^\circ$ deflection.

The right aileron is shown in figure 5.4 and it has a large moment arm around the x_b -axis and less so around the y_b -axis of the aircraft. Aileron faults are therefore expected to be detected primarily by deviations in P . The aileron also covers a large area relative to the elevators and rudders. It is thus expected that detecting an aileron fault would be easier than detecting an elevator or rudder fault.

5.2 Details of the Flight Tests

The flight tests were conducted at the Helderberg Radio Flyers Club in the Western Cape (South Africa). A flight plan document was compiled beforehand and reviewed with all parties involved. The flight plan can be found in appendix E.

The flight tests were conducted to obtain data to be used by the two FDI methods developed in the study. It was therefore necessary to deliberately fail the actuators at different times and then to remove the fault after a set amount of time, similar to the simulations run in section 3.4 and section 4.6. The sensors on board the aircraft then recorded the data as a fault occurred. The faults were induced deliberately by sending a signal from the ground station to the aircraft, giving specific details of the type of fault: which actuator to fail and the duration of the fault.

The first test was to fly the aircraft and induce 0° locked-in-place faults (from trim) and the second test was to induce 2.5° locked-in-place (from trim) faults.

5.2.1 Wind Conditions

The wind velocity on the test day (19 September 2012) was more than 2 m/s, as shown in figure 5.5, which was much more than was anticipated in the research. In the graph it is seen that the minimum and maximum wind gusts for the flight test periods were 2.3 m/s and 7.7 m/s, respectively.

The flight tests were conducted in such weather conditions due to the fact that the weather in the Western Cape is usually windy between August and March, and also because the

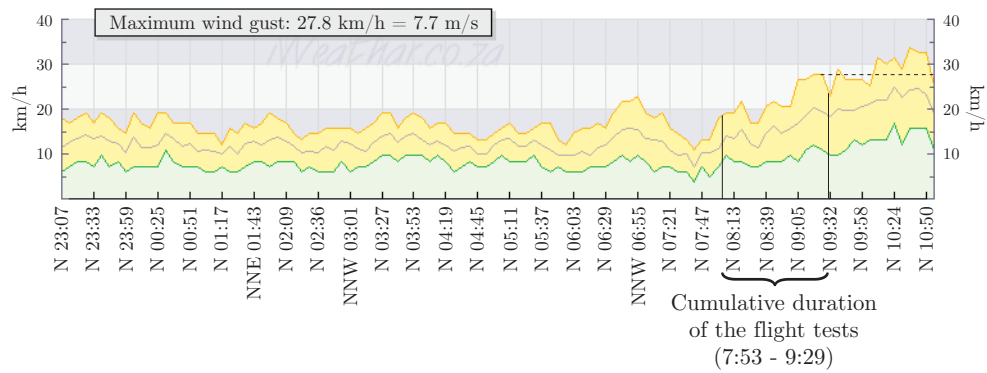


Figure 5.5: Maximum and minimum wind gusts for Helderberg Radio Flyers Club on the morning of 19 September 2012. (<http://iweather.co.za>)

availability of a test venue, flight team, equipment and the Meraka Modular UAV is limited. The windy conditions also allowed testing the FDI systems for robustness.

The measured values for the wind gust velocities found in figure 5.5 were taken on top of the Helderberg Radio Flyers' clubhouse at an altitude of 3 m. In the lower atmosphere wind shear becomes prevalent, causing wind velocities to slow down close to the surface of the earth. From historical data, obtained by previous flight tests done by the ESL, it was found that the wind velocity can increase up to twofold from where the wind velocity is measured by the club to where the aircraft operates at a higher altitude.

The two FDI methods were therefore recalibrated with higher process noise values in the process noise covariance matrix for the Kalman filters and higher values for the healthy covariance matrices in the parity space method. The effect in the parity space method is mainly to change the CUSUM parameters and not so much the optimisation solutions. The higher process noise was set to account for the wind velocity at where the aircraft operates: at 15 m/s. The conservative higher value for the wind velocity was used, because the wind is not the only factor that affects the process noise. Unmodelled dynamics and differences in aircraft parameters all have an effect on how the process noise influences the system.

According to the simulation results of figure 3.12 and figure 4.11, the FDI methods will have less fault sensitivity because of the higher expected (design) wind gust velocity used in the recalibration process.

5.2.2 Flight Trajectory

The aircraft was flown with complete manual pilot control in a race track trajectory as shown in figure 5.6. No automated control loops were introduced during the flight tests.

For one half of the path the aircraft operated without a fault, represented in figure 5.6 as the thin black line. For the other half of the path a fault was induced by the ground station and radio controller, represented in figure 5.6 as the thick red line. This circular trajectory was repeated until all the faults were induced.

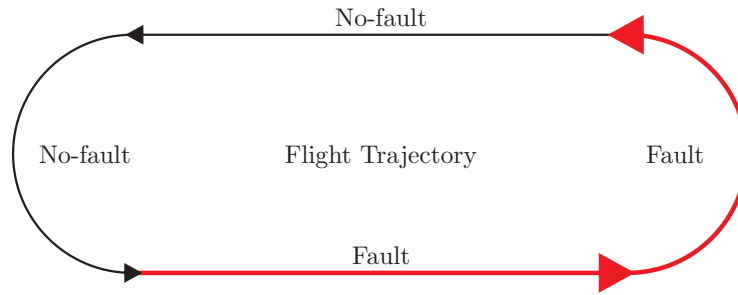


Figure 5.6: Flight trajectory for both flight tests as seen from above.

5.3 Results for the First Flight Test

The first flight was concerned with 0° locked-in-place faults. Table 5.1 summarises the events of the first flight test that was conducted on the 19th of September 2012.

Event start time [s]	Event end time [s]	Event description
35.6	65.6	Fail left aileron at 0° locked-in-place
90.32	123.52	Fail right aileron at 0° locked-in-place
146.84	180.92	Fail left elevator at 0° (from trim) locked-in-place
204.44	236.92	Fail right elevator at 0° (from trim) locked-in-place
261.76	292.12	Fail left rudder at 0° locked-in-place
316.32	347.36	Fail right rudder at 0° locked-in-place

Table 5.1: First test flight event summary.

The fault decisions for the two FDI methods are summarised in figures 5.7 and 5.9 respectively. It is desirable that the line representing the fault decision follows the real fault scenario as closely as possible. The high levels of process noise, as well as unmodelled dynamics and inevitable differences in aircraft parameters, may however affect the outcome in a negative manner.

The actuator deflection estimates are illustrated in figures 5.8 and 5.10 for the two FDI methods. The high wind velocity and differences in aircraft parameters should also adversely affect the actuator deflection estimates in an interesting manner that will be discussed below.

5.3.1 FDI Results Using the Bank of Kalman Filters

In figure 5.7 the fault decisions along with the fault probabilities are shown. It can be seen that aileron faults are detected and discernable as expected. Looking at the probabilities of the faults, some confusion is seen at the onset of an aileron fault as the filters decide if the left or right aileron is at fault. The FDI takes between five and ten seconds to detect that an aileron is at fault.

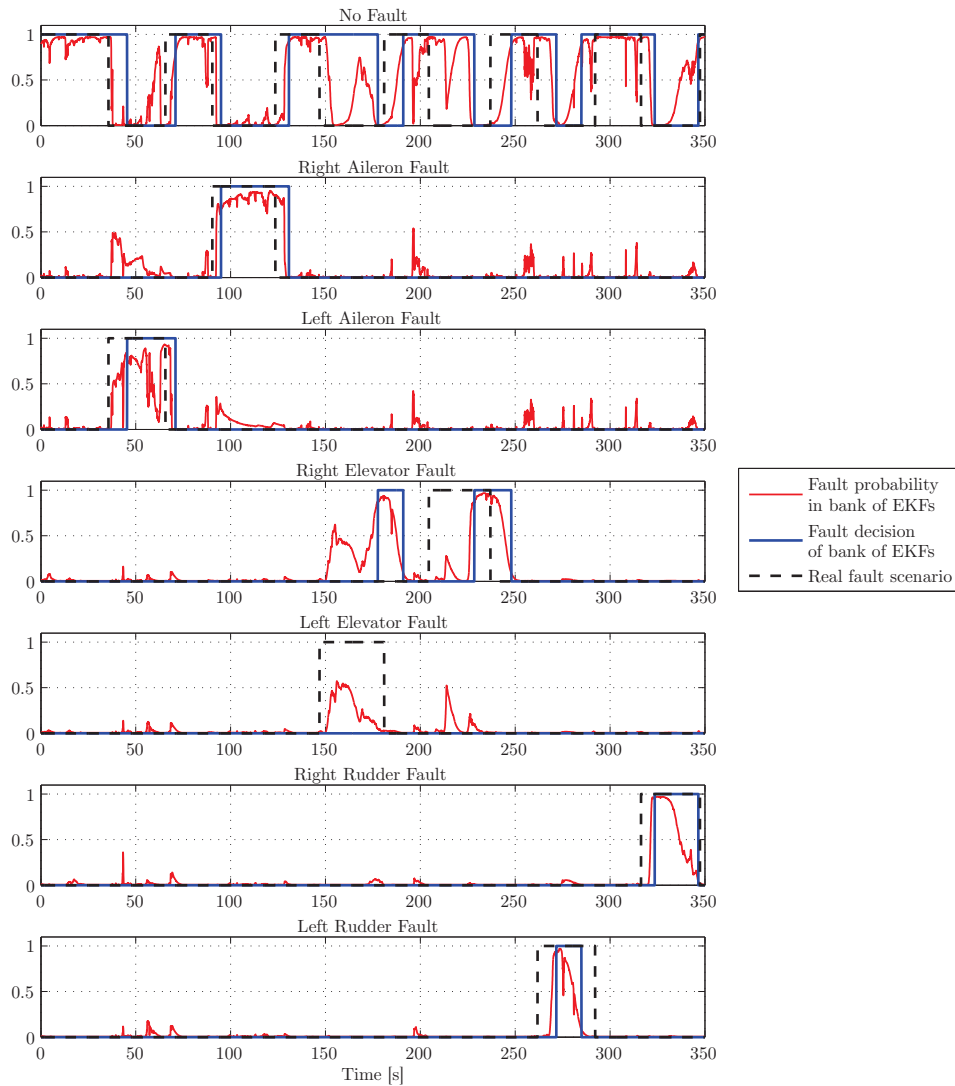


Figure 5.7: Fault decisions using the bank of Kalman filters FDI.

As seen in the fourth and fifth row in figure 5.7, the FDI has difficulty detecting the elevator faults. It also has difficulty deciding if the left or right elevator is at fault, causing a long delay before a fault decision is made. This is precisely what was expected, as was discussed in section 5.1. The FDI takes 25 seconds to correctly detect an elevator fault.

In the two last rows of figure 5.7 the fault decisions regarding the rudder faults are displayed. It is interesting to note that both rudder faults were detected even though it was expected to be difficult. It must be noted however that the rudders are excited at the same time as when the faults occur, as can be seen in figure 5.8's last two rows. The large extra actuator excitation made the rudder faults detectable, as was expected. The FDI takes between seven and ten seconds to detect a rudder fault.

Figure 5.8 displays the actuator deflection estimates as determined by the bank of Kalman filters. The non-greyed out areas represent estimated deflections when a fault occurs.

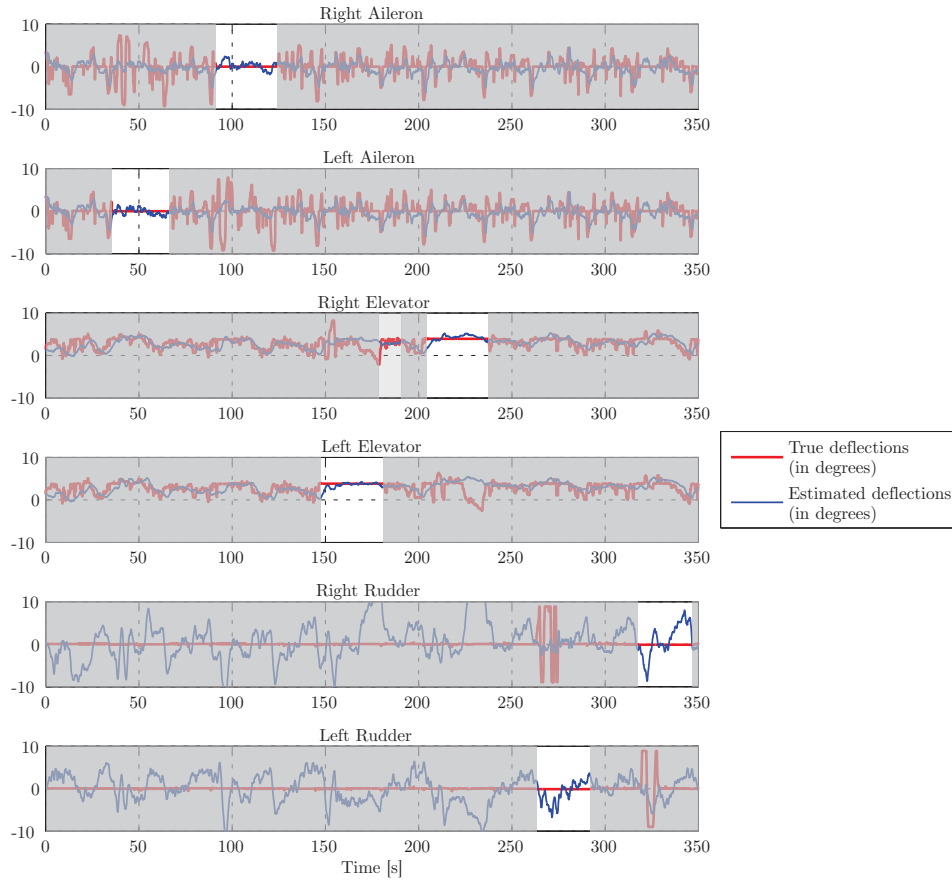


Figure 5.8: Actuator deflection estimates using the bank of Kalman filters FDI.

Note that the actuator deflections are estimated with some error, especially the rudder deflection estimates. The large error in the estimates can be attributed to the fact that the Kalman filters always try and calculate an actuator deflection estimate that will produce the same dynamic effect as that being observed through the sensors. This means that the estimators are trying to quantify the effect of a fault, but also the effect of disturbances, through its estimate. With such large wind gusts present, the estimators are focussing more on determining an actuator deflection that would produce the same wind effect, instead of focussing on the effect of a fault. This will always be the case once the effect of disturbances are greater than the effect of faults.

The light grey area in figure 5.8 represents the right elevator deflection estimates when the FDI incorrectly detected a right elevator fault. It shows that the estimated value for the right elevator will incorrectly be sent to the re-allocation process, but that the estimate is still reasonably correct.

The aileron and elevator deflection estimates resemble the true deflection, once a fault has occurred, within a 2° margin. The rudder estimates on the other hand have about a 10° error margin. This is due to the fact that the control derivatives of a rudder are less than that of the ailerons and elevators, and the moment of inertia is greatest around the z_b -axis (see appendix A). The effect is that the estimator needs to estimate larger values of rudder

deflection to produce the same disturbance effects.

5.3.2 FDI Results Using Parity Space

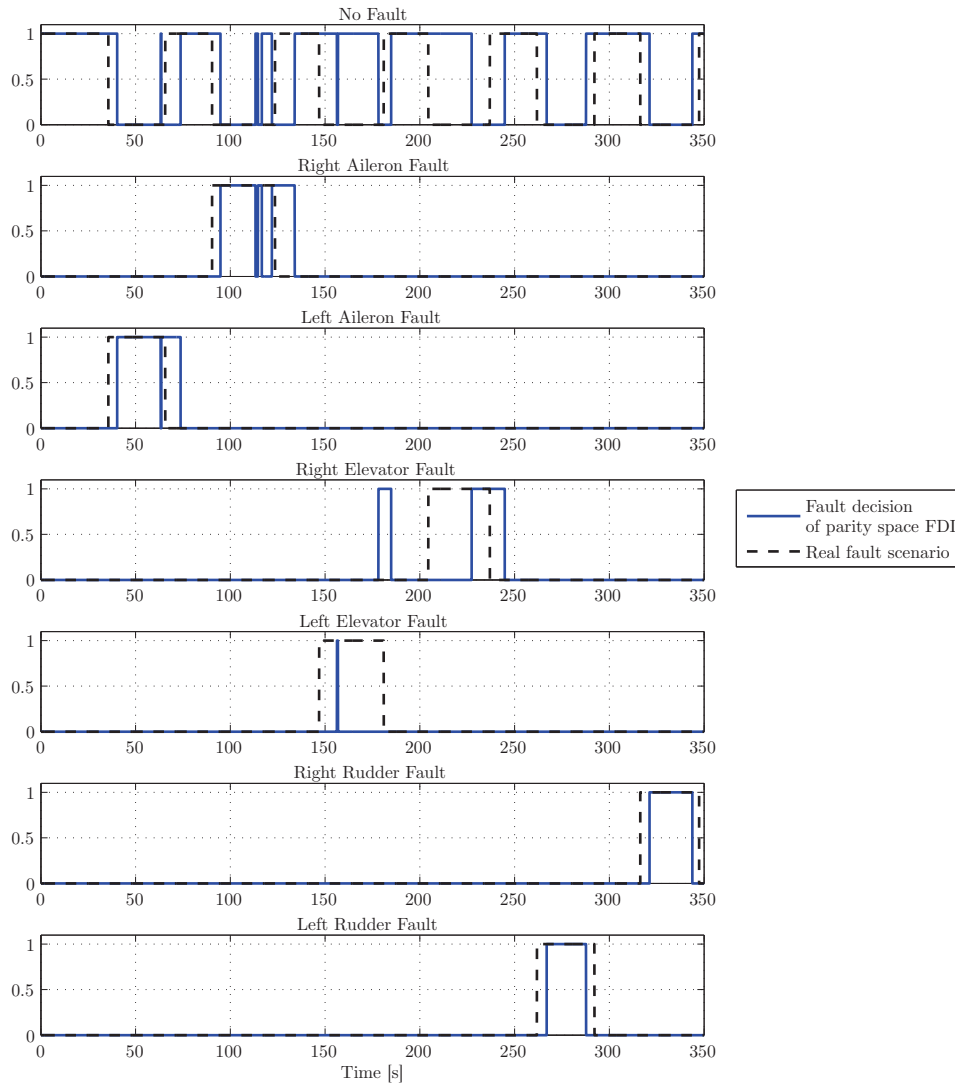


Figure 5.9: Fault decisions using parity space FDI.

Figure 5.9 displays the decisions of the parity space FDI method for the first flight test.

In the second and third rows of figure 5.9, the decisions regarding an aileron fault are shown. It can be seen that the FDI can detect aileron faults within five seconds and can also discern between the left and right aileron.

In the fourth and fifth rows of figure 5.9, the FDI has difficulty detecting elevator faults, as well as discerning between the left and right elevator, as was expected. The FDI takes 23 seconds to correctly detect an elevator fault.

The parity space FDI correctly detects rudder faults in less than five seconds, as can be seen in figure 5.9. Even though the wind disturbance on the aircraft is large and the rudders are difficult to detect, the extra actuator excitation seen in figure 5.10's last two rows empower the FDI to detect the rudder faults.

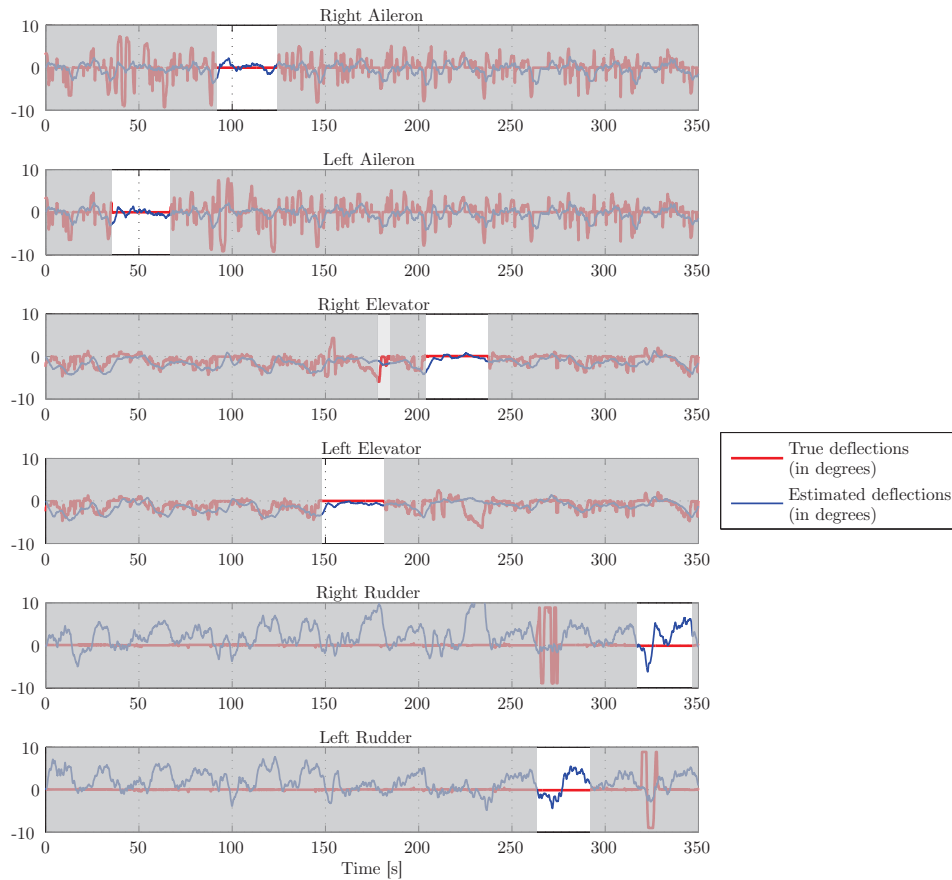


Figure 5.10: Actuator deflection estimates using parity space FDI.

Figure 5.10 summarises the actuator deflection estimates calculated with the parity space method. The non-greyed out areas represent the deflection estimates when the specific actuator fault occurs. The light grey area represents the right elevator deflection estimates when the FDI incorrectly detected a right elevator fault. It shows that the estimated value for the right elevator will incorrectly be sent to the re-allocation process, but that the estimate is still reasonably correct.

In figure 5.10 it is seen that the estimates do not follow the true actuator deflections, especially for the rudder. This is due to the fact that equation 4.5.4 is trying to find the solution to a fault that will create the same effect that the faults and disturbances have on the aircraft. Since the wind disturbances are larger than the effect of an actuator fault, the effect of wind greatly overshadows the effect of faults in the estimate solution.

5.4 Results for the Second Flight Test

The second flight was concerned with 2.5° locked-in-place faults. Table 5.2 summarises the events of the second flight test that was conducted on the 19th of September 2012.

Event start time [s]	Event end time [s]	Event description
28.96	63.4	Fail left aileron at positive 2.5° locked-in-place
87.72	120.70	Fail right aileron at positive 2.5° locked-in-place
145	182.2	Fail left elevator at negative 2.5° (from trim) locked-in-place
204.6	238.7	Fail right elevator at negative 2.5° (from trim) locked-in-place
263.2	289.08	Fail left rudder at positive 2.5° locked-in-place
311.44	339.6	Fail right rudder at positive 2.5° locked-in-place

Table 5.2: Second test flight event summary.

The fault decisions of the bank of Kalman filters FDI and parity space FDI are shown in figure 5.11 and 5.13 respectively. The preferred behaviour of the decisions is to follow the real fault scenario (broken line) as closely as possible.

The actuator deflection estimates for the two FDI processes are displayed in figure 5.12 and 5.14. The high wind velocities should adversely affect the correctness of estimating the actuator deflections.

The unavoidable differences in aircraft parameters between the real aircraft and the mathematical model developed in this research should adversely impact the performance of the FDIs.

5.4.1 FDI Results Using the Bank of Kalman Filters

Figure 5.11 shows the fault decisions that the bank of Kalman filters made with regard to 2.5° locked-in-place faults.

The second and third rows in figure 5.11 clearly indicate that an aileron fault can be detected and that the left and right fault can be discerned correctly. The aileron faults were detected in under seven seconds.

The fourth and fifth rows in figure 5.11 display the fault decision regarding the elevator faults. It is seen that an elevator fault is detected in under ten seconds, but that the system incorrectly diagnosed the fault at 145s as a right elevator fault instead of a left elevator fault. This is what was expected, as was discussed in section 5.1.

In the last two rows of figure 5.11 it can be seen that no rudder faults are detected. This is due to the fact that 2.5° rudder deflection is too little actuator excitation for the FDI to

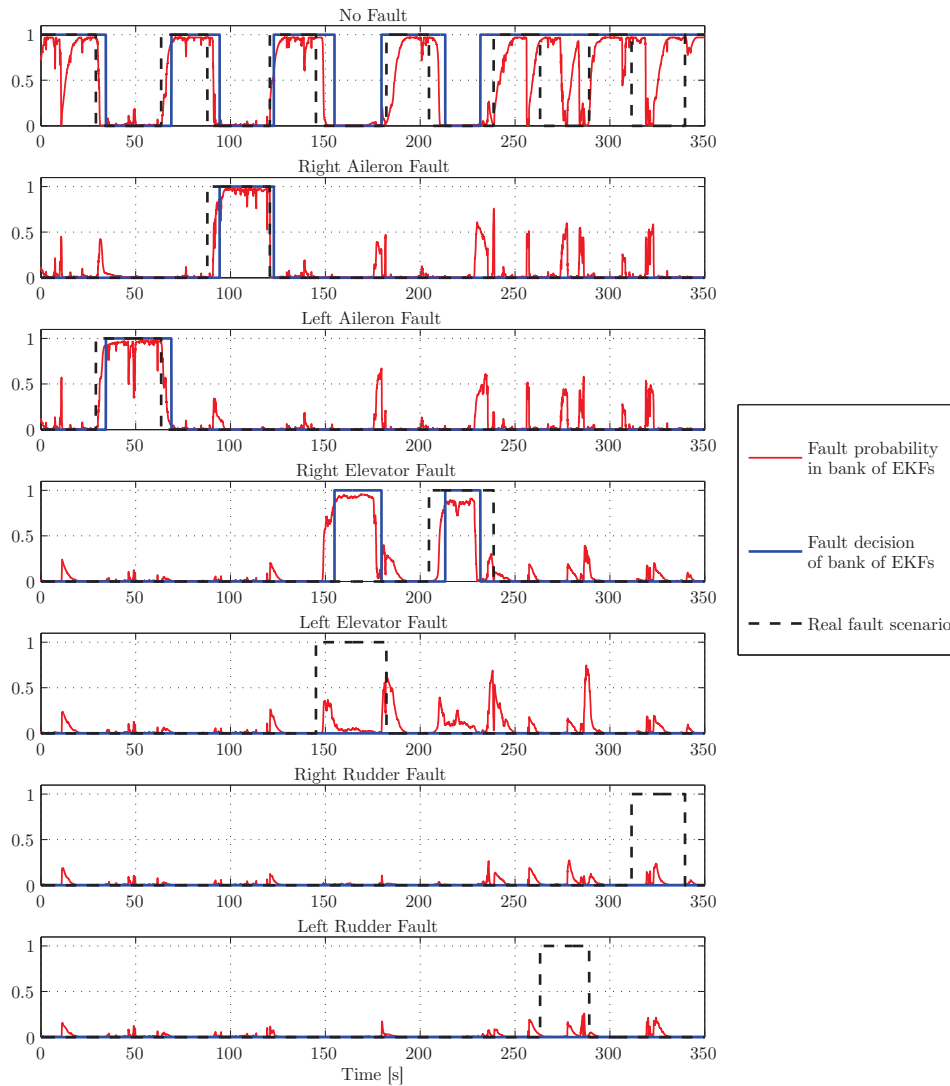


Figure 5.11: Fault decisions using the bank of Kalman filters FDI.

detect. Recall that the bank of Kalman filters were recalibrated with a higher process noise covariance matrix that decreased the fault sensitivity of the FDI system.

In figure 5.12 the estimated actuator deflections using the bank of Kalman filters are shown. The desired behaviour of the estimators should be to correctly estimate the actuator deflections when a fault has occurred (the non-greyed out areas). The light grey area represents the right elevator deflection estimates when the FDI incorrectly detected a right elevator fault. It shows that the estimated value for the right elevator will incorrectly be sent to the re-allocation process and that the deflection estimate is incorrect. The estimate however resembles the faulty left elevator deflection.

It is seen in figure 5.12 that the actuator deflections are estimated with some error. The aileron and elevator deflections are estimated within a 2° margin and the rudder estimates are estimated within a 10° margin.

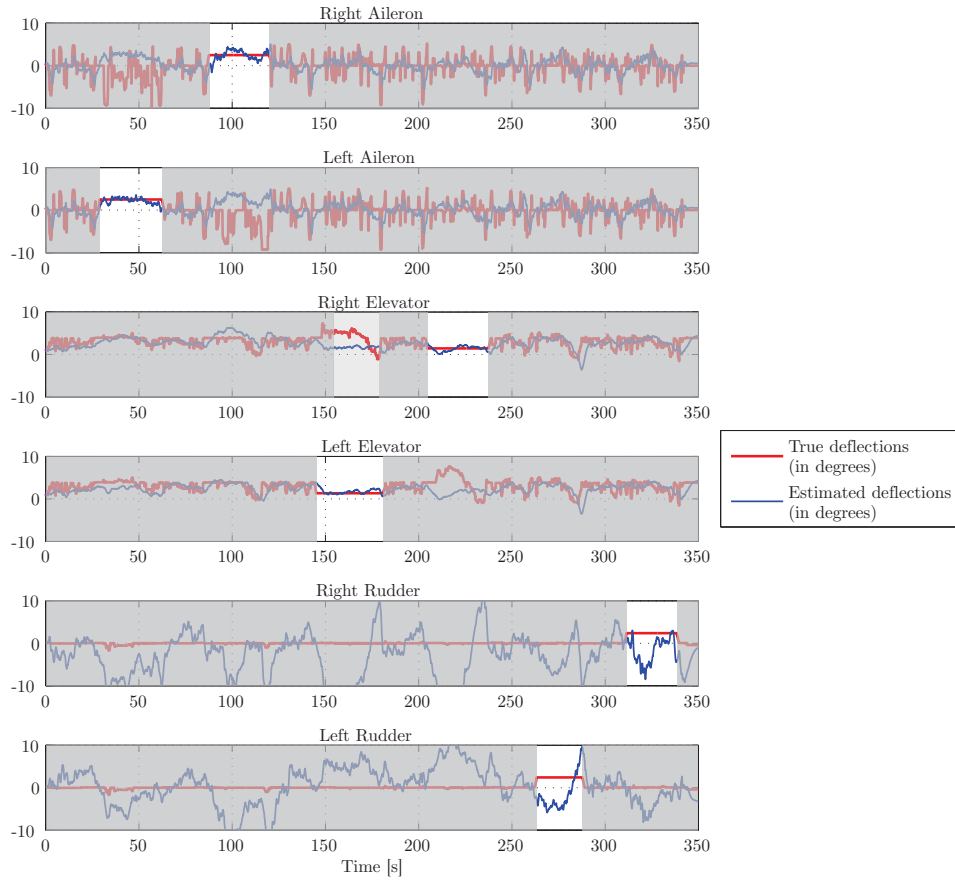


Figure 5.12: Actuator deflection estimates using the bank of Kalman filters FDI.

Note however that the estimation follows the low frequency movement of the true actuator deflections to some extent. The effect of higher wind velocity is that it becomes more prevalent than the effect of the fault. This unwanted effect of the wind and other disturbances causes the filters to estimate misleading deflections since they are a combination of the fault and disturbances effects.

5.4.2 FDI Results Using Parity Space

Figure 5.13 illustrates the decisions made by the parity space FDI regarding the fault scenarios of the second flight test.

In figure 5.13's second and third rows it is seen that the FDI can accurately detect aileron faults within four seconds. This was the expected behaviour of the FDI.

The elevator fault decisions, displayed in the fourth and fifth rows of figure 5.13, demonstrate that an elevator fault is detected within seven seconds, but that the FDI cannot distinguish between the left and right elevator. This is in accordance with what was discussed in section 5.1.

No rudder faults are detected in figure 5.13, because the recalibration of the FDI using larger values for the disturbance input matrix. This caused the fault sensitivity to decrease and therefore the 2.5° actuator excitation was insufficient to detect the rudder faults.

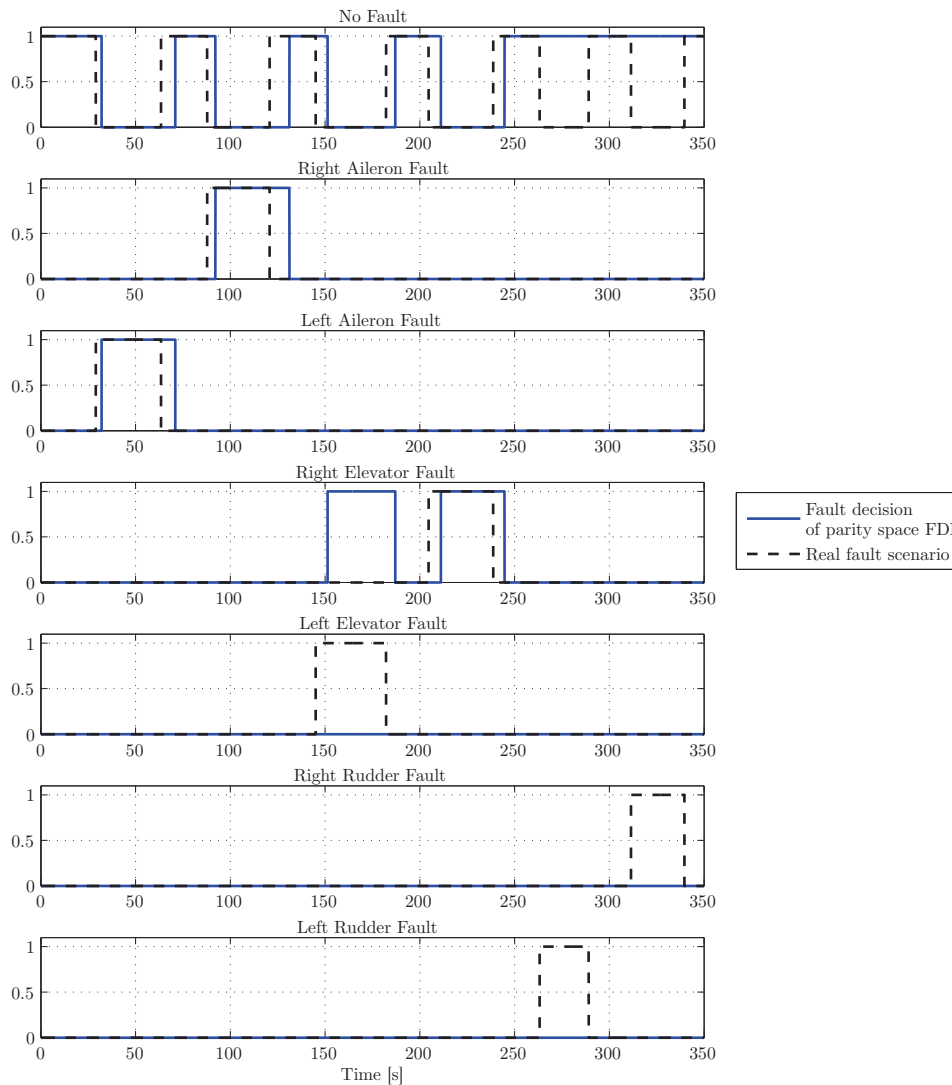


Figure 5.13: Fault decisions using parity space FDI.

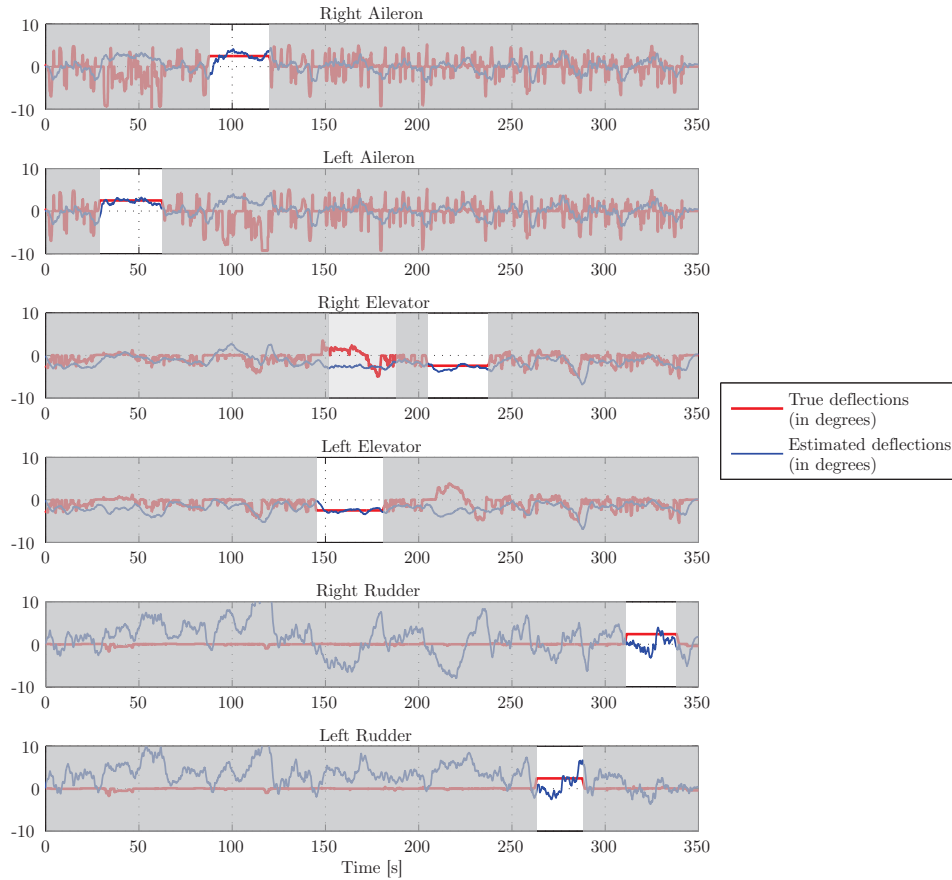


Figure 5.14: Actuator deflection estimates using parity space FDI.

Figure 5.14 displays the actuator deflection estimates determined by the parity space equations 4.5.4 and 4.5.5. The non-greyed out areas represent where a fault has occurred and where the estimators should estimate the same value as the true actuator deflection. The light grey area represents the right elevator deflection estimates when the FDI incorrectly detected a right elevator fault. It shows that the estimated value for the right elevator will incorrectly be sent to the re-allocation process and that the deflection estimate is incorrect. The estimate however resembles the faulty left actuator deflection.

In figure 5.14 we see that the aileron and elevator estimators follow the low frequency signal of the true deflections with a margin of error of about 2° . The rudder deflection estimates on the other hand have an error margin of 10° . The low frequency behaviour originates from inherent low-pass filtering present in the parity space FDI. The error margin quantifies the effect that wind has on the aircraft above the effect of an actual fault. Therefore higher winds would adversely affect the actuator deflection estimates in the same manner as described in section 5.3.

Chapter 6

Comparison of the Two Fault Detection and Isolation Methods

6.1 Simulation Results

Note that the FDI system used to obtain the simulation results shown in this section was designed using an expected (design) wind velocity of 2 m/s. The simulation results obtained in section 3.5.1 for the bank of Kalman filters and section 4.7 for the parity space approach are compared in this section. The comparison will focus on detection times and false alarms of the average values illustrated in figures 3.10 to 3.12 and 4.9 to 4.11.

6.1.1 FDI Performance Comparison in Terms of Parameter Change

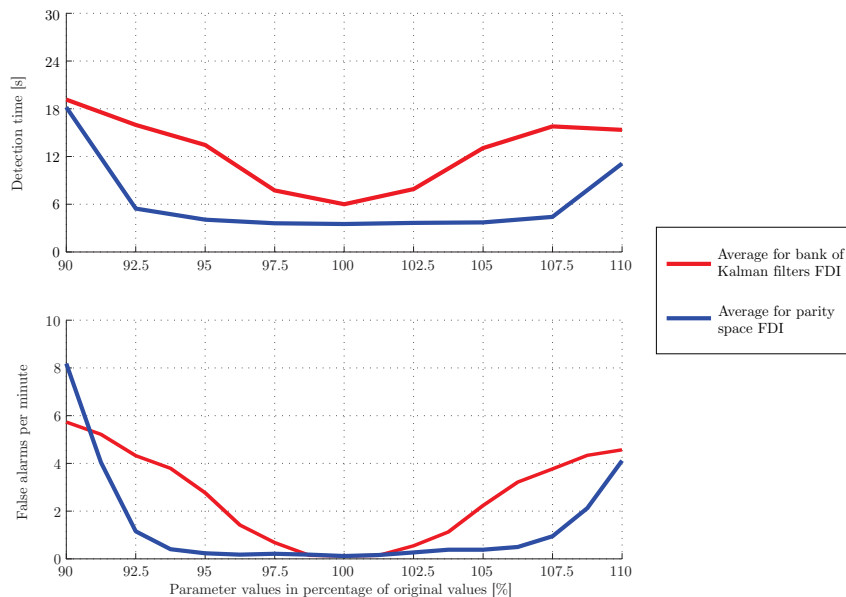


Figure 6.1: FDI performance of the two FDI methods in terms of changing parameter values.

In figure 6.1 the average performance of the bank of Kalman filters and the parity space FDI is displayed. The figure indicates that the parity space FDI can tolerate larger changes in the aircraft's parameters.

Recall from equations 3.2.6 to 3.2.10 that the Kalman gains are calculated with the statistical information of the measurement and process noise. The variance of the disturbances are therefore the determining factor for the dynamics of the bank of Kalman filters. The bank of Kalman filters are also dependent on the system states.

On the other hand the parity space design procedure requires an optimisation process that is optimised specifically for actuator FDI. The parity space method also requires the null matrix of the observability matrix that decreases the sensitivity of the states to the parity relations.

The parity space is optimised specifically for FDI and the insensitivity towards disturbances, and is independent of system states. It therefore gives it more robustness in terms of parameter changes, as can be seen in figure 6.1.

6.1.2 FDI Performance Comparison in Terms of Process Noise

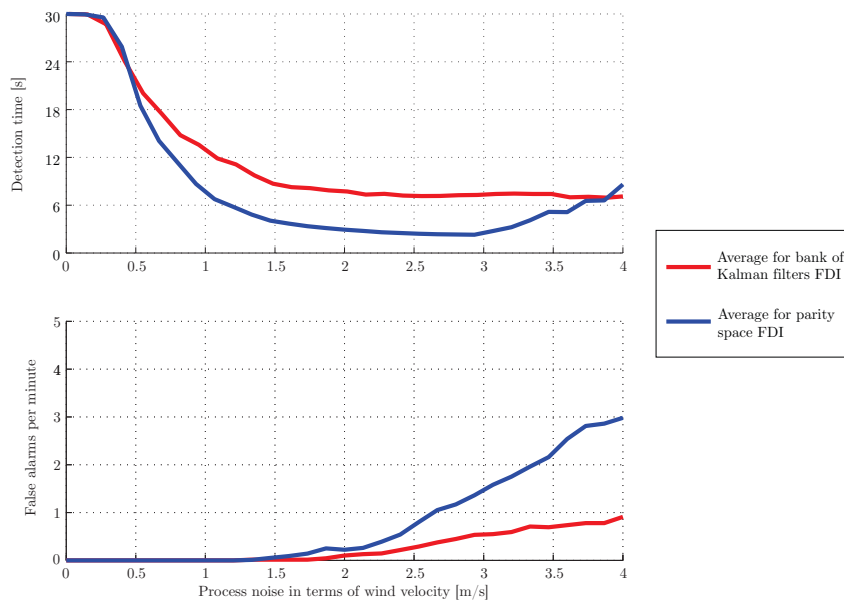


Figure 6.2: FDI performance of the two FDI methods in terms of process noise.

Figure 6.2 demonstrates the effect of increased induced process noise on the performance of both the bank of Kalman filters FDI and the parity space FDI. Recall that additional process noise induces extra actuator excitation, which assists the FDI process.

In figure 6.2 it can be seen that the detection times of the parity space method deliver superior results as opposed to that of the bank of Kalman filters at intermediate amounts of wind. The increased effectiveness of the parity space at moderate amounts of process

noise can be attributed to the same robustness properties as were discussed in section 6.1.1, where the focus of the parity space FDI design procedure is to optimise specifically for FDI.

At high process noise however, the detection times of the parity space FDI start to increase to levels above that of the bank of Kalman filters. This is due to the fact that at high process noise levels the aircraft tends to fly outside the linear region of the flight envelope. The extended Kalman filters in the bank of Kalman filters are designed to tolerate the non-linearities in these regions, whereas the parity space FDI is not. Consequently the parity space FDI's performance degrades significantly at high values of process noise.

The false alarm rates for both FDI methods increase as the amount of process noise increases. The process noise does induce extra actuator excitation, which assists in the FDI process, but the process noise also affects the aircraft in unpredictable ways. At higher values of the process noise the uncertainty of the disturbance creates a higher number of false alarms. This is true for both FDI methods.

Figure 6.2 shows that in general the parity space has shorter detection times but more false alarms than the bank of Kalman filters. From this it can be seen that the sensitivity of the parity space to faults is higher. There is thus a trade-off between the desired detection time and number of false alarms.

6.1.3 FDI Performance Comparison in Terms of Actuator Excitation

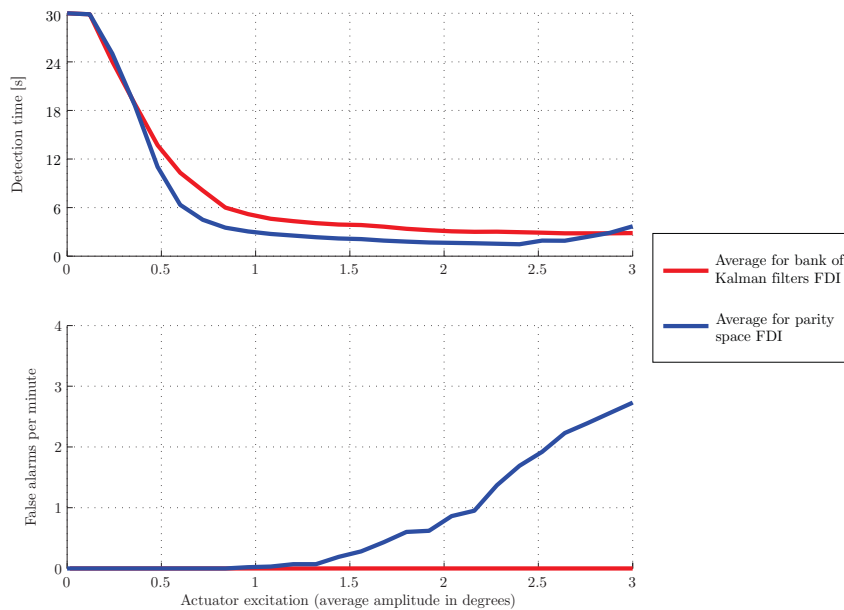


Figure 6.3: FDI performance of the two FDI methods in terms of actuator excitation.

In figure 6.3 the effect of increased actuator excitation is illustrated on the FDI performance of the two FDI methods developed in this research, where the detection times are very similar. However, at high amounts of actuator excitation the parity space method's detection time and false alarm rate start to increase. At high levels of actuator excitation, the aircraft

tends to fly in a more non-linear region of its flight envelope. The parity space is a linear FDI process, whereas the extended Kalman filters were designed to handle the non-linearities in these non-linear regions. The bank Kalman filters show superior FDI performance in terms of false alarm rates.

6.2 Flight Tests Results

The results of the flight tests are shown graphically in figures 5.7 to 5.14. Tables 6.1 and 6.2 summarise the FDI performance measures of the flight tests in terms of detection time and incorrect detections. In each column two values are given, separated by a slash, where the left value indicates the detection time and the right value indicates the number of incorrect detections for the specific actuator. The number of false alarms are not shown as no false alarms were detected. Note that a false alarm represents a detection when no fault is present, whereas a incorrect detection indicates a fault that occurred, but which was isolated incorrectly.

Recall that the two FDI methods were recalibrated with a higher design wind velocity. It is therefore expected that the fault sensitivity of the FDI processes will decrease as discussed in chapter 5.

Performance measure	Actuator	Bank of Kalman filters	Parity space
Detection time [s] / # of incorrect detections	Right aileron	4.6 / 0	4.44 / 0
	Left aileron	9.8 / 0	4.64 / 0
	Right elevator	24 / 1	22.88 / 1
	Left elevator	- / 0	9.4 / 0
	Right rudder	7.2 / 0	4.88 / 0
	Left rudder	9.92 / 0	5.16 / 0

Table 6.1: FDI performance of first flight test.

From table 6.1 it is evident that the detection times for the parity space FDI method is less than the detection times in the bank of Kalman filters FDI. This corresponds well with the simulation results summarised in figures 6.2 and 6.3.

In figure 5.9's second and third rows it can be seen that the aileron faults are detected within five seconds, but that the faults are missed for some instances when the fault is active. This decrease the quality of the detection, but is still adequate.

Table 6.1 shows that the incorrect detection is triggered when the left elevator fails. Both the bank of Kalman filters and the parity space FDI incorrectly detected a right aileron fault. The inability of both FDI methods to correctly detect a left elevator fault is attributed to the fact that although an elevator fault is detectable, the FDI methods have difficulty distinguishing between the left and right elevator pair, as discussed in section 5.1. The

parity space method, however, does detect a left elevator fault for a short period of time, whereas the bank of Kalman filters missed the left elevator fault completely.

From figures 5.7, 5.11, 5.9 and 5.13 it is noted that the time it takes the parity space method to detect that a fault is removed is longer than the time it takes the bank of Kalman filters. This is due to the fact that the bank of Kalman filters have a filter specially designed for the no-fault case, whereas the parity space FDI does not produce a residual that is optimised for a no-fault scenario. The CUSUM procedure in the parity space must therefore “leak” until the fault detection is removed, which takes a longer than in the bank of Kalman filters. According to [8] the time it takes to detect that a fault has been removed is not an important FDI performance parameter.

Performance measure	Actuator	Bank of Kalman filters	Parity space
Detection time [s] / # of incorrect detections	Right aileron	6.38 / 0	4.36 / 0
	Left aileron	5.28 / 0	3.04 / 0
	Right elevator	8.6 / 1	6.48 / 1
	Left elevator	- / 0	- / 0
	Right rudder	- / 0	- / 0
	Left rudder	- / 0	- / 0

Table 6.2: FDI performance of second flight test.

Table 6.2 summarises the fault performance measurements obtained by the two FDI methods on the second flight test. Note again that the results here were obtained by designing the FDIs with a higher design wind velocity and therefore it should be expected that the fault sensitivity of both FDIs should decrease.

In table 6.2 only the aileron faults and a right elevator fault were detected. Of these three faults, the bank of Kalman filters took longer to detect a fault than the parity space FDI. This corresponds to the graphs in figures 6.2 and 6.3. The parity space method and bank of Kalman filters however made an incorrect elevator detection. This strengthens the belief that it is difficult to isolate an elevator fault on the Meraka Modular UAV, even though the presence of an elevator fault is detected. The left elevator fault was not detected due to the difficulty with which the FDI methods discern between right and left elevator faults, as was discussed previously.

The rudder faults were undetected, as seen in table 6.2, because 2.5° was too small an amount of actuator excitation to assist the FDI systems in detecting these faults. This is what was expected, since the recalibrated FDI systems should cause a decreased FDI sensitivity to faults.

6.3 Comparison to Other Literature

In [2] a bank of extended Kalman filters was implemented to detect actuator faults for left and right ailerons, left and right elevators and one rudder. The actuators were failed at near trim conditions in a MATLAB® / Simulink® simulation with a non-linear autopilot which regulated the velocity, altitude and the attitude of the aircraft. Only the detection times were given and table 6.3 summarises the FDI performance of the simulated system.

Actuator	Detection Time [s]
Right Aileron	24
Left Aileron	20
Right Elevator	11
Left Elevator	18
Rudder	1

Table 6.3: FDI performance on the simulations in [2].

It must be noted that the simulation done in [2] was with low process noise that induced some actuator excitation. The simulations in this thesis that represent the results in table 6.3 the closest, is between mission 1 and mission 2 of sections 3.4 and 4.6.

The results in table 6.3 indicate that the FDI methods developed in this research perform relatively well, especially in terms of the aileron faults, which are detected faster than the 24 seconds in [2]. One observation that can be made is that the rudder fault is detected within one second. The speedy response to a rudder fault in table 6.3 is due to the fact that only one rudder is present. The FDI system therefore does not have to waste time and effort discerning between the left and right rudder.

6.4 Noteworthy Differences

The differences between the bank of Kalman filters and the parity space FDI stem from the way in which their residuals are generated and how their decision processes are set up.

The bank of Kalman filters use several different extended Kalman filters to estimate the actuator deflections and then predict the observed sensor values. The non-linear extended Kalman filters allow the FDI to be more robust in terms of larger aircraft manoeuvres. The Kalman filters are however susceptible to instability if it is not design carefully.

The parity space on the other hand is an FDI process designed around a certain working point, usually the trim condition of the aircraft. The parity space method's performance therefore degrades once the aircraft flies outside the sufficiently linear region of the flight envelope. The parity space is however a stable residual generator if the linearised mathematical state space representation of the system is stable.

The residuals created by the bank of Kalman filters represent the relative error that each filter within has with regard to the actual state of the system. The filter with the smallest

residual therefore represents the filter that is most likely to represent the correct fault scenario. The parity space approach on the other hand is optimised so that each fault creates a distinct effect on certain residuals. Therefore specific larger residuals indicate specific faults.

The consequence of different residuals between the FDI methods requires that different decision processes have to be used. The bank of Kalman filters send its residuals to a Bayes classifier (discussed in section 3.3.1), which uses the statistical information supplied by the extended Kalman filters to determine the most likely fault scenario. The parity space capitalises on the fact that the variance of the correct residual increases when a fault occurs. The CUSUM method (discussed in section 4.4.2) then use these residuals together with predefined statistical information to determine the most likely actuator fault scenario. Both the decision processes use the variance of the residuals to help determine the active fault scenario. The extended Kalman filter however determines the statistical information more accurately and in real time, which gives it some advantage over the parity space method.

The parity space method on the other hand does not have to determine all the statistical information or Kalman gains in real time as the extended Kalman filters have to. The parity space method therefore uses much less computational power as the null space of the observability matrix, as well as the optimisation of the transformation matrix (discussed in section 4.3), can be determined beforehand.

Chapter 7

Recommendations and Conclusion

7.1 Recommendations

The recommendations proposed in this section are focused on improving the FDI and control re-allocation processes that were developed in this research and at the ESL. These recommendations did not fall in the scope of this study but can be used in future research.

7.1.1 Different Failure Modes

In figure 1.1 (section 1.2.1) different actuator failure modes were described. It is recommended that actuator deflection estimators be developed that can estimate different types of faults, such as floating faults or effectiveness faults. A control re-allocation process can then be researched that can also accommodate such faults. From the simulations done in sections 3.4 and 4.6, it is seen that the estimates follow the true actuator deflections and the investigation into a re-allocation process that can handle other types of faults seems viable.

7.1.2 Process Noise Estimation

One of the shortcomings of the FDI development done thus far in the research was the dependence of the design on the expected process noise. The robustness of both FDI processes are dependent on the correlation between the expected process noise and the actual process noise present when the aircraft is flying.

One solution to this problem would be to estimate the process noise in flight, and then by means of gain scheduling, or other methods, to adapt the process noise covariance matrix in the bank of Kalman filters or the CUSUM parameters in the parity space FDI.

A proposed method would be to use any available real time wind data from locations near the flight test airports and radio flyer clubs to determine the process noise from the wind velocities. The problem with this approach is the unknown availability and accuracy of the data, as well as excluding other process noise influences.

In [33] several methods are described that can help in estimating the amount of process noise. Note that a fault itself has an effect on the estimated process noise through these methods and must be taken into account.

7.1.3 Non-Linear Parity Space FDI

One of the shortcomings found in the performance of the parity space FDI was the inability to operate effectively outside the linear trim region of the aircraft's flight envelope. It is highly recommended that the possibility of a non-linear parity space method for actuator FDI be investigated.

7.1.4 Practical implementation of the FDI methods

The research shows that the FDI methods are reliable for detecting and isolating aileron faults, but as the process noise increases, the FDI performance in terms of detecting elevator and rudder faults starts to decrease. It is recommended that the Meraka Modular UAV be equipped with an FDI module that focuses on specific faults in accordance with the estimated process noise. At low process noise, all actuators can be eligible for FDI, but at higher process noise it is recommended that only aileron faults be detected. When too much process noise is detected, the FDI module can be switched off.

It was found that it was difficult to isolate an elevator fault, but detecting an elevator fault is not that difficult for any of the two FDI methods. If the need arises to use this research's FDIs to detect elevator faults at high process noise levels, it is recommended not to also try and accomplish isolation.

FDI considerations on other aircraft however, must be analysed separately to determine the effectiveness of the FDI methods for their specific actuators.

7.2 Active Fault Detection and Isolation

The suggested improvement in this section focuses on extra actuator excitation that could not be tested on flight tests, but would be able to improve the FDI performance of both the bank of Kalman filters and parity space FDI.

The aim of active fault FDI is to artificially excite the actuators and therefore obtain more effective FDI performance when a fault occurs. The disadvantage of this procedure is that the aircraft loses some of its manoeuvrability, there is more wear on the actuators, and more energy is required to artificially excite the actuators. There are numerous ways of constructing the signal to artificially excite the actuators. In [13] the individual external actuator signals are chosen to reduce the overall dynamic effects that the external excitation has on the system, while still sufficiently exciting the actuators. In [2] external excitation is only used when the system suspects a fault but is still not sure the fault has occurred. This method improves the performance of the FDI by dramatically lowering the false alarm rate, but missed detections are still prevalent.

A simulation was run in MATLAB[®] R2008b with the implementation of Simulink. The same Simulink architecture was used as in chapters 3 and 4. The control system added an extra control signal to each actuator. The aim of this simulation was to demonstrate the improvement in performance that external excitation has on FDI and therefore a simple excitation signal is adopted. The extra excitation is a basic sinusoidal signal of 1° amplitude with a frequency of $\frac{2\pi}{4}$ rad/s. The minimum amplitude that must be detected is chosen as an 1° actuator fault.

The simulation was run only on the straight and level flight with minimal process noise as this was the mission with the worst case FDI performance.

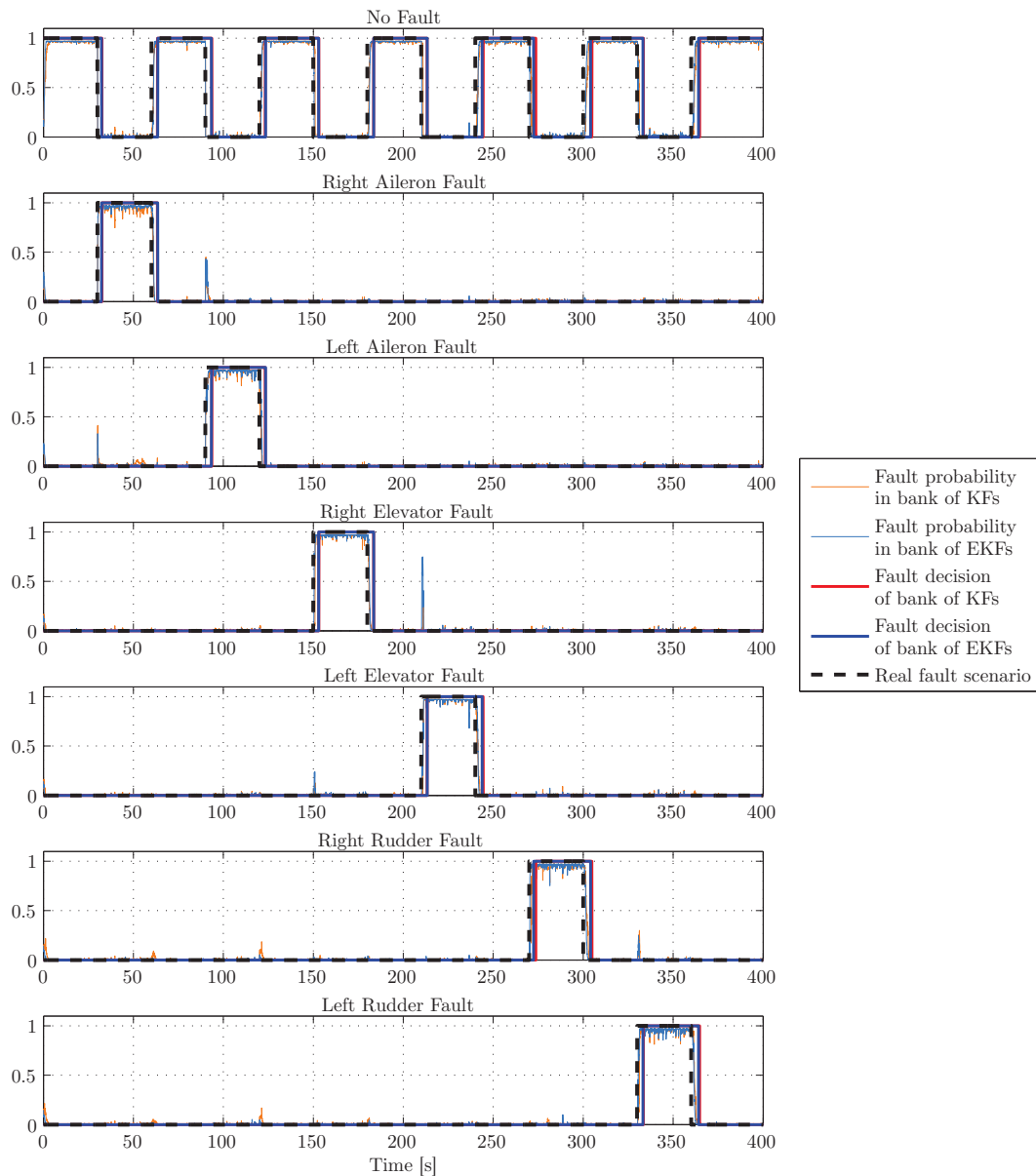


Figure 7.1: The bank of Kalman filters FDI decisions where extra actuator excitation was added.

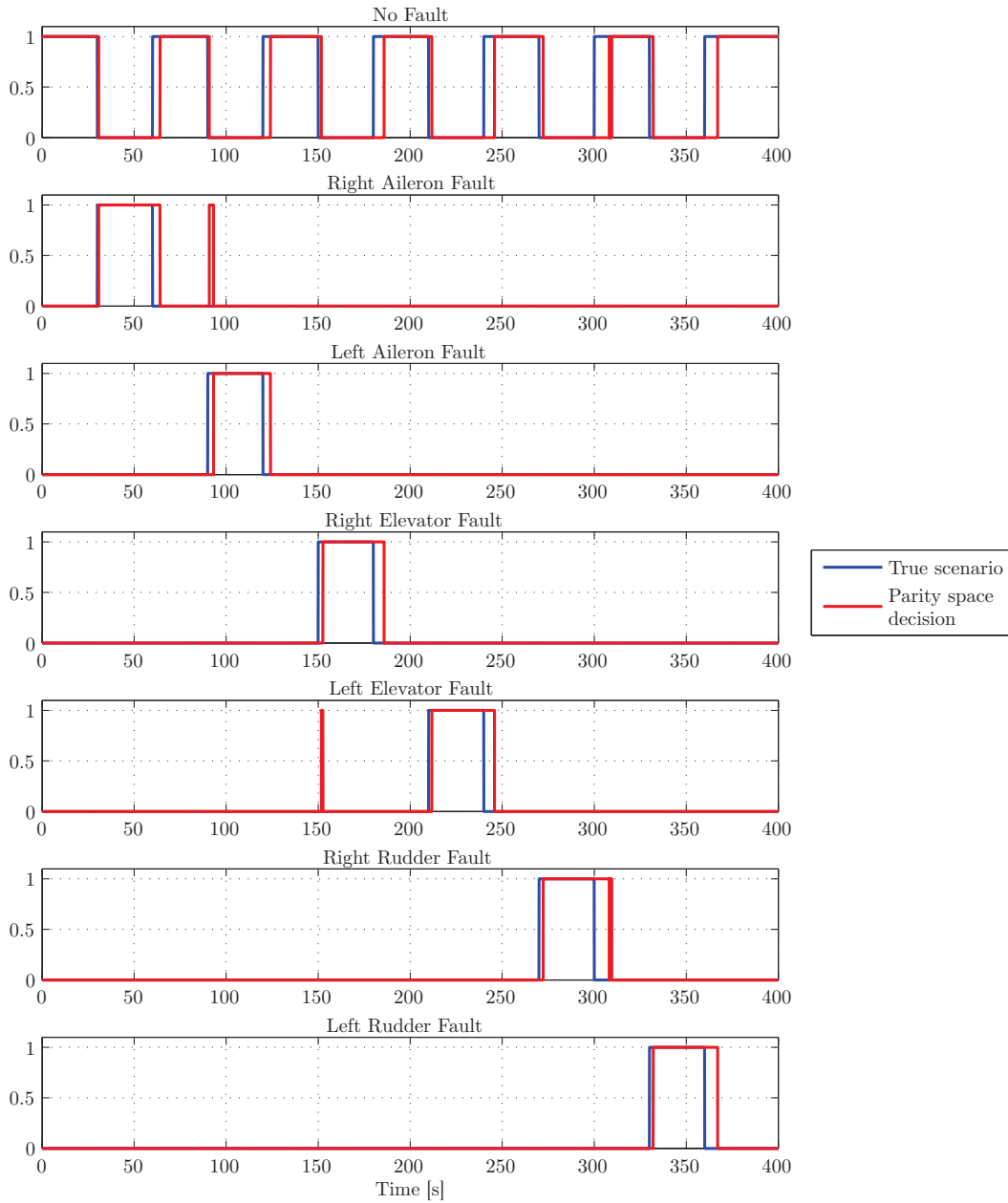


Figure 7.2: Parity space FDI decisions where extra actuator excitation was added.

In figures 7.1 and 7.2 it is evident that extra actuator excitation significantly increases FDI performance as was expected throughout this research.

7.3 Conclusion

One of the advantages of using the bank of Kalman filters for FDI is that it is prone to fewer false alarms in comparison to the parity space method. On the other hand it is less sensitive to faults and consequently produces more missed detections. The possible instability associated with the extended Kalman filters used in this research requires using this method carefully, especially when extreme flight manoeuvres are expected. An added disadvantage is the higher amount of processing power required to run a bank of Kalman filters on board the aircraft. However, one of the major advantages of the bank of Kalman filters is the ability to manage the non-linearities of aircraft flight much better than the parity space approach to FDI.

The parity space method for FDI is seen to have higher fault sensitivity and is therefore able to detect faults faster than the bank of Kalman filters. The parity space approach, however, is a linear process designed around the trim condition of the aircraft. This fact, coupled with the system's higher sensitivity to faults, causes it to produce more false alarms. The main advantage of the parity space method is the design freedom that it grants the designer. All the analytical redundancies of the system are determined and contained in the parity relations. The FDI designer can then use a simple optimisation process to compute a transformation matrix that transforms the parity relations into any desired residuals. The added advantage of this design procedure is that it uses less computational power than the bank of extended Kalman filters.

One of the conclusions of this research is that no one of these methods is necessarily better than the other. The type of aircraft, expected flight envelope and available computational power are all considerations that should aid in deciding which FDI method is better for the specific task at hand. If the aircraft is expected to fly excessive manoeuvres and has enough computational power on board, the bank of Kalman filters is the recommended choice for FDI. If the aircraft's computational power is limited and the aircraft is expected to fly near its trim conditions, the parity space method for FDI is a viable option.

One of the main conclusions that was reached in this research was that the greatest design parameters are the expected amount of measurement and process noise. For all practical considerations, the measurement noise is expected to be less than the process noise to such an extent that the process noise becomes the dominant design parameter. The process noise quantifies several unknown quantities that include the expected wind gust velocity, unmodelled dynamics and effects of different aircraft parameters. It is unfortunately impossible to know the exact amount of process noise, as well as its statistical behaviour. The FDIs developed in this research have shown to perform as expected despite these challenges.

From the research some conclusions can be drawn with regard to the Meraka Modular UAV. For this specific aircraft it was shown that even in the presence of large wind gusts, aileron faults could be correctly detected. It was also shown that both FDI methods had difficulty

correctly discerning between the left and right elevator. The FDI's were demonstrated to have decreased sensitivity to rudders faults, so that high amounts of actuator excitation were required to detect rudder faults.

The actuator deflection estimates were shown to be very susceptible to the effects of process noise, especially the rudders. The conclusion can be drawn that the FDI methods' performance are varyingly sensitive to different pairs of actuators in accordance with the physical construction of the specific aircraft, as well as the amount of actual process noise.

Actuator excitation is seen throughout the research to be the most important factor in effective fault detection. Without sufficient actuator excitation, the residuals of both FDI methods would be insufficiently dissimilar to produce meaningful FDI performance. In the flight tests, however, natural excitation was shown to produce adequate FDI for the ailerons and extra induced actuator excitation was shown to assist in detecting rudder faults.

The FDI methods developed in this research show that the design of the physical aircraft influences the achievable FDI performance. It also illustrates that direct actuator sensor costs can be reduced on the Meraka Modular UAV if the use of the chosen FDI be augmented with an active actuator excitation supervisor and/or a process noise estimator. The research topic is also rich in cross disciplinary subject matter that develops deep insight into the workings of a typical aircraft system.

Appendix A

Aircraft Parameters: The Meraka Modular UAV

Parameter	Value
Mass	26.0 kg
Wing Span	4.0 m
Mean Aerodynamic Chord	0.36 m
Wing Reference Area	1.44 m ²
Wing Aspect Ratio	11.11
Wing Efficiency Factor	0.85

Table A.1: Meraka Modular UAV physical parameters.

The moment of inertia tensor was determined by weighing and measuring the separate aircraft components and creating an accurate three-dimensional computer model. The moment of inertia tensor was calculated with Autodesk Inventor[®] as

$$\mathbf{I}_b = \begin{bmatrix} 12.18 & 0 & 0 \\ 0 & 5.86 & 0 \\ 0 & 0 & 17.29 \end{bmatrix} kg.m^2 \quad (\text{A.0.1})$$

Parameter	Value
C_{D_0}	0.06
C_{L_0}	0.5
C_{L_α}	5.557928
C_{Y_β}	-0.389444
C_{M_0}	-0.05
C_{M_α}	-1.069455
C_{l_β}	-0.071508
C_{n_β}	0.102214

Table A.2: Meraka Modular UAV stability derivatives.

Each column in table A.3 represents the transpose of the control derivative row vectors used in equations 2.6.11 to 2.6.16.

Actuator	C_{l_δ}	C_{Y_δ}	C_{L_δ}	C_{M_δ}	C_{N_δ}
Left Aileron	-0.47515	-0.009786	-0.16364	0.062452	0.005796
Right Aileron	0.47515	-0.009786	-0.16364	-0.062452	0.005796
Left Flap	0.59232	-0.010199	0.11539	-0.065031	0.003495
Right Flap	0.59232	0.010199	-0.11539	-0.065031	-0.003495
Left Elevator	0.17624	-0.028361	0.0072193	-0.6157	0.0092819
Right Elevator	0.17624	0.028361	-0.0072193	-0.6157	-0.0092819
Left Rudder	-0.3856	0.10766	0.0029221	0.13189	-0.035695
Right Rudder	0.3856	0.10766	0.0029221	-0.13189	-0.035695

Table A.3: Meraka Modular UAV control derivatives.

Appendix B

Linearisation

B.1 State Matrices

$$\begin{aligned}
 \begin{bmatrix} \dot{p} \\ \dot{q} \\ \dot{r} \\ \dot{\alpha} \\ \dot{\beta} \end{bmatrix} &= \begin{bmatrix} \frac{\partial \dot{P}}{\partial P} & \frac{\partial \dot{P}}{\partial Q} & \frac{\partial \dot{P}}{\partial R} & |\mathbf{V}|_{\text{wp}} \frac{\partial \dot{P}}{\partial W} & |\mathbf{V}|_{\text{wp}} \frac{\partial \dot{P}}{\partial V} \\ \frac{\partial \dot{Q}}{\partial P} & \frac{\partial \dot{Q}}{\partial Q} & \frac{\partial \dot{Q}}{\partial R} & |\mathbf{V}|_{\text{wp}} \frac{\partial \dot{Q}}{\partial W} & |\mathbf{V}|_{\text{wp}} \frac{\partial \dot{Q}}{\partial V} \\ \frac{\partial \dot{R}}{\partial P} & \frac{\partial \dot{R}}{\partial Q} & \frac{\partial \dot{R}}{\partial R} & |\mathbf{V}|_{\text{wp}} \frac{\partial \dot{R}}{\partial W} & |\mathbf{V}|_{\text{wp}} \frac{\partial \dot{R}}{\partial V} \\ \frac{1}{|\mathbf{V}|_{\text{wp}}} \frac{\partial \dot{W}}{\partial P} & \frac{1}{|\mathbf{V}|_{\text{wp}}} \frac{\partial \dot{W}}{\partial Q} & \frac{1}{|\mathbf{V}|_{\text{wp}}} \frac{\partial \dot{W}}{\partial R} & \frac{\partial \dot{W}}{\partial W} & \frac{\partial \dot{W}}{\partial V} \\ \frac{1}{|\mathbf{V}|_{\text{wp}}} \frac{\partial \dot{V}}{\partial P} & \frac{1}{|\mathbf{V}|_{\text{wp}}} \frac{\partial \dot{V}}{\partial Q} & \frac{1}{|\mathbf{V}|_{\text{wp}}} \frac{\partial \dot{V}}{\partial R} & \frac{\partial \dot{V}}{\partial W} & \frac{\partial \dot{V}}{\partial V} \end{bmatrix}_{\text{wp}} \begin{bmatrix} p \\ q \\ r \\ \alpha \\ \beta \end{bmatrix} + \\
 &\begin{bmatrix} \frac{\partial \dot{P}}{\partial \delta_{Ar}} & \frac{\partial \dot{P}}{\partial \delta_{Al}} & \frac{\partial \dot{P}}{\partial \delta_{Er}} & \frac{\partial \dot{P}}{\partial \delta_{El}} \\ \frac{\partial \dot{Q}}{\partial \delta_{Ar}} & \frac{\partial \dot{Q}}{\partial \delta_{Al}} & \frac{\partial \dot{Q}}{\partial \delta_{Er}} & \frac{\partial \dot{Q}}{\partial \delta_{El}} \\ \frac{\partial \dot{R}}{\partial \delta_{Ar}} & \frac{\partial \dot{R}}{\partial \delta_{Al}} & \frac{\partial \dot{R}}{\partial \delta_{Er}} & \frac{\partial \dot{R}}{\partial \delta_{El}} & \dots \\ \frac{1}{|\mathbf{V}|_{\text{wp}}} \frac{\partial \dot{W}}{\partial \delta_{Ar}} & \frac{1}{|\mathbf{V}|_{\text{wp}}} \frac{\partial \dot{W}}{\partial \delta_{Al}} & \frac{1}{|\mathbf{V}|_{\text{wp}}} \frac{\partial \dot{W}}{\partial \delta_{Er}} & \frac{1}{|\mathbf{V}|_{\text{wp}}} \frac{\partial \dot{W}}{\partial \delta_{El}} \\ \frac{1}{|\mathbf{V}|_{\text{wp}}} \frac{\partial \dot{V}}{\partial \delta_{Ar}} & \frac{1}{|\mathbf{V}|_{\text{wp}}} \frac{\partial \dot{V}}{\partial \delta_{Al}} & \frac{1}{|\mathbf{V}|_{\text{wp}}} \frac{\partial \dot{V}}{\partial \delta_{Er}} & \frac{1}{|\mathbf{V}|_{\text{wp}}} \frac{\partial \dot{V}}{\partial \delta_{El}} \end{bmatrix} \\
 \dots &\begin{bmatrix} \frac{\partial \dot{P}}{\partial \delta_{Fr}} & \frac{\partial \dot{P}}{\partial \delta_{Fl}} & \frac{\partial \dot{P}}{\partial \delta_{Rr}} & \frac{\partial \dot{P}}{\partial \delta_{Rl}} \\ \frac{\partial \dot{Q}}{\partial \delta_{Fr}} & \frac{\partial \dot{Q}}{\partial \delta_{Fl}} & \frac{\partial \dot{Q}}{\partial \delta_{Rr}} & \frac{\partial \dot{Q}}{\partial \delta_{Rl}} \\ \frac{\partial \dot{R}}{\partial \delta_{Fr}} & \frac{\partial \dot{R}}{\partial \delta_{Fl}} & \frac{\partial \dot{R}}{\partial \delta_{Rr}} & \frac{\partial \dot{R}}{\partial \delta_{Rl}} \\ \frac{1}{|\mathbf{V}|_{\text{wp}}} \frac{\partial \dot{W}}{\partial \delta_{Fr}} & \frac{1}{|\mathbf{V}|_{\text{wp}}} \frac{\partial \dot{W}}{\partial \delta_{Fl}} & \frac{1}{|\mathbf{V}|_{\text{wp}}} \frac{\partial \dot{W}}{\partial \delta_{Rr}} & \frac{1}{|\mathbf{V}|_{\text{wp}}} \frac{\partial \dot{W}}{\partial \delta_{Rl}} \\ \frac{1}{|\mathbf{V}|_{\text{wp}}} \frac{\partial \dot{V}}{\partial \delta_{Fr}} & \frac{1}{|\mathbf{V}|_{\text{wp}}} \frac{\partial \dot{V}}{\partial \delta_{Fl}} & \frac{1}{|\mathbf{V}|_{\text{wp}}} \frac{\partial \dot{V}}{\partial \delta_{Rr}} & \frac{1}{|\mathbf{V}|_{\text{wp}}} \frac{\partial \dot{V}}{\partial \delta_{Rl}} \end{bmatrix}_{\text{wp}} \begin{bmatrix} \delta_{Ar} \\ \delta_{Al} \\ \delta_{Er} \\ \delta_{El} \\ \delta_{Fr} \\ \delta_{Fl} \\ \delta_{Rr} \\ \delta_{Rl} \end{bmatrix} \quad (\text{B.1.1})
 \end{aligned}$$

B.2 Partial Derivatives of the Elements in the State Matrices

This section is concerned with the linearisation process by determining the partial derivatives contained in the state matrices of equation B.1.1 in section B.1. For the linearisation process we note that the five states used in the FDI system are not dependent on the gravitational or thrust forces and moments, but only on the aerodynamic forces and moments. The value

of α is assumed small so that $\cos \alpha_T \approx 1$ and $\sin \alpha_T \approx \alpha_T$. The forward velocity U is approximated by $|\mathbf{V}|$ as is done in equation B.2.55 and B.2.82.

Note that \bar{q}_{wp} is the dynamic pressure from equation 2.6.1 evaluated at the working point.

$$\left. \frac{\partial \dot{P}}{\partial P} \right|_{wp} = \frac{\partial}{\partial P} \left(\frac{1}{I_{xx}} (L - QR(I_{zz} - I_{yy})) \right) \quad (\text{B.2.1})$$

$$= \frac{1}{I_{xx}} \frac{\partial}{\partial P} L_a \quad (\text{B.2.2})$$

$$= \frac{1}{I_{xx}} \frac{\partial}{\partial P} C_L \left(\frac{1}{2} \rho |\mathbf{V}|_{wp}^2 S \right) b \quad (\text{B.2.3})$$

$$= \frac{1}{I_{xx}} \frac{\partial}{\partial P} \left(\frac{b}{2|\mathbf{V}|_{wp}} C_{LP} P \right) \left(\frac{1}{2} \rho |\mathbf{V}|_{wp}^2 S \right) b \quad (\text{B.2.4})$$

$$= \frac{\bar{q}_{wp} S b^2}{2I_{xx} |\mathbf{V}|_{wp}} C_{LP} \quad (\text{B.2.5})$$

$$\left. \frac{\partial \dot{P}}{\partial Q} \right|_{wp} = \frac{\partial}{\partial Q} \left(\frac{1}{I_{xx}} (L - QR(I_{zz} - I_{yy})) \right) \quad (\text{B.2.6})$$

$$= \frac{1}{I_{xx}} \frac{\partial}{\partial Q} L - \frac{1}{I_{xx}} R_{wp} (I_{zz} - I_{yy}) \quad (\text{B.2.7})$$

$$= \frac{R_{wp} (I_{yy} - I_{zz})}{I_{xx}} \quad (\text{B.2.8})$$

$$\left. \frac{\partial \dot{P}}{\partial R} \right|_{wp} = \frac{\partial}{\partial R} \left(\frac{1}{I_{xx}} (L - QR(I_{zz} - I_{yy})) \right) \quad (\text{B.2.9})$$

$$= \frac{1}{I_{xx}} \frac{\partial}{\partial R} L - \frac{1}{I_{xx}} Q_{wp} (I_{zz} - I_{yy}) \quad (\text{B.2.10})$$

$$= \frac{\bar{q}_{wp} S b^2}{2I_{xx} |\mathbf{V}|_{wp}} C_{LR} + \frac{Q_{wp} (I_{yy} - I_{zz})}{I_{xx}} \quad (\text{B.2.11})$$

$$|\mathbf{V}|_{wp} \left. \frac{\partial \dot{P}}{\partial W} \right|_{wp} = |\mathbf{V}|_{wp} \frac{\partial}{\partial W} \left(\frac{1}{I_{xx}} (L - QR(I_{zz} - I_{yy})) \right) \quad (\text{B.2.12})$$

$$= \frac{\partial}{\partial \alpha} \left(\frac{1}{I_{xx}} (L - QR(I_{zz} - I_{yy})) \right) \quad (\text{B.2.13})$$

$$= 0 \quad (\text{B.2.14})$$

$$|\mathbf{V}|_{wp} \frac{\partial \dot{P}}{\partial V} \Big|_{wp} = |\mathbf{V}|_{wp} \frac{\partial}{\partial V} \left(\frac{1}{I_{xx}} (L - QR(I_{zz} - I_{yy})) \right) \quad (\text{B.2.15})$$

$$= \frac{\partial}{\partial \beta} \left(\frac{1}{I_{xx}} (L - QR(I_{zz} - I_{yy})) \right) \quad (\text{B.2.16})$$

$$= \frac{1}{I_{xx}} \frac{\partial}{\partial \beta} L \quad (\text{B.2.17})$$

$$= \frac{1}{I_{xx}} C_{L\beta} \left(\frac{1}{2} \rho |\mathbf{V}|_{wp}^2 S \right) b \quad (\text{B.2.18})$$

$$= \frac{\bar{q}_{wp} S b}{I_{xx}} C_{L\beta} \quad (\text{B.2.19})$$

$$\frac{\partial \dot{Q}}{\partial P} \Big|_{wp} = \frac{\partial}{\partial P} \left(\frac{1}{I_{yy}} (M - PR(I_{xx} - I_{zz})) \right) \quad (\text{B.2.20})$$

$$= \frac{1}{I_{yy}} \left(\frac{\partial}{\partial P} M - R_{wp}(I_{xx} - I_{zz}) \right) \quad (\text{B.2.21})$$

$$= \frac{R_{wp}(I_{zz} - I_{xx})}{I_{yy}} \quad (\text{B.2.22})$$

$$\frac{\partial \dot{Q}}{\partial Q} \Big|_{wp} = \frac{\partial}{\partial Q} \left(\frac{1}{I_{yy}} (M - PR(I_{xx} - I_{zz})) \right) \quad (\text{B.2.23})$$

$$= \frac{1}{I_{yy}} \frac{\partial}{\partial Q} M \quad (\text{B.2.24})$$

$$= \frac{\bar{q}_{wp} S \bar{c}^2}{2I_{yy} |\mathbf{V}|_{wp}} C_{M_Q} \quad (\text{B.2.25})$$

$$\frac{\partial \dot{Q}}{\partial R} \Big|_{wp} = \frac{\partial}{\partial R} \left(\frac{1}{I_{yy}} (M - PR(I_{xx} - I_{zz})) \right) \quad (\text{B.2.26})$$

$$= \frac{1}{I_{yy}} \left(\frac{\partial}{\partial R} M - P_{wp}(I_{xx} - I_{zz}) \right) \quad (\text{B.2.27})$$

$$= \frac{P_{wp}(I_{zz} - I_{xx})}{I_{yy}} \quad (\text{B.2.28})$$

$$|\mathbf{V}|_{wp} \frac{\partial \dot{Q}}{\partial W} \Big|_{wp} = |\mathbf{V}|_{wp} \frac{\partial}{\partial W} \left(\frac{1}{I_{yy}} (M - PR(I_{xx} - I_{zz})) \right) \quad (\text{B.2.29})$$

$$= \frac{1}{I_{yy}} \frac{\partial}{\partial \alpha} M \quad (\text{B.2.30})$$

$$= \frac{\bar{q}_{wp} S \bar{c}}{I_{yy}} C_{M_\alpha} \quad (\text{B.2.31})$$

$$|\mathbf{V}|_{wp} \frac{\partial \dot{Q}}{\partial V} \Big|_{wp} = |\mathbf{V}|_{wp} \frac{\partial}{\partial V} \left(\frac{1}{I_{yy}} (M - \mathcal{P}\mathcal{R}(I_{xx} - I_{zz})) \right) \quad (\text{B.2.32})$$

$$= \frac{1}{I_{yy}} \frac{\partial}{\partial \beta} M \quad (\text{B.2.33})$$

$$= 0 \quad (\text{B.2.34})$$

$$\frac{\partial \dot{R}}{\partial P} \Big|_{wp} = \frac{\partial}{\partial P} \left(\frac{1}{I_{zz}} (N - PQ(I_{yy} - I_{xx})) \right) \quad (\text{B.2.35})$$

$$= \frac{1}{I_{zz}} \left(\frac{\partial}{\partial P} N - Q_{wp}(I_{yy} - I_{xx}) \right) \quad (\text{B.2.36})$$

$$= \frac{\bar{q}_{wp} S b^2}{2I_{zz} |\mathbf{V}|_{wp}} C_{N_P} + \frac{Q_{wp}(I_{xx} - I_{yy})}{I_{zz}} \quad (\text{B.2.37})$$

$$\frac{\partial \dot{R}}{\partial Q} \Big|_{wp} = \frac{\partial}{\partial Q} \left(\frac{1}{I_{zz}} (N - PQ(I_{yy} - I_{xx})) \right) \quad (\text{B.2.38})$$

$$= \frac{1}{I_{zz}} \left(\frac{\partial}{\partial Q} N - P_{wp}(I_{yy} - I_{xx}) \right) \quad (\text{B.2.39})$$

$$= \frac{P_{wp}(I_{xx} - I_{yy})}{I_{zz}} \quad (\text{B.2.40})$$

$$\frac{\partial \dot{R}}{\partial R} \Big|_{wp} = \frac{\partial}{\partial R} \left(\frac{1}{I_{zz}} (N - \mathcal{P}\mathcal{Q}(I_{yy} - I_{xx})) \right) \quad (\text{B.2.41})$$

$$= \frac{1}{I_{zz}} \frac{\partial}{\partial R} N \quad (\text{B.2.42})$$

$$= \frac{\bar{q}_{wp} S b^2}{2I_{zz} |\mathbf{V}|_{wp}} C_{N_R} \quad (\text{B.2.43})$$

$$|\mathbf{V}|_{wp} \frac{\partial \dot{R}}{\partial W} \Big|_{wp} = |\mathbf{V}|_{wp} \frac{\partial}{\partial W} \left(\frac{1}{I_{zz}} (N - \mathcal{P}\mathcal{Q}(I_{yy} - I_{xx})) \right) \quad (\text{B.2.44})$$

$$= \frac{1}{I_{zz}} \frac{\partial}{\partial \alpha} N \quad (\text{B.2.45})$$

$$= 0 \quad (\text{B.2.46})$$

$$|\mathbf{V}|_{wp} \frac{\partial \dot{R}}{\partial V} \Big|_{wp} = |\mathbf{V}|_{wp} \frac{\partial}{\partial V} \left(\frac{1}{I_{zz}} (N - \mathcal{P}\mathcal{Q}(I_{yy} - I_{xx})) \right) \quad (\text{B.2.47})$$

$$= \frac{1}{I_{zz}} \frac{\partial}{\partial \beta} N \quad (\text{B.2.48})$$

$$= \frac{\bar{q}_{wp} S b}{I_{zz}} C_{N_\beta} \quad (\text{B.2.49})$$

$$\left. \frac{1}{|\mathbf{V}|_{wp}} \frac{\partial \dot{W}}{\partial P} \right|_{wp} = \frac{1}{|\mathbf{V}|_{wp}} \frac{\partial}{\partial P} \left(\frac{Z}{m} + UQ - VP \right) \quad (\text{B.2.50})$$

$$= \frac{1}{|\mathbf{V}|_{wp}} \left(\frac{\partial}{\partial P} \frac{Z}{m} - V_{wp} \right) \quad (\text{B.2.51})$$

$$= \frac{1}{m|\mathbf{V}|_{wp}} \frac{\partial}{\partial P} (-C_d \sin \alpha - C_l \cos \alpha) (\bar{q}_{wp} S) \quad (\text{B.2.52})$$

$$= 0 \quad (\text{B.2.53})$$

$$\left. \frac{1}{|\mathbf{V}|_{wp}} \frac{\partial \dot{W}}{\partial Q} \right|_{wp} = \frac{1}{|\mathbf{V}|_{wp}} \frac{\partial}{\partial Q} \left(\frac{Z}{m} + UQ - VP \right) \quad (\text{B.2.54})$$

$$= \frac{1}{|\mathbf{V}|_{wp}} \left(\frac{\partial}{\partial Q} \frac{Z}{m} + U_{wp} \right) \quad (\text{B.2.55})$$

$$= \frac{1}{m|\mathbf{V}|_{wp}} \frac{\partial}{\partial Q} (-C_d \sin \alpha - C_l \cos \alpha) (\bar{q}_{wp} S) + 1 \quad (\text{B.2.56})$$

$$= \frac{1}{m|\mathbf{V}|_{wp}} \frac{\partial}{\partial Q} \left(-\frac{C_l^2}{\pi A e} \alpha_{wp} - C_l \right) (\bar{q}_{wp} S) + 1 \quad (\text{B.2.57})$$

$$= \frac{1}{m|\mathbf{V}|_{wp}} \left(-\left(\frac{2\bar{c}C_{lQ}Q_{wp}}{2|\mathbf{V}|_{wp}(\pi A e)^2} \right) \alpha_{wp} - \frac{\bar{c}}{2|\mathbf{V}|_{wp}} C_{lQ} \right) (\bar{q}_{wp} S) + 1 \quad (\text{B.2.58})$$

$$= 1 - \frac{\bar{q}_{wp} S \bar{c}}{2m|\mathbf{V}|_{wp}^2} C_{lQ} \quad (\text{B.2.59})$$

$$\left. \frac{1}{|\mathbf{V}|_{wp}} \frac{\partial \dot{W}}{\partial R} \right|_{wp} = \frac{1}{|\mathbf{V}|_{wp}} \frac{\partial}{\partial R} \left(\frac{Z}{m} + UQ - VP \right) \quad (\text{B.2.60})$$

$$= \frac{1}{m|\mathbf{V}|_{wp}} \frac{\partial}{\partial R} Z \quad (\text{B.2.61})$$

$$= 0 \quad (\text{B.2.62})$$

$$\left. \frac{\partial \dot{W}}{\partial W} \right|_{wp} = \frac{1}{|\mathbf{V}|_{wp}} \frac{\partial}{\partial \alpha} \left(\frac{Z}{m} + UQ - VP \right) \quad (\text{B.2.63})$$

$$= \frac{1}{m|\mathbf{V}|_{wp}} \frac{\partial}{\partial \alpha} Z \quad (\text{B.2.64})$$

$$= \frac{1}{m|\mathbf{V}|_{wp}} \frac{\partial}{\partial \alpha} (-C_d \alpha - C_l) (\bar{q}_{wp} S) \quad (\text{B.2.65})$$

$$= \frac{1}{m|\mathbf{V}|_{wp}} \left(-(C_d)_{wp} - \alpha_{wp} \frac{\partial}{\partial \alpha} (C_d) - \frac{\partial}{\partial \alpha} (C_l) \right) (\bar{q}_{wp} S) \quad (\text{B.2.66})$$

$$= \frac{1}{m|\mathbf{V}|_{wp}} \left(-(C_d)_{wp} - \alpha_{wp} \frac{2(C_l)_{wp} C_{l\alpha}}{\pi A e} - C_{l\alpha} \right) (\bar{q}_{wp} S) \quad (\text{B.2.67})$$

$$\text{but } (C_d)_{wp} \ll C_{l\alpha} \text{ and } \alpha_{wp} \frac{2(C_l)_{wp} C_{l\alpha}}{\pi A e} \ll C_{l\alpha} \text{ therefore} \quad (\text{B.2.68})$$

$$\left. \frac{\partial \dot{W}}{\partial W} \right|_{wp} \approx \frac{1}{m|\mathbf{V}|_{wp}} (-0 - 0 - C_{l\alpha}) (\bar{q}_{wp} S) \quad (\text{B.2.69})$$

$$= -\frac{\bar{q}_{wp} S}{m|\mathbf{V}|_{wp}} C_{l\alpha} \quad (\text{B.2.70})$$

$$\left. \frac{\partial \dot{W}}{\partial V} \right|_{wp} = \frac{\partial}{\partial V} \left(\frac{Z}{m} + \mathcal{U}\mathcal{Q} - VP \right) \quad (\text{B.2.71})$$

$$= \frac{1}{|\mathbf{V}|_{wp}} \left(\frac{\partial Z}{\partial \beta} \frac{1}{m} \right) - P_{wp} \quad (\text{B.2.72})$$

$$= \frac{1}{m|\mathbf{V}|_{wp}} \frac{\partial}{\partial \beta} (-C_d \sin \alpha - C_l \cos \alpha) (\bar{q}_{wp} S) - P_{wp} \quad (\text{B.2.73})$$

$$= -P_{wp} \quad (\text{B.2.74})$$

$$\left. \frac{1}{|\mathbf{V}|_{wp}} \frac{\partial \dot{V}}{\partial P} \right|_{wp} = \frac{1}{|\mathbf{V}|_{wp}} \frac{\partial}{\partial P} \left(\frac{Y}{m} - \mathcal{U}\mathcal{R} + WP \right) \quad (\text{B.2.75})$$

$$= \frac{1}{|\mathbf{V}|_{wp}} \left(\frac{\partial Y}{\partial P} \frac{1}{m} + W_{wp} \right) \quad (\text{B.2.76})$$

$$= \frac{1}{|\mathbf{V}|_{wp}} \left(\frac{\partial}{\partial P} \frac{1}{m} (\bar{q}_{wp} S C_Y) \right) \quad (\text{B.2.77})$$

$$= \frac{\bar{q}_{wp} S b}{2m|\mathbf{V}|_{wp}^2} C_{Y_P} \quad (\text{B.2.78})$$

$$\left. \frac{1}{|\mathbf{V}|_{wp}} \frac{\partial \dot{V}}{\partial Q} \right|_{wp} = \frac{1}{|\mathbf{V}|_{wp}} \frac{\partial}{\partial Q} \left(\frac{Y}{m} - \mathcal{U}\mathcal{R} + WP \right) \quad (\text{B.2.79})$$

$$= 0 \quad (\text{B.2.80})$$

$$\left. \frac{1}{|\mathbf{V}|_{wp}} \frac{\partial \dot{V}}{\partial R} \right|_{wp} = \frac{1}{|\mathbf{V}|_{wp}} \frac{\partial}{\partial R} \left(\frac{Y}{m} - UR + WP \right) \quad (\text{B.2.81})$$

$$= \frac{1}{|\mathbf{V}|_{wp}} \left(\frac{\partial}{\partial R} \frac{1}{m} (\bar{q}_{wp} S C_Y) - U_{wp} \right) \quad (\text{B.2.82})$$

$$= \frac{\bar{q}_{wp} S b}{2m|\mathbf{V}|_{wp}^2} C_{Y_R} - 1 \quad (\text{B.2.83})$$

$$\left. \frac{\partial \dot{V}}{\partial W} \right|_{wp} = \frac{\partial}{\partial W} \left(\frac{Y}{m} - \mathcal{U}\mathcal{R} + WP \right) \quad (\text{B.2.84})$$

$$= \frac{1}{|\mathbf{V}|_{wp}} \left(\frac{\partial Y}{\partial \alpha} \frac{1}{m} + P_{wp} \right) \quad (\text{B.2.85})$$

$$= \frac{1}{m|\mathbf{V}|_{wp}} \frac{\partial}{\partial \alpha} (\bar{q}_{wp} S C_Y) + P_{wp} \quad (\text{B.2.86})$$

$$= P_{wp} \quad (\text{B.2.87})$$

$$\left. \frac{\partial \dot{V}}{\partial V} \right|_{wp} = \frac{\partial}{\partial V} \left(\frac{Y}{m} - \mathcal{V}\mathcal{R} + \mathcal{W}\mathcal{P} \right) \quad (\text{B.2.88})$$

$$= \frac{1}{m|\mathbf{V}|_{wp}} \frac{\partial}{\partial \beta} (\bar{q}_{wp} S C_Y) \quad (\text{B.2.89})$$

$$= \frac{\bar{q}_{wp} S}{m|\mathbf{V}|_{wp}} C_{Y_\beta} \quad (\text{B.2.90})$$

The partial derivative terms relating the actuators to the states are very similar. For convenience the specific actuator subscript will be substituted by \square . The resulting partial derivatives are

$$\left. \frac{\partial \dot{P}}{\partial \delta_\square} \right|_{wp} = \frac{\partial}{\partial \delta_\square} \left(\frac{1}{I_{xx}} (L - \mathcal{Q}\mathcal{R}(I_{zz} - I_{yy})) \right) \quad (\text{B.2.91})$$

$$= \frac{\bar{q}_{wp} S b}{I_{xx}} \frac{\partial}{\partial \delta_\square} C_L \quad (\text{B.2.92})$$

$$= \frac{\bar{q}_{wp} S b}{I_{xx}} C_{L_\square} \quad (\text{B.2.93})$$

$$\left. \frac{\partial \dot{Q}}{\partial \delta_\square} \right|_{wp} = \frac{\partial}{\partial \delta_\square} \left(\frac{1}{I_{yy}} (M - \mathcal{P}\mathcal{R}(I_{xx} - I_{zz})) \right) \quad (\text{B.2.94})$$

$$= \frac{\bar{q}_{wp} S \bar{c}}{I_{yy}} \frac{\partial}{\partial \delta_\square} C_M \quad (\text{B.2.95})$$

$$= \frac{\bar{q}_{wp} S \bar{c}}{I_{yy}} C_{M_\square} \quad (\text{B.2.96})$$

$$\left. \frac{\partial \dot{R}}{\partial \delta_\square} \right|_{wp} = \frac{\partial}{\partial \delta_\square} \left(\frac{1}{I_{zz}} (N - \mathcal{P}\mathcal{Q}(I_{yy} - I_{xx})) \right) \quad (\text{B.2.97})$$

$$= \frac{\bar{q}_{wp} S \bar{c}}{I_{zz}} \frac{\partial}{\partial \delta_\square} C_N \quad (\text{B.2.98})$$

$$= \frac{\bar{q}_{wp} S \bar{c}}{I_{zz}} C_{N_\square} \quad (\text{B.2.99})$$

$$\left. \frac{1}{|\mathbf{V}|_{wp}} \frac{\partial \dot{W}}{\partial \delta_\square} \right|_{wp} = \frac{1}{|\mathbf{V}|_{wp}} \frac{\partial}{\partial \delta_\square} \left(\frac{Z}{m} + \mathcal{U}\mathcal{Q} - \mathcal{V}\mathcal{P} \right) \quad (\text{B.2.100})$$

$$= \frac{1}{m|\mathbf{V}|_{wp}} \frac{\partial}{\partial \delta_\square} (\bar{q}_{wp} S) C_Z \quad (\text{B.2.101})$$

$$= \frac{\bar{q}_{wp} S}{m|\mathbf{V}|_{wp}} \frac{\partial}{\partial \delta_\square} (-C_d \alpha - C_l) \quad (\text{B.2.102})$$

$$= \frac{\bar{q}_{wp} S}{m|\mathbf{V}|_{wp}} \left(-\frac{2\alpha_{wp} C_{l_\square} (C_l)_{wp}}{\pi A e} - C_{l_\square} \right) \quad (\text{B.2.103})$$

$$\text{but } \frac{2\alpha_{wp} C_{l_\square} (C_l)_{wp}}{\pi A e} \ll C_{l_\square} \text{ therefore} \quad (\text{B.2.104})$$

$$= -\frac{\bar{q}_{wp} S}{m|\mathbf{V}|_{wp}} C_{l_\square} \quad (\text{B.2.105})$$

$$\left. \frac{1}{|\mathbf{V}|_{wp}} \frac{\partial \dot{V}}{\partial \delta_{\square}} \right|_{wp} = \frac{1}{|\mathbf{V}|_{wp}} \frac{\partial}{\partial \delta_{\square}} \left(\frac{Y}{m} - \mathcal{UR} + \mathcal{WP} \right) \quad (\text{B.2.106})$$

$$= \frac{1}{m|\mathbf{V}|_{wp}} \frac{\partial}{\partial \delta_{\square}} (\bar{q}_{wp} S) C_Y \quad (\text{B.2.107})$$

$$= \frac{\bar{q}_{wp} S}{m|\mathbf{V}|_{wp}} C_{Y_{\square}} \quad (\text{B.2.108})$$

B.3 Linearised State Matrices

With reference to section B the linearised state and input matrices becomes

$$\begin{bmatrix} \dot{p} \\ \dot{q} \\ \dot{r} \\ \dot{\alpha} \\ \dot{\beta} \end{bmatrix} = \begin{bmatrix} \frac{\bar{q}_{wp}Sb^2}{2I_{xx}|V|_{wp}}C_{LP} & \frac{\bar{q}_{wp}Sb^2}{2I_{xx}|V|_{wp}}C_{LR} + \frac{Q_{wp}(I_{yy}-I_{zz})}{I_{xx}} & 0 & \frac{\bar{q}_{wp}Sb}{I_{xx}}C_{L\beta} & 0 \\ \frac{\bar{q}_{wp}Sb^2}{2I_{yy}|V|_{wp}}C_{NQ} & \frac{\bar{q}_{wp}Sb^2}{2I_{zz}|V|_{wp}}C_{NR} & \frac{\bar{q}_{wp}S}{I_{yy}}C_{M\alpha} & 0 & \frac{\bar{q}_{wp}Sb}{I_{zz}}C_{N\beta} \\ \frac{\bar{q}_{wp}Sb^2}{2I_{zz}|V|_{wp}}C_{NP} + \frac{Q_{wp}(I_{xx}-I_{yy})}{I_{zz}} & 0 & 0 & -\frac{P_{wp}}{m|V|_{wp}}C_{l\alpha} & -P_{wp} \\ 0 & 1 - \frac{\bar{q}_{wp}S}{2m|V|_{wp}^2}C_{lQ} & 0 & \frac{\bar{q}_{wp}S}{m|V|_{wp}}C_{Y\beta} & \frac{\bar{q}_{wp}S}{m|V|_{wp}}C_{Y\beta} \\ \frac{\bar{q}_{wp}Sb}{2m|V|_{wp}^2}C_{YP} & 0 & 0 & 0 & 0 \end{bmatrix} + \begin{bmatrix} p \\ q \\ r \\ \alpha \\ \beta \end{bmatrix} \quad (B.3.1)$$

$$\begin{bmatrix} \frac{\bar{q}_{wp}Sb}{I_{xx}}C_{L\delta Ar} & \frac{\bar{q}_{wp}Sb}{I_{xx}}C_{L\delta Al} & \frac{\bar{q}_{wp}Sb}{I_{xx}}C_{L\delta Er} & \frac{\bar{q}_{wp}Sb}{I_{xx}}C_{L\delta El} & \frac{\bar{q}_{wp}Sb}{I_{xx}}C_{L\delta Fr} & \frac{\bar{q}_{wp}Sb}{I_{xx}}C_{L\delta Fl} & \frac{\bar{q}_{wp}Sb}{I_{xx}}C_{L\delta Rr} \\ \frac{\bar{q}_{wp}Sb}{I_{yy}}C_{M\delta Ar} & \frac{\bar{q}_{wp}Sb}{I_{yy}}C_{M\delta Al} & \frac{\bar{q}_{wp}Sb}{I_{yy}}C_{M\delta Er} & \frac{\bar{q}_{wp}Sb}{I_{yy}}C_{M\delta El} & \frac{\bar{q}_{wp}Sb}{I_{yy}}C_{M\delta Fr} & \frac{\bar{q}_{wp}Sb}{I_{yy}}C_{M\delta Fl} & \frac{\bar{q}_{wp}Sb}{I_{yy}}C_{M\delta Rr} \\ \frac{\bar{q}_{wp}Sb}{I_{zz}}C_{N\delta Ar} & \frac{\bar{q}_{wp}Sb}{I_{zz}}C_{N\delta Al} & \frac{\bar{q}_{wp}Sb}{I_{zz}}C_{N\delta Er} & \frac{\bar{q}_{wp}Sb}{I_{zz}}C_{N\delta El} & \frac{\bar{q}_{wp}Sb}{I_{zz}}C_{N\delta Fr} & \frac{\bar{q}_{wp}Sb}{I_{zz}}C_{N\delta Fl} & \frac{\bar{q}_{wp}Sb}{I_{zz}}C_{N\delta Rr} \\ -\frac{m|V|_{wp}}{\bar{q}_{wp}S}C_{l\delta Ar} & -\frac{m|V|_{wp}}{\bar{q}_{wp}S}C_{l\delta Al} & -\frac{m|V|_{wp}}{\bar{q}_{wp}S}C_{l\delta Er} & -\frac{m|V|_{wp}}{\bar{q}_{wp}S}C_{l\delta El} & -\frac{m|V|_{wp}}{\bar{q}_{wp}S}C_{l\delta Fr} & -\frac{m|V|_{wp}}{\bar{q}_{wp}S}C_{l\delta Fl} & -\frac{m|V|_{wp}}{\bar{q}_{wp}S}C_{l\delta Rr} \\ \frac{\bar{q}_{wp}S}{m|V|_{wp}}C_{Y\delta Ar} & \frac{\bar{q}_{wp}S}{m|V|_{wp}}C_{Y\delta Al} & \frac{\bar{q}_{wp}S}{m|V|_{wp}}C_{Y\delta Er} & \frac{\bar{q}_{wp}S}{m|V|_{wp}}C_{Y\delta El} & \frac{\bar{q}_{wp}S}{m|V|_{wp}}C_{Y\delta Fr} & \frac{\bar{q}_{wp}S}{m|V|_{wp}}C_{Y\delta Fl} & \frac{\bar{q}_{wp}S}{m|V|_{wp}}C_{Y\delta Rr} \end{bmatrix}$$

Appendix C

Process and Measurement Covariance Matrices

Uncertainty is found in all practical systems. The precise value of the states, measurements and even the active fault scenario is uncertain and random. Fortunately these uncertainties can be approximated closely with a compact parametric model. In the case of this research, a normal (Gaussian) distribution was chosen as the parametric model, as discussed in chapter 3.

The state of the system is a multi-dimensional vector and normal distributions of vectors are called multivariate. Multivariate normal distributions are characterised by density functions of the following Gaussian form [41]:

$$p(\mathbf{x}) = \frac{1}{(2\pi)^{\frac{m}{2}} |\boldsymbol{\Sigma}|^{0.5}} \exp\left(-\frac{1}{2}(\mathbf{x} - \boldsymbol{\mu})^T \boldsymbol{\Sigma}^{-1}(\mathbf{x} - \boldsymbol{\mu})\right) \quad (\text{C.0.1})$$

where m is the vector dimension. The distribution is parameterised by the mean vector and the covariance matrix, also called the moments parameterisation. The mean vector describes the expected values of x

$$\boldsymbol{\mu} = \begin{bmatrix} E[x_1] \\ E[x_2] \\ \vdots \\ E[x_m] \end{bmatrix} \quad (\text{C.0.2})$$

where n is the dimension of x .

The covariance of two random variables is defined as

$$\text{Cov}(x_i, x_j) = E[(x_i - E[x_i])(x_j - E[x_j])] \quad (\text{C.0.3})$$

where the covariance describes how these two random variables change together. The variance of a random variable is defined as

$$\text{Var}(x_i) = E[(x_i - E[x_i])^2] \quad (\text{C.0.4})$$

which is an indication of the statistical spread of the variable.

The covariance matrix contains all the possible covariances of the elements in the corresponding vector, including the elements' variance, where the diagonal terms of the covariance matrix are the variance of the elements. The covariance matrix is a positive semi-definite and symmetrical matrix with the form

$$\mathbf{\Sigma} = E[\mathbf{xx}^T] \quad (\text{C.0.5})$$

$$= \begin{bmatrix} \text{Var}(x_1) & \text{Cov}(x_1, x_2) & \dots & \text{Cov}(x_1, x_m) \\ \text{Cov}(x_2, x_1) & \text{Var}(x_2) & \dots & \text{Cov}(x_2, x_m) \\ \vdots & \vdots & \ddots & \vdots \\ \text{Cov}(x_n, x_1) & \text{Cov}(x_n, x_2) & \dots & \text{Var}(x_m) \end{bmatrix} \quad (\text{C.0.6})$$

For the linear and extended Kalman filter the initial state covariance matrix as well as the process and measurement covariance matrices are required. Usually it can be assumed the initial state, in which the state covariance matrix is assumed zero, is known exactly. The remaining problem is to find the covariances for the process and measurement noise.

C.1 Process Noise

The process noise covariance matrix describes the covariances of \mathbf{w}_k in equation 3.2.4. Process noise can be described in practical terms as the difference in dynamics between the mathematical model and the real aircraft, as well as external disturbances such as wind and structural phenomena. It is therefore not a straightforward process of determining the covariances, since no information is available to determine this statistical difference precisely.

A wind model was used with the mathematical model of equation 3.2.4 to empirically determine the process noise covariance. The process noise covariance matrix is very sensitive to the amount of disturbance: where a higher amount of disturbance induces a larger valued matrix.

$$\mathbf{R}_w \approx \mathbf{V}_{wind}^2 \begin{bmatrix} 69.5 & -51.2 & 0 & 0 & 0 \\ -51.2 & 76.5 & 0 & 0 & 0 \\ 0 & 0 & 94.75 & -36.9 & -67.1 \\ 0 & 0 & -36.9 & 38.1 & 11.2 \\ 0 & 0 & -67.1 & 11.2 & 85.2 \end{bmatrix} \times 10^{-9} \quad (\text{C.1.1})$$

where \mathbf{V}_{wind}^2 represents the expected wind velocity. For the development of this research, a value of 2 m/s was used, in accordance with previous flight test data.

The process noise covariance matrices for the fault scenarios are somewhat different from the no-fault case in that the estimated actuator deflection also has an effect on the covariances of the states. By using $\mathbf{V}_{wind}^2 = 2$ m/s, the noise covariance matrices for the fault scenarios

were determined to be

$$(R_w)_{Ar} = \begin{bmatrix} 0.29 & -0.223 & 0 & 0.06 & -0 & -0.056 \\ -0.223 & 0.523 & 0 & 0.194 & -0 & -0.18 \\ 0 & 0 & 0.392 & -0.187 & 0.284 & -0 \\ 0.060 & 0.194 & -0.187 & 4.912 & -0.0292 & -4.319 \\ 0 & -0.008 & 0.284 & -0.292 & 0.0591 & 0.169 \\ -0.056 & -0.180 & -0 & -4.319 & 0.0169 & 4 \end{bmatrix} \times 10^{-6} \quad (\text{C.1.2})$$

$$(R_w)_{Al} = \begin{bmatrix} 0.290 & -0.223 & 0 & -0.06 & 0 & 0.056 \\ -0.223 & 0.523 & 0 & -0.194 & 0 & 0.18 \\ 0 & -0 & 0.392 & -0.187 & 0.284 & 0 \\ -0.06 & -0.194 & -0.187 & 4.912 & -0.292 & -4.319 \\ 0 & 0 & 0.284 & -0.292 & 0.591 & 0.169 \\ 0.056 & 0.18 & 0 & -4.319 & 0.169 & 4 \end{bmatrix} \times 10^{-6} \quad (\text{C.1.3})$$

$$(R_w)_{Er} = \begin{bmatrix} 0.289 & -0.217 & 0 & 0 & 0 & -0.021 \\ -0.217 & 1.3 & 0 & 0.084 & 0.122 & -1.773 \\ 0 & 0 & 0.392 & -0.189 & 0.284 & 0 \\ 0 & 0.084 & -0.189 & 0.258 & -0.096 & -0.191 \\ 0 & 0.122 & 0.284 & -0.096 & 0.603 & -0.275 \\ -0.021 & -1.773 & 0 & -0.191 & -0.275 & 4 \end{bmatrix} \times 10^{-6} \quad (\text{C.1.4})$$

$$(R_w)_{El} = \begin{bmatrix} 0.289 & -0.217 & 0 & 0 & 0 & -0.021 \\ -0.217 & 1.301 & 0 & -0.084 & -0.122 & -1.773 \\ 0 & 0 & 0.392 & -0.189 & 0.284 & 0 \\ 0 & -0.084 & -0.189 & 0.258 & -0.096 & 0.191 \\ 0 & -0.122 & 0.284 & -0.096 & 0.603 & 0.275 \\ -0.021 & -1.773 & 0 & 0.191 & 0.275 & 4 \end{bmatrix} \times 10^{-6} \quad (\text{C.1.5})$$

$$(R_w)_{Rr} = \begin{bmatrix} 0.289 & -0.226 & 0 & 0 & 0 & 0 \\ -0.226 & 0.551 & 0 & 0 & 0.1 & -0.380 \\ 0 & 0 & 0.392 & -0.188 & 0.281 & 0.013 \\ 0 & 0 & -0.188 & 0.250 & -0.129 & 0.077 \\ 0 & 0.100 & 0.281 & -0.129 & 0.863 & -1.056 \\ 0 & -0.380 & 0.013 & 0.077 & -1.056 & 4 \end{bmatrix} \times 10^{-6} \quad (\text{C.1.6})$$

$$(R_w)_{Rl} = \begin{bmatrix} 0.289 & -0.226 & 0 & 0 & 0 & 0 \\ -0.226 & 0.551 & 0 & 0 & -0.100 & 0.380 \\ 0 & 0 & 0.392 & -0.188 & 0.281 & 0.013 \\ 0 & 0 & -0.188 & 0.250 & -0.129 & 0.0077 \\ 0 & -0.100 & 0.281 & -0.129 & 0.863 & -1.056 \\ 0 & 0.380 & 0.013 & 0.077 & -1.056 & 4 \end{bmatrix} \times 10^{-6} \quad (\text{C.1.7})$$

C.2 Measurement Noise

The measurement noise covariance matrix describes the covariances of \mathbf{v}_k in equation 3.2.5. The measurement noise is determined by sensor data sheets. It is assumed that sensor readings are independent of one another and therefore the covariances between the measurements will be zero. The resulting covariance matrix is a diagonal matrix with the variances of the measurement noise as its elements.

The data sheets show that the angle of attack and angle of sideslip have a noise variance of 20×10^{-6} in radians squared. The angular rate sensors have a noise variance of 109.66×10^{-6} in radians squared, which results in a measurement noise covariance matrix of

$$\mathbf{R}_v = \begin{bmatrix} 20 & 0 & 0 & 0 & 0 \\ 0 & 109.66 & 0 & 0 & 0 \\ 0 & 0 & 20 & 0 & 0 \\ 0 & 0 & 0 & 109.66 & 0 \\ 0 & 0 & 0 & 0 & 109.66 \end{bmatrix} \times 10^{-6} \quad (\text{C.2.1})$$

The fault scenario Kalman filters use the same measurement noise covariance matrix, as they use the same sensor data as the no-fault Kalman filter

$$(\mathbf{R}_v)_f = (\mathbf{R}_v)_{nf} \quad (\text{C.2.2})$$

Appendix D

Healthy and Faulty Residuals Covariance Matrices

D.1 Healthy Residuals Covariance Matrices

The healthy covariance matrix without passing through a low pass filter.

$$\Sigma_H = \begin{bmatrix} 0.3516 & -0.0082 & 0.6645 & 0.4644 & 0.1399 & -0.0486 \\ -0.0082 & 0.3516 & -0.4644 & -0.6645 & -0.0486 & 0.1399 \\ 0.6645 & -0.4644 & 1.9350 & 1.8184 & 0.3222 & -0.2693 \\ 0.4644 & -0.6645 & 1.8184 & 1.9350 & 0.2693 & -0.3222 \\ 0.1399 & -0.0486 & 0.3222 & 0.2693 & 3.2939 & 3.1951 \\ -0.0486 & 0.1399 & -0.2693 & -0.3222 & 3.1951 & 3.2939 \end{bmatrix} \quad (\text{D.1.1})$$

The healthy covariance matrix after passing through a low pass filter.

$$\Sigma_H = \begin{bmatrix} 10.3249 & -0.2626 & 6.8788 & 4.1782 & 1.2825 & -1.4424 \\ -0.2626 & 10.3249 & -4.4623 & -7.3864 & -1.2227 & 1.7051 \\ 6.8788 & -4.4623 & 25.6371 & 22.7840 & 2.6558 & -3.2867 \\ 4.1782 & -7.3864 & 22.7840 & 25.6371 & 2.6179 & -3.4418 \\ 1.2825 & -1.2227 & 2.6558 & 2.6179 & 102.6914 & 97.0422 \\ -1.4424 & 1.7051 & -3.2867 & -3.4418 & 97.0422 & 102.6914 \end{bmatrix} \times 10^{-3} \quad (\text{D.1.2})$$

D.2 Faulty Residuals Covariance Matrices Without the Effect of Disturbances

$$\Sigma_{F,Ar} = \begin{bmatrix} 0.5000 & 0.4422 & 0.3280 & -0.2153 & 0.1354 & 0.1058 \\ 0.4422 & 0.3922 & 0.2909 & -0.1909 & 0.1200 & 0.0938 \\ 0.3280 & 0.2909 & 0.2158 & -0.1416 & 0.0891 & 0.0696 \\ -0.2153 & -0.1909 & -0.1416 & 0.0930 & -0.0584 & -0.0457 \\ 0.1354 & 0.1200 & 0.0891 & -0.0584 & 0.0368 & 0.0288 \\ 0.1058 & 0.0938 & 0.0696 & -0.0457 & 0.0288 & 0.0225 \end{bmatrix}_{\mathbf{N}(\tau,n)=0} \quad (\text{D.2.1})$$

$$\Sigma_{F,AI} = \begin{bmatrix} 0.3922 & 0.4422 & 0.1909 & -0.2909 & 0.0938 & 0.1200 \\ 0.4422 & 0.5000 & 0.2153 & -0.3280 & 0.1058 & 0.1354 \\ 0.1909 & 0.2153 & 0.0930 & -0.1416 & 0.0457 & 0.0584 \\ -0.2909 & -0.3280 & -0.1416 & 0.2158 & -0.0696 & -0.0891 \\ 0.0938 & 0.1058 & 0.0457 & -0.0696 & 0.0225 & 0.0288 \\ 0.1200 & 0.1354 & 0.0584 & -0.0891 & 0.0288 & 0.0368 \end{bmatrix}_{\mathbf{N}(\tau,n)=0} \quad (\text{D.2.2})$$

$$\Sigma_{F,Er} = \begin{bmatrix} 0.1390 & -0.1044 & 0.2635 & 0.2436 & 0.1339 & 0.0064 \\ -0.1044 & 0.0784 & -0.1980 & -0.1830 & -0.1006 & -0.0048 \\ 0.2635 & -0.1980 & 0.5000 & 0.4621 & 0.2539 & 0.0121 \\ 0.2436 & -0.1830 & 0.4621 & 0.4271 & 0.2347 & 0.0112 \\ 0.1339 & -0.1006 & 0.2539 & 0.2347 & 0.1290 & 0.0061 \\ 0.0064 & -0.0048 & 0.0121 & 0.0112 & 0.0061 & 0.0003 \end{bmatrix}_{\mathbf{N}(\tau,n)=0} \quad (\text{D.2.3})$$

$$\Sigma_{F,El} = \begin{bmatrix} 0.0784 & -0.1044 & 0.1830 & 0.1980 & -0.0048 & -0.1006 \\ -0.1044 & 0.1390 & -0.2436 & -0.2635 & 0.0064 & 0.1339 \\ 0.1830 & -0.2436 & 0.4271 & 0.4621 & -0.0112 & -0.2347 \\ 0.1980 & -0.2635 & 0.4621 & 0.5000 & -0.0121 & -0.2539 \\ -0.0048 & 0.0064 & -0.0112 & -0.0121 & 0.0003 & 0.0061 \\ -0.1006 & 0.1339 & -0.2347 & -0.2539 & 0.0061 & 0.1290 \end{bmatrix}_{\mathbf{N}(\tau,n)=0} \quad (\text{D.2.4})$$

$$\Sigma_{F,Rr} = \begin{bmatrix} 0.0148 & -0.0022 & 0.0213 & 0.0141 & 0.0860 & 0.0771 \\ -0.0022 & 0.0003 & -0.0032 & -0.0021 & -0.0130 & -0.0116 \\ 0.0213 & -0.0032 & 0.0308 & 0.0204 & 0.1242 & 0.1113 \\ 0.0141 & -0.0021 & 0.0204 & 0.0134 & 0.0821 & 0.0736 \\ 0.0860 & -0.0130 & 0.1242 & 0.0821 & 0.5000 & 0.4491 \\ 0.0771 & -0.0116 & 0.1113 & 0.0736 & 0.4491 & 0.4026 \end{bmatrix}_{\mathbf{N}(\tau,n)=0} \quad (\text{D.2.5})$$

$$\Sigma_{F,Rl} = \begin{bmatrix} 0.0003 & -0.0022 & 0.0021 & 0.0032 & -0.0116 & -0.0130 \\ -0.0022 & 0.0148 & -0.0141 & -0.0213 & 0.0771 & 0.0860 \\ 0.0021 & -0.0141 & 0.0134 & 0.0204 & -0.0736 & -0.0821 \\ 0.0032 & -0.0213 & 0.0204 & 0.0308 & -0.1113 & -0.1242 \\ -0.0116 & 0.0771 & -0.0736 & -0.1113 & 0.4026 & 0.4491 \\ -0.0130 & 0.0860 & -0.0821 & -0.1242 & 0.4491 & 0.5000 \end{bmatrix}_{\mathbf{N}(\tau,n)=0} \quad (\text{D.2.6})$$

D.3 Final Faulty Residuals Covariance Matrices

$$\Sigma_{F,Ar} = \begin{bmatrix} 0.5103 & 0.4419 & 0.3349 & -0.2111 & 0.1367 & 0.1044 \\ 0.4419 & 0.4025 & 0.2864 & -0.1983 & 0.1188 & 0.0955 \\ 0.3349 & 0.2864 & 0.2414 & -0.1188 & 0.0917 & 0.0663 \\ -0.2111 & -0.1983 & -0.1188 & 0.1186 & -0.0558 & -0.0491 \\ 0.1367 & 0.1188 & 0.0917 & -0.0558 & 0.1395 & 0.1258 \\ 0.1044 & 0.0955 & 0.0663 & -0.0491 & 0.1258 & 0.1252 \end{bmatrix} \quad (\text{D.3.1})$$

$$\Sigma_{F,AI} = \begin{bmatrix} 0.4025 & 0.4419 & 0.1978 & -0.2867 & 0.0951 & 0.1186 \\ 0.4419 & 0.5103 & 0.2108 & -0.3354 & 0.1046 & 0.1371 \\ 0.1978 & 0.2108 & 0.1186 & -0.1188 & 0.0483 & 0.0551 \\ -0.2867 & -0.3354 & -0.1188 & 0.2414 & -0.0670 & -0.0925 \\ 0.0951 & 0.1046 & 0.0483 & -0.0670 & 0.1252 & 0.1258 \\ 0.1186 & 0.1371 & 0.0551 & -0.0925 & 0.1258 & 0.1395 \end{bmatrix} \quad (\text{D.3.2})$$

$$\Sigma_{F,Er} = \begin{bmatrix} 0.1493 & -0.1047 & 0.2704 & 0.2478 & 0.1352 & 0.0049 \\ -0.1047 & 0.0888 & -0.2025 & -0.1904 & -0.1018 & -0.0031 \\ 0.2704 & -0.2025 & 0.5255 & 0.4848 & 0.2566 & 0.0088 \\ 0.2478 & -0.1904 & 0.4848 & 0.4527 & 0.2373 & 0.0077 \\ 0.1352 & -0.1018 & 0.2566 & 0.2373 & 0.2317 & 0.1032 \\ 0.0049 & -0.0031 & 0.0088 & 0.0077 & 0.1032 & 0.1030 \end{bmatrix} \quad (\text{D.3.3})$$

$$\Sigma_{F,El} = \begin{bmatrix} 0.0888 & -0.1047 & 0.1899 & 0.2022 & -0.0035 & -0.1020 \\ -0.1047 & 0.1493 & -0.2480 & -0.2709 & 0.0051 & 0.1356 \\ 0.1899 & -0.2480 & 0.4527 & 0.4848 & -0.0085 & -0.2380 \\ 0.2022 & -0.2709 & 0.4848 & 0.5255 & -0.0095 & -0.2574 \\ -0.0035 & 0.0051 & -0.0085 & -0.0095 & 0.1030 & 0.1032 \\ -0.1020 & 0.1356 & -0.2380 & -0.2574 & 0.1032 & 0.2317 \end{bmatrix} \quad (\text{D.3.4})$$

$$\Sigma_{F,Rr} = \begin{bmatrix} 0.0251 & -0.0025 & 0.0282 & 0.0183 & 0.0873 & 0.0757 \\ -0.0025 & 0.0107 & -0.0077 & -0.0095 & -0.0142 & -0.0099 \\ 0.0282 & -0.0077 & 0.0564 & 0.0431 & 0.1269 & 0.1081 \\ 0.0183 & -0.0095 & 0.0431 & 0.0391 & 0.0847 & 0.0701 \\ 0.0873 & -0.0142 & 0.1269 & 0.0847 & 0.6037 & 0.5461 \\ 0.0757 & -0.0099 & 0.1081 & 0.0701 & 0.5461 & 0.5053 \end{bmatrix} \quad (\text{D.3.5})$$

$$\Sigma_{F,RI} = \begin{bmatrix} 0.0107 & -0.0025 & 0.0090 & 0.0074 & -0.0104 & -0.0144 \\ -0.0025 & 0.0251 & -0.0186 & -0.0287 & 0.0759 & 0.0877 \\ 0.0090 & -0.0186 & 0.0391 & 0.0431 & -0.0709 & -0.0853 \\ 0.0074 & -0.0287 & 0.0431 & 0.0564 & -0.1087 & -0.1276 \\ -0.0104 & 0.0759 & -0.0709 & -0.1087 & 0.5053 & 0.5461 \\ -0.0144 & 0.0877 & -0.0853 & -0.1276 & 0.5461 & 0.6037 \end{bmatrix} \quad (\text{D.3.6})$$

Appendix E

Flight Test Plan

Name of test	Meraka Modular UAV FDI flight test 1
Date of test	19 September 2012
Location of test	Helderberg Radio Flyers Club 34° 02' 47.69" S 18° 44' 26.55" E

Table E.1: Flight test details.

Table E.2 is an example of the form that must be signed by all parties involved in the flight test to state that they understand the proposed flight test as well as the safety procedures of the Helderberg Radio Flyers Club.

Team Member	Name	Signature	Date
Flight Test Coordinator	Hendrik Odendaal		
Flight Test Coordinator Assistant	Lionel Basson		
Safety Pilot	Michael Basson		
Safety Officer	Japie Engelbrecht		

Table E.2: Safety and execution sign-in form.

E.1 Introduction

E.1.1 Background

This Meraka Modular UAV flight test will serve as an analysis of the performance of the FDI processes that were developed in this research. The UAV was already tested on the 2nd August 2012, where it displayed its flight readiness for this test.

E.1.2 Test Objectives

- To fail the actuators one by one in a controlled manner, at 0° locked-in-place.
- To fail the actuators one by one in a controlled manner, at 2.5° locked-in-place.
- To evaluate the performance of the aircraft with an actuator fault.
- To gather flight data while the aircraft is flying with faults.

E.1.3 Description of the Test Item

The Meraka Modular UAV will be used as the test aircraft. More specific technical information can be found in appendix A as well as in chapter 2. The aircraft is shown in figure 5.1.

E.1.4 Test Scope

Michael Basson will take off manually and fly the aircraft until the trim of the aircraft is set and he is comfortable with the aircraft performance. Michael will control the aircraft via radio controller throughout the flight test, even when a fault is active.

The fault sequence will be pre-programmed so that the type of fault can be chosen in-flight at the ground station. When ready, Michael can activate and de-activate the faults on the remote control. Each fault will be activated for at least 20 seconds before again de-activating it, except in cases where the fault is causing uncontrollable behaviour. All six actuators of interest will be tested. These actuators are:

- Right aileron
- Left aileron
- Right elevator
- Left elevator
- Right rudder
- Left rudder

When the test is finished Michael will de-activate any active faults and land the aircraft.

The test will first be executed by inducing only 0° locked-in-place faults, as these faults should cause no uncontrollable behaviour. This is done to first identify whether the aircraft will be able to sustain flight after such faults.

If the controllability of the aircraft is acceptable in the presence of faults, the same test will be conducted, except that 2.5° locked-in-place faults will then be activated.

E.2 Test Preparation

E.2.1 Project Team

The project team will be notified of their tasks and handed a copy of this flight test plan before the test.

- Hendrik Odendaal
- Lionel Basson
- Michael Basson
- Japie Engelbrecht

E.2.2 Logistical Support

For the transportation of the aircraft a vehicle will be hired from the Stellenbosch University vehicle pool. The reservation number was: 2048622.

E.2.3 Briefings and Debriefings

Flight briefing will be done before the flight test and briefing will be done after the flight test, both taking place at the airfield.

E.2.4 Safety

- The relevant test hazard analysis will be conducted before flight.
- First aid kit must be available.
- Fire services (extinguishers) must be available.
- Participants will be briefed on general safety regarding the UAV on the flight day.
- Refer and adhere to the checklist.

E.3 Details of the Test

E.3.1 Test Conditions

Weather conditions will be monitored and the tests will only take place if the weather falls within the requirements for these tests: there should be no rain and the wind must be below 10 m/s.

E.3.2 Data Required

The states of the system, as well as the actuator commands, are essential data that must be logged.

E.3.3 Data Analysis

The data will be used to determine the performance of the FDI systems developed in this research.

E.3.4 Acceptance Criteria

- All actuators fail one by one at 0° locked-in-place without trouble.
- All actuators fail one by one at 2.5° locked-in-place without trouble.
- All required data is logged correctly.

E.4 Test Schedule

Test description	Expected duration
Trim and check aircraft performance	1 minute
Fail right aileron at 0° locked-in-place	20 seconds
Fail left aileron at 0° locked-in-place	20 seconds
Fail right elevator at 0° (from trim) locked-in-place	20 seconds
Fail left elevator at 0° (from trim) locked-in-place	20 seconds
Fail right rudder at 0° locked-in-place	20 seconds
Fail left rudder at 0° locked-in-place	20 seconds
Fail right aileron at positive 2.5° locked-in-place	20 seconds
Fail left aileron at positive 2.5° locked-in-place	20 seconds
Fail right elevator at positive 2.5° (from trim) locked-in-place	20 seconds
Fail left elevator at positive 2.5° (from trim) locked-in-place	20 seconds
Fail right rudder at positive 2.5° locked-in-place	20 seconds
Fail left rudder at positive 2.5° locked-in-place	20 seconds

Note: The battery power will be monitored constantly. If the power becomes too low the aircraft will be landed and the batteries will be replaced.

Table E.3: The test schedule.

E.5 Equipment Checklist

Vehicle-related		CHECK
Two sets of charged batteries		
Two chargers and a power supply		
SD Card for data logging		
Ground station		CHECK
Ground station laptop		
External matte LCD display		
Ground station RF module		
Fold up table		
AC extension lead (5m) + multi-plug		
Radio controller		CHECK
RC transmitter		
Backup battery for RC transmitter		
Flight log + Bind plug		
Camera equipment		CHECK
Off-board video camera		
Tripod		
Still camera		
Miscellaneous		CHECK
Flight toolbox		
Fire extinguisher		
First aid kit		
Two-way radios		
Notes		

Table E.4: Equipment checklist.

Bibliography

- [1] Diebel, J.: Representing Attitude: Euler Angles, Unit Quaternions, and Rotation Vectors. Tech. Rep., Stanford University, October 2006.
- [2] Ducard, G.J.: *Fault-tolerant Flight Control and Guidance Systems*. Springer, 2009.
- [3] Basson, L.: *Control Allocation as Part of a Fault-tolerant Control Architecture for UAVs*. Master's thesis, Stellenbosch University, December 2010.
- [4] Isermann, R.: *Fault-Diagnosis Systems: An Introduction from Fault Detection to Fault Tolerance*. Springer-Verlag, 2006.
- [5] Maki, M., Jiang, J. and Hagino, K.: A stability guaranteed active fault-tolerant control system against actuator failures. *International Journal of Robust and Nonlinear Control*, vol. 14, 2004.
- [6] Wise, K.A., Brinker, J.S., Calise, A.J., Enns, D.F., Elgersma, M.R. and Voulgaris, P.: Direct Adaptive Reconfigurable Flight Control for a Tailless Advanced Fighter Aircraft. *International Journal of Robust and Nonlinear Control*, vol. 9, 1999.
- [7] Zhang, Y. and Jiang, J.: Bibliographical review on reconfigurable fault-tolerant control systems. *Annual Reviews in Control*, vol. 32, 2008.
- [8] Gertler, J.J.: *Fault Detection and Diagnosis in Engineering Systems*. 1st edn. Marcel Dekker Inc., 1998.
- [9] Niemann, H.: A Setup for Active Fault Diagnosis. *IEEE Transactions on Automatic Control*, vol. 51, no. 9, September 2006.
- [10] Poulsen, N.K. and Niemann, H.: Active Fault Diagnosis Based on Stochastic Tests. *International Journal of Applied Mathematics and Computer Science*, vol. 18, no. 4, 2008.
- [11] Cieslak, J., Henry, D. and Zolghadri, A.: Development of an Active Fault-Tolerant Flight Control Strategy. *Journal of Guidance, Control and Dynamics*, vol. 31, no. 1, January 2008.
- [12] Niemann, H.: Fault Tolerant Control Based on Active Fault Diagnosis. In: *American Control Conference*. Portland, June 2005.

- [13] Busch, R. and Peddle, I.: Active Fault Detection for an Open Loop Stable SISO System. *IEEE Transactions on Automatic Control*, 2011.
- [14] Hearn, G., Grimble, M.J. and Johnson, M.A.: Integrated Fault Monitoring and Reliable Control. *UKACC International Conference on Control '98*, vol. 455, September 1998.
- [15] Buffington, J.M.: Tailless Aircraft Control Allocation. Tech. Rep., Wright-Patterson Air Force Base, Ohio, May 1997.
- [16] Shtessel, Y., Buffington, J. and Banda, S.: Tailless Aircraft Flight Control Using Multiple Time Scale Reconfigurable Sliding Modes. *IEEE Transactions on Control Systems Technology*, vol. 10, no. 2, March 2002.
- [17] Tang, S., Zhang, S. and Zhang, Y.: A Modified Direct Allocation Algorithm with Application to Redundant Actuators. *Chinese Journal of Aeronautics*, vol. 24, 2011.
- [18] Blankel, M., Staroswiecki, M. and Wu, N.E.: Concepts and Methods in Fault tolerant Control. *American Control Conference*, June 2001.
- [19] Wang, D. and Lum, K.-Y.: Adaptive Unknown Input Observer Approach for Aircraft Actuator Fault Detection and Isolation. *International Journal of Adaptive Control and Signal Processing*, 2007.
- [20] Eide, P. and Maybeck, P.S.: An MMAE Failure Detection System for the F-16. Tech. Rep., Air Force Institute of Technology, 1996.
- [21] Åsröm, K.J. and Eykhoff, P.: System Identification: A Survey. *Automatica*, vol. 7, 1971.
- [22] Ward, D., Barron, R.L., Carley, M.P. and Curtis, T.J.: Real-time Parameter Identification for Self-designing Flight Control. *National Aerospace and Electronics Conference*, 1994.
- [23] Chow, E.Y. and Willsky, A.S.: Analytical Redundancy and the Design of Robust Failure Detection Systems. *IEEE Transactions on Automatic Control*, vol. 29, no. 7, 1984.
- [24] Härkegöard, O.: Efficient Active Set Algorithms for Solving Constrained Least Squares Problems in Aircraft Control Allocation. *Decision and Control*, vol. 2, pp. 1295–1300, 2002.
- [25] Maybeck, P.S.: Multiple Model Adaptive Algorithms for Detecting and Compensating Sensor and Actuator/Surface Failures in Aircraft Flight Control Systems. *International Journal of Robust and Nonlinear Control*, vol. 9, 1999.
- [26] Etkin, B. and Reid, L.D.: *Dynamics of Flight: Stability and Control*. 3rd edn. John Wiley & Sons, Inc., 1996.
- [27] Blakelock, J.H.: *Automatic Control of Aircraft and Missiles*. 2nd edn. John Wiley & Sons, Inc., 1991.

- [28] Cook, M.: *Flight Dynamics Principles*. Elsevier, 2007.
- [29] Peddle, I.: Advance Automation 833: Introductory Course to Aircraft Dynamics. April 2011.
- [30] Meriam, J. and Kraige, L.: *Engineering Mechanics: Dynamics*. 5th edn. John Wiley & Sons, Inc., 2003.
- [31] Peddle, I.: *Autonomous Flight of a Model Aircraft*. Master's thesis, Stellenbosch University, April 2005.
- [32] Franklin, G.F., Powell, J.D. and Emami-Naeini, A.: *Feedback Control of Dynamic Systems*. 5th edn. Prentice Hall, 2009.
- [33] Mehra, R.K.: On the Identification of Variances and Adaptive Kalman Filtering. *IEEE Transactions on Automatic Control*, vol. 15, no. 2, 1970.
- [34] Edwards, A.: *Likelihood*. Cambridge University Press, 1972.
- [35] Zarchan, P. and Musoff, H.: *Fundamentals of Kalman Filtering: A Practical Approach*. 2nd edn. Massachusetts Institute of Technology, 2006.
- [36] Deckert, J.C., Desai, M.N., Deyst, J.J. and Willsky, A.S.: F-8 DFBW Sensor Failure Identification Using Analytic Redundancy. *IEEE Transactions on Automatic Control*, vol. 22, no. 5, 1977.
- [37] Golub, G. and Reinsch, C.: *Singular Value Decomposition and Least Squares Solutions*. Springer, 1970.
- [38] Lasdon, L.S., Warren, A.D., Jain, A. and Ratner, M.: Design and Testing of a Generalized Reduced Gradient Code for Nonlinear Programming. *ACM Transactions on Mathematical Software*, vol. 4, no. 1, 1978.
- [39] Healy, J.D.: A Note on Multivariate CUSUM Procedures. *Technometrics*, vol. 29, no. 4, 1987.
- [40] Peebles, P.Z.: *Probability, Random Variables and Random Signal Principles*. 4th edn. McGraw Hill, 2001.
- [41] Thrun, S., Burgard, W. and Fox, D.: *Probabilistic Robotics*. Massachusetts Institute of Technology, 2006.